Spring 7-31-2017

Novel Design Strategies for Platinum-Containing Conjugated Polymers and Small Molecules for Organic Solar Cells

Wenhan He
University of New Mexico

Wenhan He

Candidate

Chemistry and Chemical Biology

Department

This dissertation is approved, and it is acceptable in quality and form for publication:

Approved by the Dissertation Committee:

Prof. Yang Qin, Chairperson

Prof. Fu-Sen Liang

Prof. Ramesh Giri

Prof. Michael Heagy

Novel Design Strategies for Platinum-Containing Conjugated Polymers and Small Molecules for Organic Solar Cells

By

Wenhan He

M.S., Industrial Catalysis, Shanghai Normal University, Shanghai, China, 2010

Bachelor, Applied Chemistry, Shanghai Normal University, Shanghai, China, 2007

DISSERTATION

Submitted in Partial Fulfillment of the
Requirements for the Degree of

Doctor of Philosophy
Chemistry

The University of New Mexico
Albuquerque, New Mexico

May, 2017

Acknowledgements

Firstly, and most importantly, I would like to express my sincere gratitude to my supervisor Prof. Yang Qin for his continuous guidance and support in the past 5 years. During my PhD program, Prof. Qin's patience, motivation and immense knowledge helped me to understand how to accomplish a project in a scientific way and I can't imagine attaining my PhD degree without him. I can say with certainty that he is the best advisor in my academic career so far.

Secondly, I would like to thank my committee members, Prof. Fu-Sen Liang, Prof. Ramesh Giri, and Prof. Michael Heagy for their insightful comments and encouragement, but also for their advice during my research proposal which indeed furthered my progress of the projects.

Thirdly, my thanks also go to all my collaborators, whose efforts facilitate my projects. Specifically, Prof. Jeff Rack and his student Maksim Livshits helped me with time-resolved transient absorption spectroscopy. Dr. Ying-Bing Jiang trained me as a TEM user and did all the troubleshooting during the measurements. Dr. Qin Wu ran the density functional theory (DFT) calculation for me. Dr. Diane A. Dickie helped me with single-crystal XRD analysis. Prof. Rohit Prasankumar provided me with low-temperature fluorescence lifetime measurements and Prof. Fu-Sen Liang generously allowed me to access his lab microscope conveniently during the past years. All these experiments and data helped me to better understand the relationship between the structure, morphology and photophysical properties of the compounds I was working on. Without their input, it would have been impossible for me to achieve some nice results in my experiments.

Fourthly, I also want to thank all my labmates for their time and efforts. Specifically, I want to express my thanks to my student, Luis Mejiaortega for his long term support in my research as well as spending time on revising my resume and cover letters for my job hunting.

Last but not least, I would like to thank my family: my parents and my wife for supporting me spiritually throughout my research and my life in general. In addition, I would like to thank my friendship family, Sam Brandt and his family for helping me to go through the early times in the United States.

Novel Design Strategies for Platinum-Containing Conjugated Polymers and Small Molecules for Organic Solar Cells

By

Wenhan He

M.S., Industrial Catalysis, Shanghai Normal University, China, 2010

Bachelor, Applied Chemistry, Shanghai Normal University, China, 2007

PhD, Chemistry, University of New Mexico, USA, 2017

Abstract

Current state-of-the-art organic solar cells (OSCs) adopt the strategy of using conjugated polymers or small molecules as donors and fullerene derivatives as acceptors in their active layers. Regarding to the donors of interest, the conjugated polymers and small molecules coupled with heavy metals have been less explored compared to their counterparts. Among various transition metal complexes applied, Pt(II) complexes are unique because of their intrinsic square planar geometries and ability to serve as building blocks for conjugated systems. Furthermore, the heavy metal Pt facilitates the formation of triplet excitons with longer life times through spin-orbital coupling which are of benefit for the OSCs application. However, in order to obtain low bandgap polymers, people are intended to use chromophores with long conjugated length, nevertheless such design will inevitably dilute the spin-orbital coupling effect and finally influence the formation of triplet excitons.

Furthermore, the majority of Pt-containing conjugated systems reported so far shared a common feature— they all possessed “dumbbell” shaped structures and were amorphous, leading to poor device performance. In addition, there were few examples reporting the capture of the triplet excitons by the fullerene acceptors in the OSCs since there is a mismatch between the triplet energy state (T_1) of the Pt-containing compounds and the LUMO level of fullerene acceptors. As a result, these three intrinsic problems will impede the further development of such a field.

In order to solve these problems, I originally designed and synthesized three novel compounds with unique proprieties named as Bodipy-Pt, Pt-SM and $C_{60}^{+}SDS^{-}$. Specifically, Bodipy has the advantages of compact size, easy to synthesis and high fluorescence quantum yield which can effectively solve the problem of long conjugated length. While in terms of second problem, the new Pt-SM possessed a “roller-wheel” structural design with increased crystallinity through slip-stack packing; the solar cell efficiency of this compound out-performed all existing Pt-containing materials in organic solar cells. I have further studied the photophysical behavior of the molecule through time-resolved transient absorption spectroscopy as well as DFT calculation. Finally, because of its ionic nature, the LUMO level of $C_{60}^{+}SDS^{-}$ is lower than that of PCBM which serves as a common fullerene acceptor applied in the organic solar cell. Above all, through the measurement of time-resolved transient absorption, I have confirmed the $C_{60}^{+}SDS^{-}$ can capture the triplet exciton of Pt-SM through dynamic quenching since the life-time of triplet exciton has decreased after adding $C_{60}^{+}SDS^{-}$ solution.

TABLE OF CONTENTS

LIST OF FIGURES

LIST OF SCHEMES

LIST OF TABLES

LIST OF ABBREVIATIONS

AIL	Anode Interfacial Layer
BDT	Benzenedithiophene
BTD	Benzothiadiazole
BHJ	Bulk Heterojunction
Bodipy	Boron-dipyrromethene
CIL	Cathode Interfacial Layer
CP	Conjugated Polymers
CV	Cyclic Voltammetry
D-A	Donor-Acceptor
DDQ	2,3-Dichloro-5,6-dicyano-1,4-benzoquinone
DFT	Density Functional Theory
DSC	Differential Scanning Calorimetry
EQE	External Quantum Efficiency
Et_3N/TEA	Triethylamine
FF	Fill Factor
FRET	Forster Resonance Energy Transfer
HOMO	Highest Occupied Molecular Orbital

HRMS	High Resolution Mass Spectrometry
ICT	Intramolecular Charge-transfer
IL	Intra-ligand
IR	Infrared
ISC	Intersystem Crossing
ITO	Indium Tin Oxide
I-V curves	Current Density-Voltage Curves
J_{max}	Maximum Current Density
J_{sc}	Short-circuit Current
LUMO	Lowest Unoccupied Molecular Orbital
MEH-PPV	Poly (2-methoxy-5-(2'-ethyl-hexyloxy)-1,4-phenylenevinylene)
MLCT	Metal-to-ligand-charge transfer
Mn	Number Average Molecular Weight
Mw	Weight Average Molecular Weight
NMR	Nuclear Magnetic Resonance
NTO	Natural Transition Orbital
OPVs	Organic Photovoltaic
OSCs	Organic Solar Cells

PCE	Power Conversion Efficiency
$PC_{61}BM$	Phenyl-C_{61}-butyric Acid Methyl Ester
$PC_{71}BM$	Phenyl-C_{71}-butyric Acid Methyl Ester
PCM	Polarizable Continuum Model
PDI	Polydispersity Index
PEDOT: PSS	Poly(3,4-ethylenedioxythiophene) polystyrene sulfonate
P3HT	Poly (3-hexylthiophene)
P_{in}	Power Input
QY	Quantum Yield
SCLC	Space Charge Limited Current
SEC	Size Exclusion Chromatography
SM	Small Molecule
TEM	Transmission Electron Microscopy
THF	Tetrahydrofuran
TIPS	Triisopropylsilyl
TOF	Time of Flight
TTA	Triplet-Triplet Annihilation
UV-Vis	Ultraviolet-visible
V_{max}	Maximum Output Voltage

V_{oc}	Open-circuit Voltage
XRD	X-ray Diffraction
λ	Wavelength
δ	Chemical Shift
3D	Three-dimensional

Chapter 1

Introduction

1.1 Overview

It is clear that the current energy regimen, which relies on combustion of nonrenewable fossil fuels, has caused two great global problems: the increasingly serious environmental pollution and the expected depletion of fossil fuels.[1] As a result, the energy and environmental crisis pushed our community to look for an alternative energy source which should be environmentally friendly with less or zero greenhouse gas emission, renewable, and economically viable.[2] Among all the alternatives, solar energy is a bountiful renewable and clean energy resource since the energy in the sunlight that reaches Earth in an hour exceeds the energy consumed by all of humanity in a year[3] and in addition, according to Annual Energy Outlook 2015 compiled by US Energy Information Administration, solar energy is the fastest-growing energy source for renewable generation, at an annual average rate of 6.8%.[4] Therefore, in order to harness the solar energy, more and more efforts have been devoted to the development of solar cells which are devices directly converting sunlight into electricity. Currently, the silicon-based inorganic solar cells whose power conversion efficiencies (PCEs) have reached more than 20% dominate the market, however the rigidity and the high cost of such solar cells prevented them being widely accepted.[5] On the other hand, the organic photovoltaics (OPVs) including polymer solar cells,[6,7] small molecule solar cells,[8,9] dye-sensitized solar cells[10,11] and perovskite solar cells[12,13] have drawn great attention due to their potential to lower the cost. In particular, organic polymer and small molecule solar cells have advantages in their light-weight nature, flexibility and

amenability to printing electronic techniques for massive production scales including roll-to-roll processing and ink-jet printing.[14] Furthermore, the powerful synthetic methodology can endow the organic polymers and small molecules with versatile structures and functionalities[6] which is extremely important since it is possible for us to synthesize different compounds in order to find the desired properties.

1.2 Basics of Organic Solar Cells

1.2.1 The Evolution of Organic Solar Cells

Although the phenomenon known as the organic photovoltaic effect was discovered a long time ago, the real first milestone in the field was set by Tang in 1985.[15] In his pioneer work, the authors deposited two layers of copper phthalocyanine (donor) and perylene tetracarboxylic derivative (acceptor) through vacuum evaporation and both layers were sandwiched by indium tin oxide (ITO) coated glass and opaque Ag layer which were regarded as anode and cathode respectively. The devices were measured with PCEs around 1% which was much higher than any examples reported before. However, the bilayer structure (Fig. 1.1A) suffered a serious problem since the conversion efficiency in such architecture is limited and efficient charge separation only occurs at the Donor-Acceptor (D-A) interface; thus, photoexcitations created far from the D-A junction recombine before diffusing to the heterojunction.[16] After 10 years, the first soluble fullerene derivative phenyl-C_{61}-butyric acid methyl ester ($PC_{61}BM$) was synthesized and characterized by Wudl et al. in 1995,[17] which guaranteed the higher concentration of acceptors in the solution. As a result, at the same year, Yu et al. proposed a novel concept known as the bulk heterojunction (BHJ) (Fig. 1.1B) which will ideally create a bicontinuous

interpenetrating phase-separated D-A network, leading to the largest interfacial interaction between the donor and acceptor .[16,18] In this paper, the authors prepared a

Figure 1.1 Simplified illustrations (A) bilayer structure of organic solar cells where electron acceptors are atop the electron donors; (B) bulk-heterojunction (BHJ) morphology in which the electron donors and electron acceptors are mixed intimately as the active layer. Adapted the copyright of Ref.[18] Copyright (2014), The Royal Society of Chemistry.

mixed solution of conjugated polymer poly (2-methoxy-5-(2'-ethyl-hexyloxy)-1,4-phenylenevinylene) (MEH-PPV) with pure fullerene or its derivative $PC_{61}BM$. The active layer was obtained through the spin-coating of the above solution and the solar cell performances measured as a result of the method were boosted to as high as 2.5%. Since then, the concept of BHJ was widely accepted as state-of-art technology for organic solar cells.[19] Nevertheless, the large bandgap (~2.3 eV) and amorphous nature of PPV prevented this type of polymer from being further considered as a promising donor candidate. In order to find an ideal replacement for PPV, great efforts had been made to synthesize novel conjugated polymers. In 2005 a benchmark polymer poly (3-hexylthiophene) (P3HT) was invented and the system of P3HT/PCBM was optimized to have the power conversion efficiencies as high as 5%.[20–22] In addition, such solar cell devices had been stayed as the standard model for various investigations including detailed mechanism study and

photophysical study.[23–25] However, after several years' research, people found there is no room for pushing the PCEs of P3HT further because of its moderate bandgap (~1.9 eV). As a matter of fact, another so called push-pull conjugated polymers with low bandgaps (around 1.4~1.7 eV) came into play and these type of polymers have extended photon absorption bands and thus improved the efficiencies of solar cells.[26] The synthesis of these polymers was based on using transition metal catalyzed cross coupling reactions and some of these polymers—e.g. PTB7[27] and PDTP-DFBT[28] —when mixed with $PC_{61}BM$ had the PCEs around 10%. As a result, this field has grown very fast and the efficiencies have increased from 1% to 10% in the last 20 years. However, there is still a lot of room for improvement in order to reach the PCEs around 15% the level at which industry experts will consider organic solar cells to be cost-effective.[29]

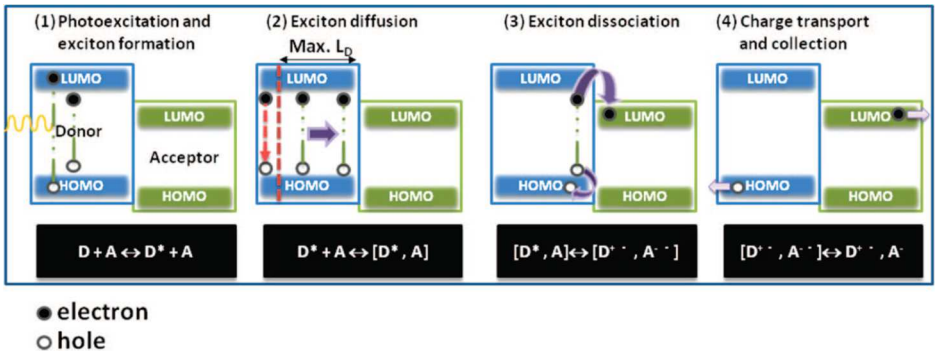

Figure 1.2 The working mechanism for donor-acceptor organic solar cells. Adapted the copyright of Ref.[6] Copyright (2009), American Chemical Society.

1.2.2 The Mechanism of Organic Solar Cells

The mechanism of OSCs is shown in Fig. 1.2. Specifically, the organic solar cells are sandwiched in structure, with different layers stacked with each other. Of these layers the most important one is the active layer in the middle which is composed of a donor phase

(conjugated polymers or small molecules) and an acceptor phase (PCBM). When the donor part is exposed to light, because of its low dielectric constant, an electron-hole pair called an exciton will be created instead of forming free electrons and holes. After the exciton migrate to the interface of donor and acceptor through Forster Resonance Energy Transfer (FRET), the excitons will be dissociated into free electrons and holes. Finally, the free charge carriers will transport to the respective electrodes in the opposite direction with the aid of the internal electric field, which in turn generates the photocurrent and photovoltage.[6]

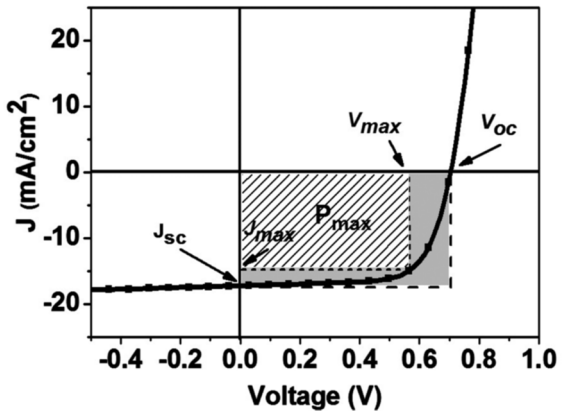

Figure 1.3 I-V curve and parameters in OSCs. Adapted the copyright of Ref.[1] Copyright (2015), American Chemical Society.

1.2.3 The Measurement of Organic Solar Cells

Efficiencies of OSCs named Power Conversion Efficiencies (PCEs) were evaluated by the I-V measurement under simulated sunlight illumination.[7,30,31] A typical I-V curve is shown Fig. 1.3, and the PCEs can be calculated through the following equation: $PCE = \frac{V_{oc} \times J_{sc} \times FF}{P_{in}}$, where FF stands for fill factor which is sensitive to the morphology of the active layer and can be calculated as $FF = \frac{V_{max} \times J_{max}}{V_{oc} \times J_{sc}}$. V_{oc} refers to the open-circuit voltage, which is proportional to the energy difference between the LUMO of the acceptor and the HOMO of the donor.[32–34] J_{sc} is the short-circuit current, and can be optimized through various

parameters including the amount of absorbed photons, the recombination rate of excitons and the charge mobilities of free carriers in the active layer.[35] Finally, the P_{in} is the power input of the incident light which can be calculated from the power density and active device area.

1.2.4 The Optimization of Organic Solar Cells

a Bandgap

The first parameter that comes into our mind is the adsorption range of the conjugated polymers or small molecules (bandgap) which should be ideally matched with the solar spectrum, however in the early stages of the OSCs, the polymer candidates such as PPV and P3HT had relatively large bandgaps which prohibited their further application in this field.[16,20] Therefore, with the help of various Pd catalysts, more and more research has been focused on the development of novel donor-acceptor polymers with lower bandgaps. As a result, when some candidates used as the donor in OSCs, the efficiencies can reach more than 10%.

b Interface Layers

Besides the importance of active layer in the OSCs, the anode interfacial layer (AIL) or cathode interfacial layer (CIL) also play a significant role in the performance of the solar cells (Fig. 1.4).[36] So far reported in the literatures, the most commonly used AILs include PEDOT: PSS,[37] MoO_3 and other metal oxide,[38] Graphene Oxide[39] as well as various small molecules[40,41]. On the other hand, the most frequently applied CILs contain metal oxide (ZnO, TiO_x, Nb_2O_5 and SnO_x),[42–45] water/alcohol soluble conjugated polymers,[46–48] low work function metal (Ca, Mg, etc.)[49,50] and metal salts (LiF, Cs_2CO_3, etc.),[51,52] as well as

carbonaceous materials.[53,54] These interfacial layers are widely used in multiple ways such as: to tune the energy level alignment,[55–57] to adjust the built-in electric field,[55–58] to improve charge selectivity[59,60] and the stability between the electrode and active layer[38,61] in order to further boost the PCEs of the solar cells

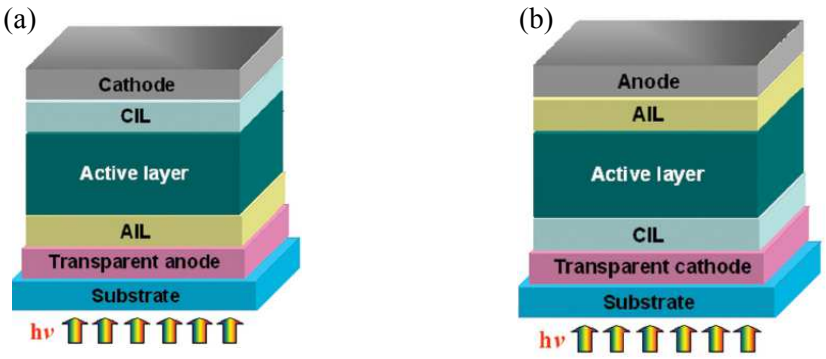

Figure 1.4 Simplified illustrations (a) Conventional architecture of organic solar cells; (b) Inverted architecture of organic solar cells. The two figures were obtained from open access article Ref. [36]

c Morphology

Since the organic compounds (donor materials) have relatively low dielectric constants, the product of light excitation is in the form of the highly-bounded excitons instead of free charge carries which leads to the limited diffusion length of such excitons of around 10-20 nm.[6] In order to utilize as many excitons as possible in the OSCs, the domain size of the organic compounds applied, or in other words the length the excitons will travel in such materials should be located within this distance otherwise the excitons will recombine before they can be captured.[16] As a result, a good morphology of the donor/acceptor blends providing ideal domain sizes and interconnected charge transport pathways is crucial to the success of organic solar cells.

Right now, there are several methods have been applied to optimize the morphology of the active layer such as adjustment of the weight ratio between the polymers or small molecules and PCBM,[62] the choices of the spin-coating solvents,[63] thermal annealing,[64–66] solvent annealing[67–71] and the use of additives.[72]

The weight ratio between donor and acceptor can control the morphology of the active layer to a certain extent. Usually, the crystalline donor will have less PCBM in the mixture such as 1:1 to 1:2, because the donors with high crystallinity tend to aggregate by themselves and smaller amount of PCBM is enough to create bicontinuous pathways,[20] while the amorphous one should have much higher loading of PCBM like 1:3 to 1:4 since the donor and acceptor have a tendency to mix with each other, more PCBM is needed to provide the continuous pathway.[73]

An ideal solvent for the spin-coating should not only dissolve both donor and acceptor at the same time but also control the phase separation during the spin-coating process where the evaporation rate is the key.[72] Technically speaking, the low boiling point or fast evaporation solvent such as chloroform tend to form well-mixed morphology between the donor and acceptor. On the other hand, the high boiling point or slow evaporation solvent including chlorobenzene or dichlorobenzene will form a less-mixed morphology since both donor and acceptor have much longer time to crystallize and aggregate during the evaporation time. As a result, it is better for highly crystalline donors, particularly conjugated small molecules to have low boiling point solvent in the spin-coating process in order to obtain a good morphology.[63] However, in terms of donors with amorphous nature, high boiling point solvent will be the first choice.[62]

The thermal annealing has proved to be an excellent post-treatment method to increase the PCEs. Specifically, after deposition of the metal cathode, the devices were heated at a given temperature for various amount of time and then left to cool down in order to obtain the best performances. The reason to apply such methodology is because the thermal annealing is supposed to remove the residual solvent in the blend film, to create percolated pathways by promoting the crystallizations of donors and acceptors through enhanced phase separation, and finally to increase the contact between the blends and the metal electrodes.[74,75]

The solvent annealing on the other hand will expose the as-cast films to solvent vapor such as chloroform or chlorobenzene in a container for a certain period of time. The role of solvent annealing is to slowly control the crystallization and phase separation of the donor and acceptor in the active layer and then create a suitable network with enhanced charge mobilities. [69–71]

Finally, adding additives into blend solution is also an effective way to improve the PCEs. A guideline can be followed to select additives, which is the additives are typically less volatile with higher boiling points solvents or compounds which have selective solubility to one of the components (typically the acceptor).[72] Through use of additives, we can expect the donor will precipitate out first with the evaporation of the solvent while the acceptor will still remain with the additives and solidify later to form an ideal phase separation.[76,77]

1.3 Pt-Containing Conjugated Polymers and Small Molecules Used in the OSCs

The introduction of a metal into conjugated polymers or small molecules is a promising but less explored method.[78,79] By doing so, we can harvest both the advantages of metals and conjugated polymers. Among various metal-containing conjugated polymers, Pt-containing conjugated polymers are of particulate interest. The main reason for introducing the Pt is to transfer the singlet exciton to triplet exciton through intersystem crossing by using the spin-orbital coupling effect with help of heavy metal Pt. The triplet exciton because of its parallel electron spin has life time longer than 1 μs and this factor will greatly increase the diffusion length of such exciton.[79] According to the calculation of Schanze et al.,[80] the diffusion length of triplet exciton can reach 100 nm in the ideal conditions which is about 5-10 times higher than that of singlet exciton. As a result, if the triplet exciton can contribute in the OSCs, the power conversion efficiencies of the solar cells will be greatly enhanced.

The work of organic solar cells regarding Pt-containing conjugated polymers was pioneered and most contributed by Wong et al.[73,79] The first paper was published in Nature Materials in 2007 and the structure of Pt-containing conjugated polymers was shown in Fig. 1.5. Specifically, a desired chromophore with the functionalization of a terminal alkyne on both sides was synthesized first and the Pt with tri-^{n}butyl phosphine used as the ligand, link to the triplet bond through a coordination reaction after polymerization. By choosing different chromophores in the middle, various Pt-containing conjugated polymers have been synthesized and applied as the donor in the organic solar cells and some promising results have been obtained.[81–84]

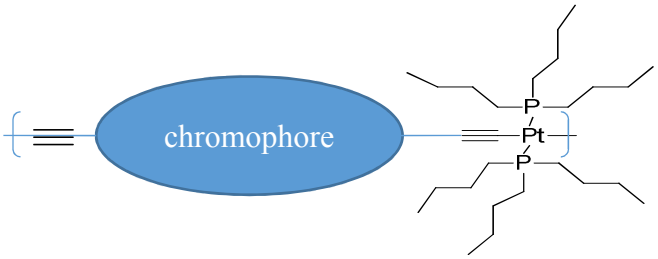

Figure 1.5 The structure of Pt-containing conjugated polymer

1.5 The Motivation of My Projects

The average PCEs for Pt-containing conjugated polymers in the OCSs reported so far are around 1-2%. After doing a literature search, it was found that in order to achieve low band-gap conjugated polymers, chromophores with long conjugated lengths are usually applied based on the concept of particle in a box. However, such a design will inevitably dilute the spin-orbital coupling effect which will finally influence the formation of triplet excitons. Therefore, in my first project, we proposed using Bodipy combined with Pt in the conjugated polymer, since the Bodipy possesses the compact size, ease of synthesis and high fluorescence quantum yield. However, the low band-gap Bodipy-Pt conjugated polymer, when applied as donor in OSCs, still suffered the poor power conversion efficiencies. Based on the UV-Vis, DSC, XRD and TEM image characterizations, we were able to determine that this polymer was of an amorphous nature. In addition, through the careful analysis of all Pt-containing conjugated systems, we found all the existing examples possess a dumb bell shape, (Figure 1.6 A) however, this shape can effectively prevent π-π stacking of the compounds which ultimately results in the amorphous feature. Unfortunately, the amorphous nature of these compounds leads to bad morphology within the active layer and increase the recombination rate of excitons which results in a poor performance in the organic solar cells.

In order to solve this problem, in my next two projects, we proposed a new "roller-wheel" shaped structure (Figure 1.6 B) by moving the Pt motif from the main chain to the side chain. This novel structure can increase the crystallinity of compounds through so-called slip-stack packing which will result in a good morphology in the active layer as well as increase the hole mobility of the compounds. As a result, the power conversion efficiencies, when mixing the new Pt-SM and Pt-SM-BTD with the $PC_{71}BM$, can reach from 3% to 6% which outperforms most examples in the OPVs. However, during the optimization process of the OSCs, we found the power conversion efficiencies will drop when the domain size in the active layer exceeded 5-10 nm which told us that less excitons were being captured by the PCBM in the solar cells. The reason for the decrease of the PCEs is possibly because the triplet excitons cannot be captured by the PCBM since the diffusion length of single exciton is about 5-10 nm— if the domain size is large than that, the single exciton will either recombine or be trapped in the T1 state of the Pt-containing small molecules.

In order to solve this mismatch between the triplet energy state (T_1) of the Pt-containing compounds and the LUMO level of fullerene acceptors.[85] We proposed a novel fullerene derivative with ionic nature in my final project since the cation in the fullerene can well stabilize the electron in the C_{60} which leads to a lower LUMO energy level. This new fullerene derivative named $C_{60}^{+}SDS^{-}$ is easy to synthesize and indeed possessed the lowest LUMO level compared to its neutral counterparts through the measurement of CV. Above all, we have successfully used time-resolved transient absorption spectrum to prove the $C_{60}^{+}SDS^{-}$ can actually capture the triple excitons of Pt-SM because the life time of triplet exciton decreased after adding the $C_{60}^{+}SDS^{-}$.

The future works for this project, to my understanding can be divided into the following directions: 1) Synthesis of new Pt-SM derivatives with higher T_1 state. 2) Synthesis of new C_{60} derivatives with a branched side chain in order to increase its solubility. 3) The application of organic solar cells using a blend of Pt-SM and $C_{60}^{+}SDS^{-}$.

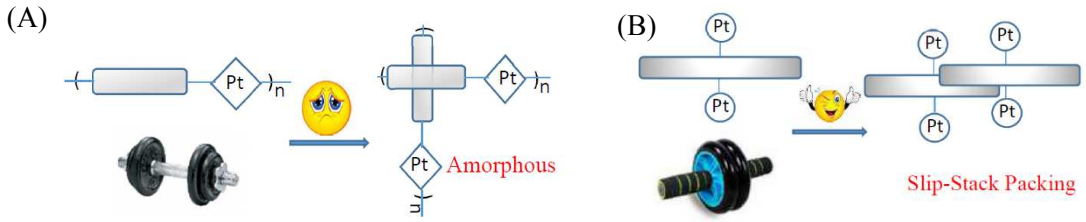

Figure 1.6 Simplified illustrations (A) Original designed Pt-containing organic solar cells with dumbbell shape; (B) New designed Pt-containing organic solar cells with roller-wheel shape.

Chapter 2

Synthesis and Photovoltaic Properties of a Low Bandgap BODIPY–Pt Conjugated Polymer

2.1 Introduction

The organic photovoltaics (OPVs) employing solution processable conjugated polymer with low bandgaps have been the subject of intensive research.[6,86–89] Incorporation of transition metals into conjugated polymer structures has been an intriguing strategy but less explored. In order to obtain organic materials with novel properties characteristic of metals, various transition metal complexes have been applied.[79,90–94] Among them, Pt(II) complexes are unique because they intrinsically adopt square planar geometries and their ability to serve as building blocks for linear conjugated systems.[95–98] The main reason to use such complexes is because their strong spin-orbital coupling effects can encourage the formation of long-lived triplet excitons through intersystem crossing, which have been considered beneficial for OPV operations.[99–104] As a result, more and more attention has been paid to the Pt-containing conjugated polymers in OPV research.[94,105–107] So far, several examples of conjugated polymers containing Pt(II)-diacetylenide building blocks have been reported and their photophysics and solar cell efficiencies were studied in detail.[81,108–113] Promising results around 3% have been observed in some cases applying such polymers as the donor in the OSCs.[73,84,114–117] The basic structures of Pt-containing polymers applied in OPVs are shown in Scheme 2.1. Specially, the chosen organic and organometallic chromophores are linked with transbis(trialkylphosphine)platinum diacetylenide building blocks through the coordination bond between the Pt and the triplet bonds. In addition, the electronic and photophysical properties of the final polymer, such

as bandgaps, HOMO and LUMO energy levels as well as triplet yields, are mainly governed by the nature of the chromophores. Typically, low bandgap conjugated polymers contain organic chromophores featuring several electron-rich and -poor aromatic moieties connected in series.[73,84,114–117] Therefore, Pt-containing polymers with low bandgap share the same manner of configuration, in such that they possess several aromatic rings side-by-side based on the concept of particle in a box.[118] However, such design will no doubt increase the chromophore sizes which can potentially dilute Pt induced spin-orbital coupling effects and lower triplet generation yields.[101]

Boron-dipyrromethene (Bodipy) dyes are a unique group of organic chromophores, which possess compact size, are easy to synthesis, and have large fluorescence quantum yields and tunable chemical/physical properties through well-established synthetic methodology.[119–123] Bodipy has been widely applied in the field of imaging techniques and protein labeling.[122,124] However, the application in the OPVs didn't happen until 2010, in that paper Rousseau et al. synthesized two different Bodipy derivatives which later were used as donors in the OSCs. The PCEs of the devices can reach as high as 2.2%.[125] Since then, extensive researches efforts have been made to synthesize various Bodipy compounds or polymers with different structures to be used as either donors or additives in the organic solar cells.[123,125–128] More recently, Chen et al. reported a bilayer organic solar cell instead of BHJ. When applying Bodipy as the donor, the obtained PCEs can be closed to 5%.[129] Thus, combing Bodipy and Pt-acetylenes building blocks into polymer structure, which has not been reported previously, provides new opportunities in OPV research.

We report herein the synthesis and photovoltaic properties of a novel low bandgap, solution processable conjugated polymer based on Pt-diacetylenide scaffolds and Bodipy chromophores.

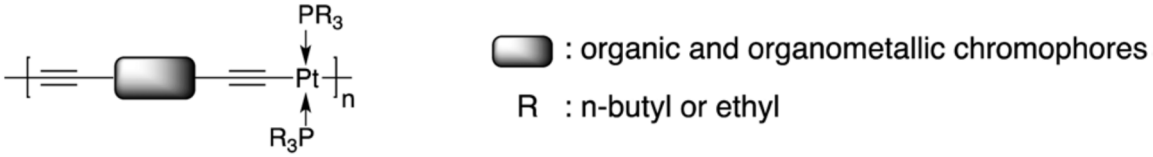

Scheme 2.1 Schematic representation of platinum containing conjugated polymers applied in organic photovoltaics

2.2 Results and Discussion

2.2.1 Synthesis of Monomers and Polymer

The summary of the synthesis of monomers and the BODIPY-Pt alternating polymer P1 is illustrated in Scheme 2.2. The trans-dichlorobis(tri-n-butylphosphine) platinum(II) (Pt1) was prepared according to reported procedures.[130–132] All synthetic intermediates were fully characterized by NMR spectroscopy and the monomer M1 was further confirmed by high resolution mass spectrometry (HRMS). The reaction of an equal molar amount of M1 and Pt1 in the mixture solvents of Et_3N/CH_2Cl_2 (1/2, v/v) at room temperature in the presence of a catalytic amount of CuI led smoothly to P1 within 12 h. P1 was collected through vacuum filtration as a purple powder after precipitation from the concentrated reaction mixture to methanol and purified by sequential Soxhlet extraction steps with methanol, acetone and chloroform. The molecular weight of P1 was determined by size exclusion chromatography (SEC, Fig. 2.1) against polystyrene standards. The number average molecular weight (Mn) was estimated to be 27 300 with a polydispersity index (PDI) of 2.1, corresponding to on average ca. 25 BODIPY or Pt repeating units along the polymer main-chain.

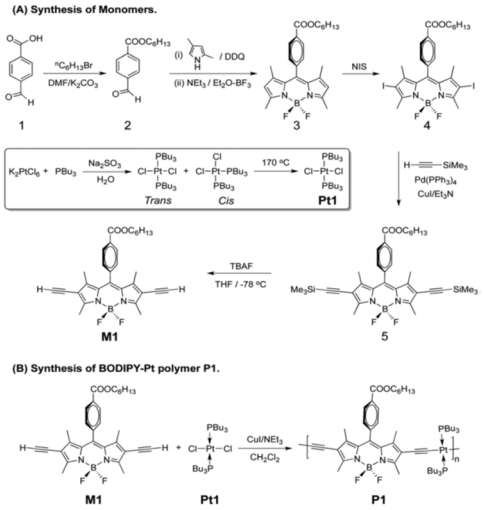

Scheme 2.2 Synthesis of monomers and polymer P1

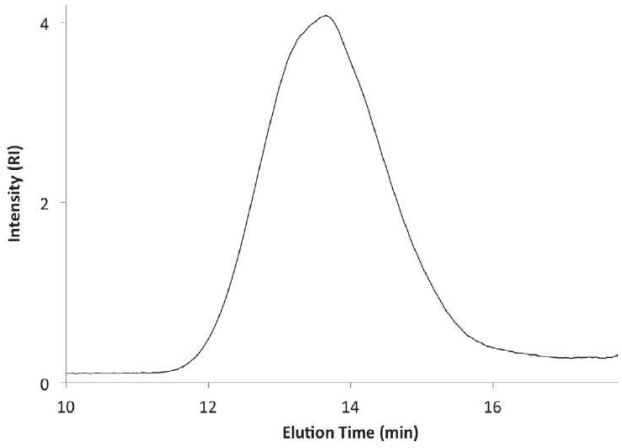

Figure 2.1 Size exclusion chromatography (SEC) profile of **P1** ($CHCl_3$, 1 mL/min, RI).

2.2.2 NMR Characterization of Polymer and Monomers

The structure of polymer P1 was fully characterized by multi-nuclear NMR spectroscopy as shown in Fig. 2. The ^{1}H NMR spectrum of P1 appears approximately as a superposition of spectra of M1 and Pt1, except for the complete disappearance of signal of terminal alkyne at 3.32 ppm, indicating the success of the polymerization. In addition, the signals of polymer are broader, less resolved and slightly up-field shifted. Integration of the P1 ^{1}H NMR spectrum leads to an equal ratio between BODIPY and $(^nBu_3P)_2Pt$ units along the polymer main-chain, suggesting the absence of any side reactions during polymer formation. ^{11}B NMR measurement of M1 gave a triplet at 0.2 ppm with a ^{1}JB–F constant of ca. 32 Hz (Fig. 2.2 A). Upon polymerization, the ^{11}B signal for P1 becomes broad and slightly downshifted 0.2 ppm. Both chemical shifts are typical for tetra-coordinated boron species,[133] suggesting a lack of unwanted side-reactions at these boron centers during

polymerization. Similar trends are observed in terms of ^{19}F NMR (Fig. 2.2 B). A quartet having a $^{1}JF–B$ constant of ca. 31 Hz is observed at -144.57 ppm for M1, while the signal for P1 up-field shifts to -145.34 ppm and becomes unresolved. In addition, the ^{31}P NMR spectrum of Pt1 has a pseudo triplet at 5.05 ppm with a large $^{1}JP–Pt$ constant of ca. 2380 Hz, on the other hand, the ^{31}P signal for polymer is around 3.76 ppm with a similar $^{1}JP–Pt$ constant of ca. 2366 Hz (Fig. 2.2 C). These chemical shifts and coupling constants are consistent with reported values in the literature.[85,132,134]

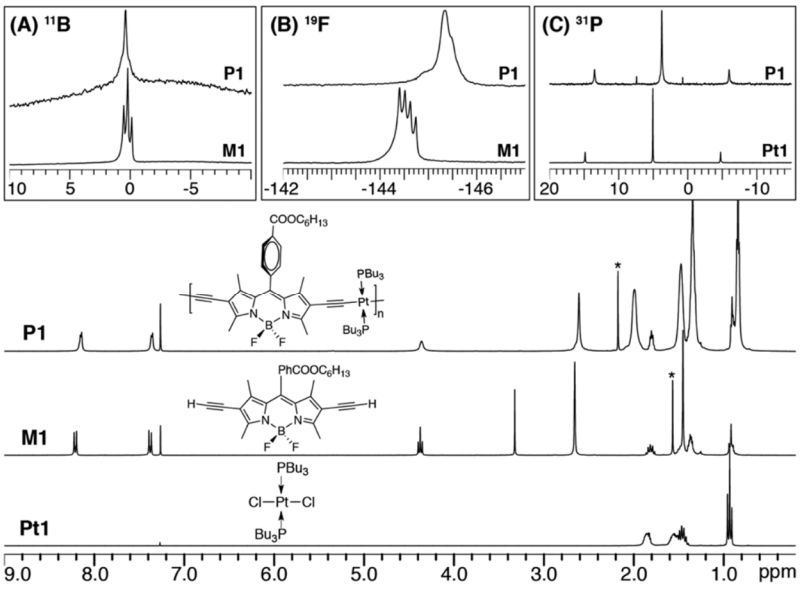

Figure 2.2 Overlay of ^{1}H NMR (300.13 MHz, $CDCl_3$) spectra of P1, M1 and Pt1 (signal marked with * are due to solvent impurities). Inset: (A) ^{11}B NMR (96.25 MHz, $CDCl_3$) spectra of P1 and M1; (B) ^{19}F NMR (282.4 MHz, $CDCl_3$) spectra of P1 and M1; (C) ^{31}P NMR (121.5 MHz, $CDCl_3$) spectra of P1 and Pt1. All scales are in ppm.

2.2.3 IR Characterization of Polymer and Monomers

IR measurements were used to further confirm the polymerization as shown in Fig. 2.3. The sharp absorption peak at ca. 3275 cm^{-1} corresponding to the C–H symmetric stretching

mode of terminal alkynes in M1 completely disappears in the spectrum of P1which is well agreed with the results of ^{1}H NMR. Furthermore, the signal due to the carbon–carbon triple bond stretching mode in M1 is very weak and appears at 2103 cm^{-1}. After polymerization, this signal in the spectrum of P1 is significantly enhanced and shifted to 2092 cm^{-1}, presumably caused by the attachment of heavy Pt atoms. Differential scanning calorimetry (DSC) were applied to evaluate the thermal properties of P1, however, no melting point could be observed in the temperature range from -50 °C to 250 °C, suggesting the amorphous nature of the polymer, which is consistent with other literature reports on conjugated polymers containing Pt-diacetylenide building blocks bearing $^{n}Bu_3P$ ligands.

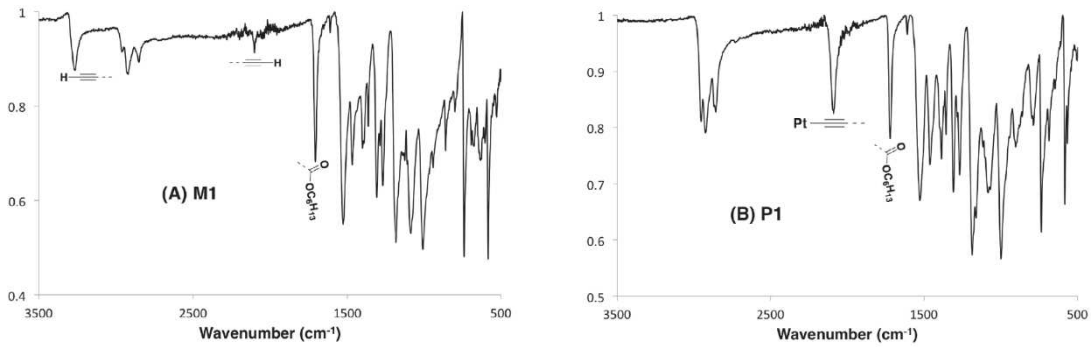

Figure 2.3 Attenuated total reflectance (ATR)-IR spectra of M1 (A) and P1 (B).

2.2.4 UV-Vis Absorption and Emission Spectra

Absorption and emission spectra of M1 and P1 both in solutions and as thin films are shown in Fig. 2.4. The maximum absorption (λ_{max}) of monomer M1 in dilute $CHCl_3$ solution is at 545 nm and emission maximum (λ_{em}) is at 560 nm when excited at 545 nm. A quantum efficiency of ca. 23% was estimated for M1. Sharp absorption and emission profiles, small Stoke's shift and high quantum efficiency of M1 are typical of BODIPY dyes.[119–123] Upon polymerization, both absorption and emission of P1 in dilute solution

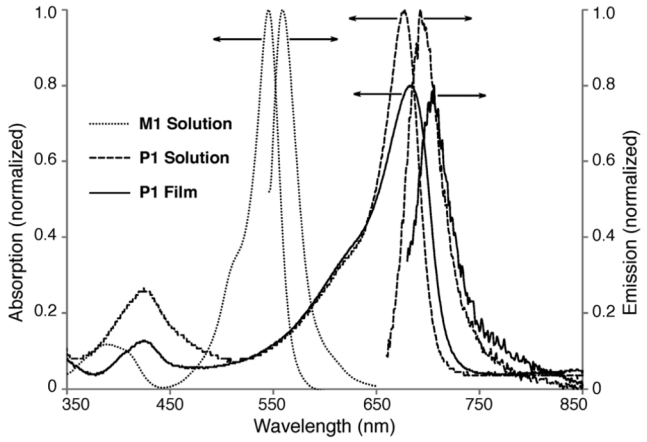

Figure 2.4 Normalized UV-Vis absorption (left axis) and emission (right axis) spectra of M1 in $CHCl_3$ (10^{-5}, dotted lines), P1 in $CHCl_3$ (10^{-5} M repeat units, dashed lines) and thin films of P1 (solid lines).

became broader and significantly red-shifted to 677 nm and 693 nm, respectively, since the Pt1 has participated the conjugation along the polymer main-chain. λ_{max} of P1 is also larger than those of similar bis-platinated BODIPY compounds bearing $^{n}Bu_3P$ ligands as reported by Zhao et al. (λ_{max} = 643 nm and λ_{em} = 671 nm),[135] indicating certain electron delocalization through the Pt-diacetylenide centers in P1. Resemblance of both absorption and emission spectra of P1 with those of M1, as well as the relatively small Stoke's shift ($\Delta\lambda$ = 16 nm), suggests that electronic transitions in P1 are intra-ligand (IL) in nature. The quantum yield of fluorescence in terms of P1 is greatly suppressed to ca. 0.3%, possibly due to the enhanced inter-system crossing caused by the presence of Pt centers. Unfortunately, no room temperature phosphorescence could be observed in deaerated solutions, which can be explained by the low bandgap of P1 and the energy gap law,[136] and is similar to the observations in the other Pt-containing low bandgap polymers reported in the literature.[73,114]Only a slight red-shift in both absorption and emission spectra is

observed in thin films of P1 (λ_{max} = 685 nm and λ_{em} = 706 nm) compared to those of solution profiles, which further confirms the amorphous nature of the polymer as suggested by DSC measurements. From the onset of the absorption, a bandgap of ca. 1.7 eV can be calculated for P1.

2.2.5 Cyclic Voltammetry Measurements

The HOMO and LUMO energy level of P1 can be obtained through cyclic voltammetry (CV) measurement on thin films of the polymer which revealed a non-reversible multi-step oxidation event and a very small non-reversible reduction peak (Fig. 2.5). From the onset the HOMO energy level of ca. -5.3 eV and a LUMO energy level of ca. -3.5 eV are estimated. This leads to an electrochemical bandgap of ca. 1.8 eV for P1, which is closed enough to the observed optical bandgap.

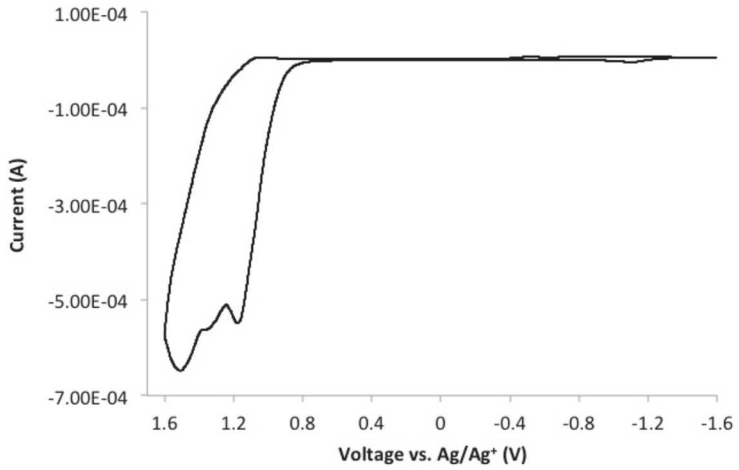

Figure 2.5 Cyclic voltammogram (CV) of P1 thin film drop-cast onto the glassy carbon working electrode (0.1 M Bu_4NPF_6 in acetonitrile as supporting electrolytes; 100 mV/s; externally referenced to ferrocene redox couple).

2.3 Solar Cell Performance

BHJ solar cells were initially fabricated employing P1 and phenyl-C_{61}-butyric acid methyl ester ($PC_{61}BM$) using a conventional device geometry of ITO/PEDOT: PSS/active

layer/Al. Different weight ratios between P1 and $PC_{61}BM$ were first tested in order to optimize the PCEs and the results are summarized in Table 2.1. However, the best device power conversion efficiency was only achieved around 0.21% using a P1/$PC_{61}BM$ ratio of 1/3 with a relatively low open circuit voltage (V_{OC}) of 0.57 V and a fill factor (FF) of 32%. We suspected that the anode interfacial layer, PEDOT: PSS, having a work function of ca. -5.0 eV (0.3 eV higher than the HOMO of P1)[137] might not be optimal in terms of energy level alignment with the HOMO of P1. We thus turned into thermally evaporated MoO_3, which has been extensively studied as an anode interfacial layer in OPVs and work functions matching or below the HOMO of P1 have been reported.[138–141] Indeed, by using 10 nm MoO_3 as the anode interfacial layer, VOCs of all devices significantly increased. A very high V_{OC} of 0.92 V is observed in the P1/$PC_{61}BM$ (1/2) devices but the overall PCEs are limited by low J_{SC} and FF. The best performances were achieved in devices applying P1/PCBM at 1/3 weight ratio, giving a high V_{OC} of 0.86 V and an average PCE of 0.91% (Fig. 2.6). The enhancement of V_{OC} around ca. 0.3 V correlates well with the difference between the work function of PEDOT: PSS and HOMO of P1, suggesting an Ohmic contact formation using MoO_3.

Table 2.1 Device performance data for P1/PCBM

Anode	P1/$PC_{61}BM$[a]	V_{oc}[b] (V)	J_{sc}[b] (mA cm^{-2})	FF[b] (%)	PCE[b] (%)
PEDOT: PSS	1/1	0.23	0.23	31	0.03(0.04)
	1/2	0.50	0.55	27	0.07(0.08)
	1/3	0.57	1.13	32	0.21(0.25)
	1/4	0.62	0.98	31	0.19(0.20)
MoO_3	1/1	0.92	0.91	26	0.22(0.25)
	1/2	0.86	2.23	48	0.91(0.99)
	1/3	0.84	2.13	48	0.86(0.92)

[a] Weight ratio. [b] Average over five devices; the best PCEs are given in parentheses.

PCEs are still limited by the relatively small J_{SC} (2.2 mA cm^{-2}) and FF (48%). Some possible reasons such as unfavorable morphology and poor charge transport due to the polymer's amorphous nature might be account for the poor performance. Transmission electron microscopy (TEM) images of active layers from the best performing devices using PEDOT: PSS (Fig. 2.7) show no obvious phase separation between P1 and PCBM. Furthermore, thermal annealing seemed to have no significant, sometimes negative, effects on device performance, presumably due to high polymer fullerene miscibility and low polymer crystallinity. The large, cone-shaped $^{n}Bu_3P$ ligands is the main reason for the polymer's amorphous nature since it can effectively prevent polymer chain close-packing. By using planar ligands that are still capable of forming stable complexes with Pt-diacetylenides, more crystalline polymers and better performing devices nature can be expected. Another possibility to account for the low PCEs is non-optimal energy level alignment between donor triplet states and acceptor molecules and unfavorable charge transfer dynamics since the triplet states of P1 will become the dead end for the excitons. Detailed photophysical studies on P1 at ambient and cryogenic conditions, as well as investigations on charge generation/separation phenomena at the organic/organic interfaces, are currently underway.

2.4 Conclusion

In summary, a novel BODIPY and platinum containing conjugated polymer, P1, possessing low bandgaps was prepared. OPV devices employing P1 and PCBM were fabricated and evaluated. Commonly applied anode interfacial layer PEDOT: PSS was found to be not an ideal candidate due to the deep lying HOMO level of P1 at -5.3 eV, however, thermally evaporated MoO_3 formed ohmic contact leading to high V_{OC}s. Detailed

studies on photophysical properties of the polymer and charge generation mechanisms in polymer/fullerene blends are currently being carried out. Replacing $^{n}Bu_3P$ ligands on Pt centers with less sterically demanding ones is expected to increase crystallinity of these platinum-containing polymers thus improving device performances.

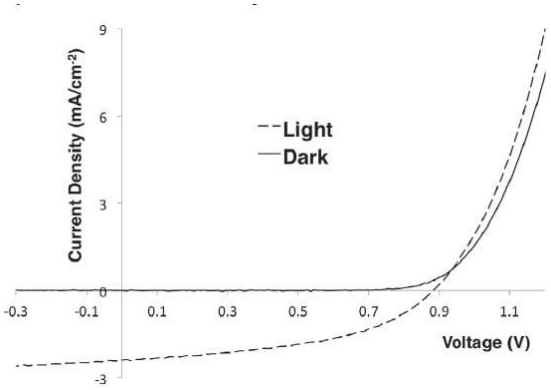

Figure 2.6 Current-Voltage (I-V) curves of the best performance device

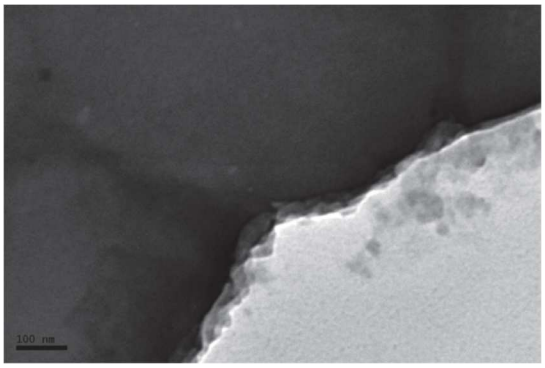

Figure 2.7 Transmission electron microscopy (TEM) image of the best performance device

2.5 Experimental

2.5.1 Materials and General Methods

All reagents and solvents were used as received from Sigma-Aldrich or VWR unless otherwise noted. Phenyl-C_{61}-butyric acid methyl ester (PCBM) was purchased from American Dye Source. trans-Dichlorobis(tri-n-butylphosphine) platinum(II) (Pt1) was synthesized according to previously reported procedures.[130–132] Anhydrous THF was distilled over Na/benzophenone prior to use. Anhydrous dichloromethane was obtained by distillation over CaH_2 and degassed through several freeze– pump–thaw cycles. 300.13 MHz ^{1}H, 75.48 MHz ^{13}C, 96.25 MHz ^{11}B, 121.5 MHz ^{31}P, and 282.4 MHz ^{19}F NMR spectra were recorded on a Bruker Avance III Solution 300 spectrometer. All solution ^{1}H and ^{13}C

NMR spectra were referenced internally to tetramethylsilane and ^{11}B, ^{31}P and ^{19}F NMR spectra were referenced by using external standards $Et_2O{\cdot}BF_3$ (0 ppm), H_3PO_4 (0 ppm) and C_6F_6 (-164.9 ppm), respectively. Size exclusion chromatography (SEC) analyses were performed in chloroform with 0.5% (v/v) triethylamine (1 mL min^{-1}) using a Waters Breeze system equipped with a 2707 autosampler, a 1515 isocratic HPLC pump and a 2414 refractive index detector. Two styragel columns (Polymer Laboratories; 5 mm Mix-C), which were kept in a column heater at 35 °C, were used for separation. The columns were calibrated with polystyrene standards (Varian). Infrared (IR) spectra were recorded on a Bruker Alpha-P instrument, using powder samples in ATR mode. Ultraviolet visible (UV-Vis) absorption spectra were measured on a Shimadzu UV-2401 PC spectrometer over a wavelength range of 240–1100 nm. Fluorescence emission spectra were obtained using a Varian Cary Eclipse Fluorimeter. Differential scanning calorimetry (DSC) measurements were performed on a Mettler Toledo DSC STARe system with a ca.8 mg sample and at a scan rate of 10 °C min^{-1}. The results reported are from the second heating cycle. Cyclic voltammetry was performed at 25 °C on a CH Instrument CHI604xD electrochemical analyzer using a glassy carbon working electrode, a platinum wire counter electrode and a Ag/AgCl reference electrode calibrated using a ferrocene redox couple (-4.8 eV). Transmission electron microscopy (TEM) images were taken on a JEOL 2010 EX HREM with an Oxford-Link EDS Gatan Digital Micrograph equipped with a slow scan CCD camera. Samples were prepared by soaking solar cell devices employing PEDOT: PSS as anode interfacial layers in water and fishing out floating active layers with carbon coated TEM grids. High resolution mass spectrometry (HRMS) was performed on a

Waters/Micromass LCT Premier system operating under electrospray ionization (ESI) mode. Elemental analysis was performed by ALS Life Sciences Division located in Tucson, Arizona.

2.5.2 Solar Cell Fabrication and Testing

P1/PCBM blend solutions were prepared by dissolving both P1 and PCBM at predetermined weight ratios in chlorobenzene at a polymer concentration of 0.5 wt% and stirred at 80 °C overnight in a nitrogen glove box (Innovative Technology, model PL-He-2GB, O_2 < 0.5 ppm, H_2O < 0.5 ppm) before device fabrication. Solar cell devices were fabricated according to the following procedure: ITO-coated glass substrates (China Shenzhen Southern Glass Display Ltd., 8 Ω $\square^{-1}$) were cleaned by ultrasonication sequentially in detergent, DI water, acetone and isopropyl alcohol, each for 15 min. These ITO-coated glass substrates were further exposed to UV-ozone (PSD Series, Novascan) for 60 min before being transferred to a nitrogen glove box (Innovative Technology, model PL-He-4GB-1800, O_2 < 0.1 ppm, H_2O < 0.1 ppm) for MoO_3 deposition. MoO_3 (10 nm) was deposited using an Angstrom Engineering Åmod deposition system at a base vacuum level of $<5 \times 10^{-7}$ Torr. The polymer/fullerene blend solution was first filtered through a 0.45 μm PTFE filter and spin-coated on top of the MoO_3 layer at 900 rpm for 45 s. Al (100 nm) was thermally evaporated through patterned shadow masks to serve as anodes. Current–voltage (I–V) characteristics were measured using a Keithley 2400 source-measuring unit under simulated AM1.5G irradiation (100 mW cm^{-3}) generated by a Xe arc-lamp based Newport 67005 150 W solar simulator equipped with an AM1.5G filter. The light intensity was calibrated using a Newport thermopile detector (model 818P-010-12) equipped with a Newport 1916-C Optical Power Meter.

2.5.3 Synthesis Details

Hexyl 4-formylbenzoate (2). In a 100 mL flask, 1.50 g of 4-formylbenzoic acid (10.0 mmol) and 2.76 g of potassium carbonate (20.0 mmol) were added together and dissolved in 30.0 mL dry DMF and then 4.20 mL 1-bromohexane (30 mmol) was added through a syringe. The reaction mixture was stirred for 12 hours at 70 °C. After cooling to r.t., the mixture was washed with H_2O and extracted with Et_2O for 3 times. The organic phases were combined and washed with brine and dried over anhydrous Na_2SO_4. After removal of all solvents through rotavapor, the product was purified by vacuum distillation (180 mTorr, 90–93 °C) as a colorless oil (1.98 g, 80% yield). ^{1}H NMR (300.13 MHz, $CDCl_3$): δ (ppm) = 10.10 (s, 1H), 8.18 (d, 2H), 7.96 (d, 2H), 4.35 (t, 2H), 1.79 (m, 2H), 1.33–1.48 (m, 6H), 0.91 (t, 3H). ^{13}C NMR (75.48 MHz, CDCl3): δ (ppm) = 191.5, 165.5, 139.0, 130.0, 129.4, 65.6, 31.3, 28.5, 25.6, 22.4, 13.9.

BODIPY (3). Compound 2 (1.20 g, 5.00 mmol) was dissolved in dichloromethane (300 mL) to which was added 2,4-dimethylpyrrole (1.00 mL, 10.0 mmol) and the mixture was degassed by three vacuum-N_2 refill cycles. 2-5 drops of trifluoroacetic acid (ca. 0.05 mL) were then added and the reaction was stirred at room temperature for 12 hours. The solution color gradually changed from yellow to deep wine-red over the course of the reaction. DDQ (1.14 g, 5.00 mmol) was then added into the solution. After stirring for 1 hour, 10.0 mL triethylamine (57.0 mmol) was added and the reaction mixture was stirred for another 20 min. Finally, 10.0 mL boron trifluoride etherate (79.0 mmol) was added and the reaction was allowed to proceed at room temperature for another 2 h. Solvents were removed under reduced pressure and the residue was first washed with H_2O and then extracted with dichloromethane. The organic phase was combined and washed with brine, dried over

anhydrous sodium sulfate and concentrated under reduced pressure. Compound 2 was purified by silica gel chromatography with hexane-ethyl acetate as a dark red solid (0.850 g, 37.8% yield). ^{1}H NMR (300.13 MHz, $CDCl_3$): δ (ppm) = 8.18 (d, 2H), 7.40 (d, 2H), 5.99 (s, 2H), 4.36 (t, 2H), 2.56 (s, 6H), 1.81 (m, 2H), 1.47 (m, 6H), 1.38 (s, 6H), 0.91 (t, 3H). ^{13}C NMR (75.48 MHz, $CDCl_3$): δ (ppm) = 166.0, 155.9, 142.8, 140.2, 139.6, 131.1, 130.9, 129.9, 128.3, 121.4, 65.5, 31.4, 28.6, 25.7, 22.5, 14.5, 13.9.

2,6-Diiodo-BODIPY (4). BODIPY 3 (452 mg, 1.00 mmol) was dissolved in 18.0 mL dichloromethane and the flask was purged with N_2. A solution of N-iodosuccinimide in anhydrous DMF which had been degassed for 20 min was slowly added to the flask via a syringe. The reaction mixture was vigorously stirred for 12 hours at room temperature. After the reaction finished, dichloromethane was evaporated under reduced pressure. The residue was washed with H_2O and extracted with dichloromethane. The organic layer was washed with brine, dried over anhydrous sodium sulfate and concentrated under reduced pressure. BODIPY 3 was purified by silica gel chromatography with hexane dichloromethane as a red solid (370 mg, 52.5% yield). ^{1}H NMR (300.13 MHz, $CDCl_3$): δ (ppm) = 8.22 (d, 2H), 7.38 (d, 2H), 4.37 (t, 2H), 2.65 (s, 6H), 1.81 (m, 2H), 1.50 (m, 6H), 1.39 (s, 6H), 0.92 (t, 3H). ^{13}C NMR (75.48 MHz, $CDCl_3$,): δ (ppm) = 165.8, 157.3, 145.1, 139.9, 139.3, 131.7, 130.8, 130.5, 128.2, 65.7, 31.4, 28.6, 25.7, 22.5, 17.1, 16.0, 14.0.

2,6-Bis(trimethylsilylethynyl)BODIPY (5). BODIPY 4 (176 mg, 0.250 mmol) was placed in a pressure vessel equipped with a magnetic stir bar. The flask and its contents were transferred to a glove box under an argon atmosphere. $Pd(PPh_3)_4$ (14.4 mg, 5.00 mol%) and CuI (10 mg, 20.0 mol%) were added to the pressure vessel under argon. Triethylamine (1.50 mL, 10.0 mmol), trimethylsilylacetylene (0.100 mL, 0.700 mmol) and toluene (5.00

mL) were then added to the vessel. The pressure vessel was sealed and taken out of the glove box. The reaction was carried out at 90 °C for 6 h. After cooling to room temperature, the solvent was removed under reduced pressure. BODIPY 5 was purified by silica gel chromatography with hexane–dichloromethane as a red solid (147 mg, 91.7% yield). ^{1}H NMR (300.13 MHz, $CDCl_3$): δ (ppm) = 8.21 (d, 2H), 7.37 (d, 2H), 4.37 (t, 2H), 2.63 (s, 6H), 1.81 (m, 2H), 1.43 (s, 6H), 1.37 (m, 6H), 0.94 (t, 3H), 0.20 (s, 18H).

2,6-Diethynyl-BODIPY (M1). BODIPY 5 (147 mg, 0.230 mmol) was dissolved in THF (4.00 mL), purged with N_2 and the solution was cooled to -78 °C. A solution of tetrabutylammonium fluoride in THF (1 M, 1.15 mL, 1.15 mmol) was added dropwise via a syringe. The reaction mixture was then removed from the cooling bath and stirred at room temperature for 2 h. The solvent was removed under reduced pressure and the crude product was washed with H_2O and extracted with dichloromethane. The organic layer was combined and washed with brine, dried over anhydrous sodium sulfate and concentrated under reduced pressure. M1 was purified by silica gel chromatography with hexane–dichloromethane as a red solid (34.5 mg, 30% yield). ^{1}H NMR (300.13 MHz, $CDCl_3$): δ (ppm) = 8.22 (d, 2H), 7.40 (d, 2H), 4.37 (t, 2H), 3.32 (s, 2H), 2.65 (s, 6H), 1.81 (m, 2H), 1.39 (s, 6H), 1.37 (m, 6H), 0.91 (t, 3H). ^{13}C NMR (75.48 MHz, $CDCl_3$): δ (ppm) = 165.8, 159.3, 145.2, 138.8, 131.6, 130.5, 128.1, 115.4, 84.3, 75.6, 65.7, 31.4, 28.6, 25.7, 22.5, 14.0, 13.5, 13.4. 11B NMR (96.25 MHz, $CDCl_3$): δ (ppm) = 0.198 (t, JB–F = 29.3 Hz). ^{19}F NMR (282.4 MHz, $CDCl_3$): δ (ppm) = -144.4 (q, JF–B = 31.0 Hz). HRMS: (ESI): $C_{30}H_{31}BF_2N_2O_2$, calcd, 501.2525 for $[M + H]^+$; found, 501.2527 for $[M + H]^+$.

Polymer P1. BODIPY M1 (300 mg, 0.600 mmol), trans-$[PtCl_2(P(C_4H_9)_3)_2]$ (Pt1, 402 mg, 0.600 mmol), CuI (22.8 mg, 0.120 mmol) and Et_3N-CH_2Cl_2 (90.0 mL, 1: 2, v/v) were

charged in a pressure vessel under argon and sealed before taken out of the glovebox. After stirring at room temperature overnight, the reaction mixture was evaporated to dryness. The residue was purified by Soxhlet extraction sequentially using methanol, acetone and chloroform. After concentration of the chloroform solution, the purple solid was collected by filtration after the precipitation into a large excess of methanol. Subsequent washing with copious methanol and drying under high vacuum gave the targeted polymer (P1) as a purple solid (590 mg, 89.6% yield). ^{1}H NMR (300.13 MHz, $CDCl_3$): δ (ppm) = 8.14 (2H), 7.35 (2H), 4.36 (2H), 2.60 (6H), 1.99 (14H), 1.80 (2H), 1.34–1.47 (45H), 0.84 (26H). ^{13}C NMR (75.48 MHz, $CDCl_3$): δ (ppm) = 166.3, 157.4, 140.4, 139.1, 137.7, 130.8, 130.3, 130.0, 128.6, 121.7, 65.7, 31.4, 28.6, 26.3, 25.7, 24.3, 24.2, 24.1, 23.8, 23.6, 23.4, 22.5, 13.9, 13.8, 13.4. ^{11}B NMR (96.25 MHz, $CDCl_3$): δ (ppm) = 0.369. ^{31}P NMR (121.5 MHz, $CDCl_3$): δ (ppm) = 3.75 (JP–Pt = 2366 Hz). ^{19}F NMR (282.4 MHz, $CDCl_3$): δ (ppm) = -145.3. SEC ($CHCl_3$, 1 mL min^{-1}, RI): Mn = 27 300, Mw = 57 300, and PDI = 2.1. IR (attenuated total reflectance mode): ν (cm^{-1}) = 2956, 2929, 2860, 2092, 1723, 1530, 1311, 1270, 1187, 999, 736, 583. Elemental analysis ($C_{54}H_{83}BF_2N_2O_2P_2Pt$): calcd: C 59.06%, H 7.62%, N 2.55%, and Pt 17.77%; found: C 57.86%, H 7.87%, N 2.70%, and Pt 18.34%.

Chapter 3

A "Roller-Wheel" Pt-containing Small Molecule That Outperforms Its Polymer Analogs in Organic Solar Cells

(Reproduced from *Chemical Science* **2016**, 7, 5798-5704. with permission from the Royal Society of Chemistry

The other authors Maksim Y. Livshits, Diane A. Dickie, Jianzhong Yang, Rachel Quinnett, Jeffrey J. Rack, Qin Wu and Yang Qin are acknowledged.

Supporting information of the publication is incorporated in this chapter)

3.1 Introduction

Organic solar cells (OSCs) have been widely perceived as low cost alternative energy sources that possess unique properties including light-weight, flexibility and semi-transparency.[142] State-of-the-art OSCs, with power conversion efficiencies (PCEs) now beyond 10%,[8,142–148] contain blends of an organic light-absorbing electron donor and a fullerene derivative as the electron acceptor, forming bulk heterojunction (BHJ) morphologies that play a decisive role on device performance.[14,149]Steady improvements in OSC efficiencies have resulted mainly from rational design and synthesis of conjugated donor materials,[6,89] interfacial engineering,[150,151]novel device geometries,[152,153]as well as morphology optimization via Edisonian approaches including thermal/solvent annealing and additives.[154,155]Another intriguing but less explored strategy is to incorporate heavy metals into the organic materials, leading to facile formation of triplet excitons. The extended lifetimes and thus longer diffusion lengths of triplet excitons have been suggested

to improve the charge separation efficiency.[80,156–163]Among the various examples of metal containing materials applied in OSCs, conjugated polymers (CPs) containing main-chain Pt-bisacetylide moieties, having the general structures shown in Scheme 3.1A, are the most studied.[105,106,164] Besides a handful of examples showing moderate PCEs of ca. 2–4%,[73,81,82,112,114] most such Pt-containing CPs display relatively low performance, which has been mainly ascribed to their intrinsic amorphous nature, resulting in low conductivity and unfavorable BHJ morphologies.[62,109,111] Although less explored in OSC applications, conjugated small molecules (SMs) can be highly crystalline and thus have superior charge mobilities, as well as discrete and reproducible molecular structures.[165,166] These features have attracted increasing attention and OSC devices employing conjugated SMs have been constantly improved to rival their CP counterparts.[146,167] On the other hand, conjugated SMs containing Pt-bisacetylides, having typical structures as shown in Scheme 3.1B, are mostly prepared as model compounds, resembling their polymeric analogs, for photophysical studies.[113,168] These SMs, similar to their polymeric analogs, possess "dumbbell" shaped molecular structures having bulky Pt groups at both ends of linear organic chromophores, resulting in inefficient molecular packing and π–π interactions.

We propose a new structural design, as shown in Scheme 3.1C, having Pt-bisacetylides as side-chains attached at the center of a rigid and linear conjugated chromophore. This "roller-wheel" shaped structure can allow partial overlap among adjacent chromophores in a slip-stacked fashion similar to that observed in symmetrically substituted acenes,[169,170] potentially enhancing crystallinity and conductivity. Herein, we report the synthesis, characterization and OSC application of such a "roller-wheel" molecule, Pt-SM that

generates PCEs up to ca. 5.9% in BHJ devices, the highest reported so far for Pt-containing SMs and polymers.

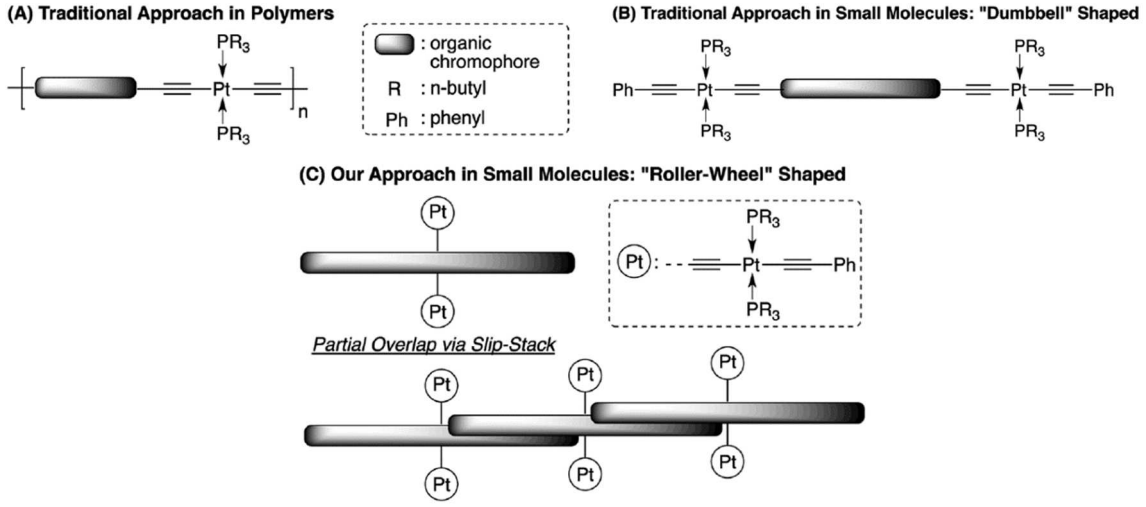

Scheme 3.1 Structure of Pt-bisacetylide materials

3.2 Results and Discussion

3.2.1 Synthesis of Pt-SM

Synthetic procedures toward the target compound Pt-SM are outlined in Scheme 3.2 and the structure of Si-SM, the nonmetallic analog to Pt-SM by replacing the Pt-containing moieties with triisopropylsilyl (TIPS) groups is also shown. Synthetic details are included in the Section 3.5.3 The alkyl side-chains on Si-SM are necessary for solution processability, since attempts to prepare Si-SM analogs having no side-chains at both terminal thiophene rings led to materials that are poorly soluble in common organic solvents and difficult to purify and analyze. On the other hand, the four bulky tri(n-butyl) phosphine ligands make Pt-SM readily soluble in common organic solvents such as $CHCl_3$, chlorobenzene, toluene and THF, etc., without the need for additional alkyl side-chains.

Pt-SM is fully characterized by ^{1}H, ^{13}C, ^{19}F and ^{31}P NMR spectroscopy, as well as high resolution mass spectrometry (HR-MS).

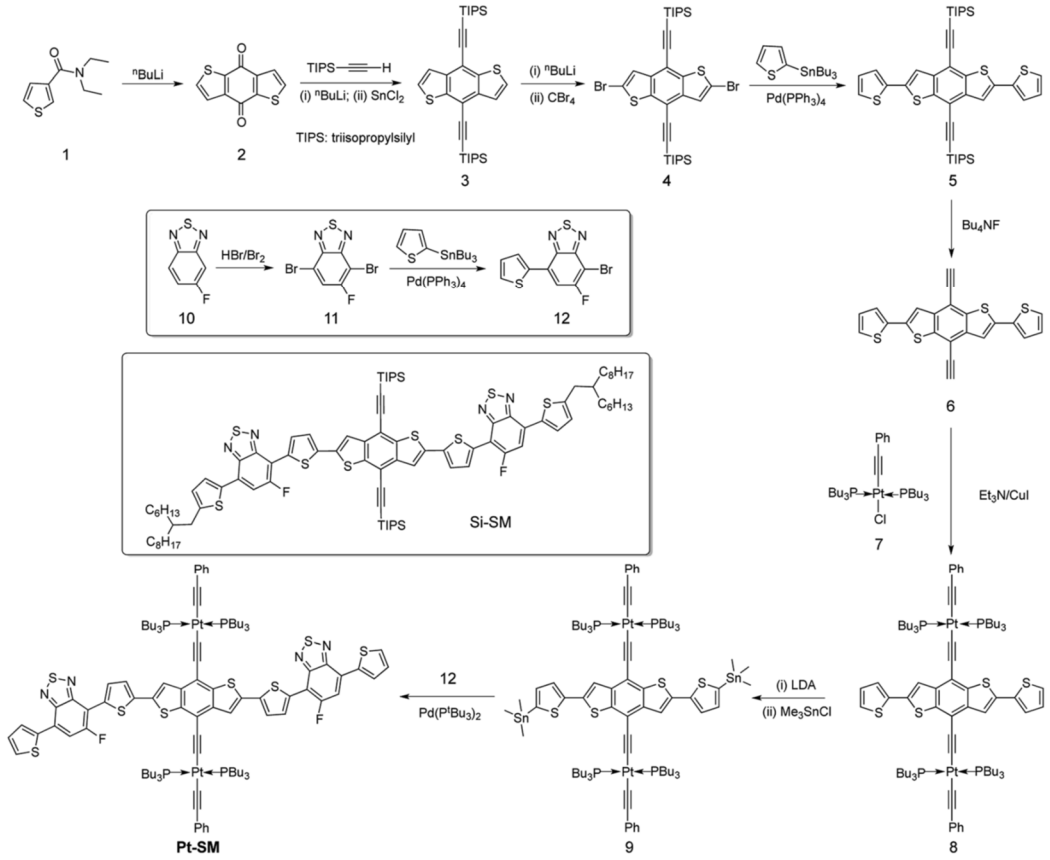

Scheme 3.2 Synthesis of Pt-SM and structure of Si-SM

3.2.2 Crystallinity of Pt-SM, Si-SM and Compound 8

Although we have not been able to obtain high quality single crystals for precise structure determination, certain crystallinity of Pt-SM can be observed in differential scanning calorimetry (DSC) and thin film X-ray diffraction (XRD) measurements. As shown in the DSC trace in Fig. 3.1 A, a clear, reproducible melting transition peak at 114 °C is seen. Fig. 3.1 B displays several sharp XRD signals from Pt-SM films drop-cast onto glass substrates. Although accurate assignments of these peaks are difficult, the signal at

2θ = 23.3° corresponds to a d-spacing of ca. 3.81 Å, which is characteristic of typical π–π stacking distances of aromatic molecules.[171] Such π–π stacking motifs are important for electronic coupling among adjacent chromophores and for efficient exciton/charge transport. Both the DSC and XRD measurements suggest that Pt-SM possesses certain crystallinity, which has rarely been observed in Pt-bisacetylide containing SMs and polymers.[172]

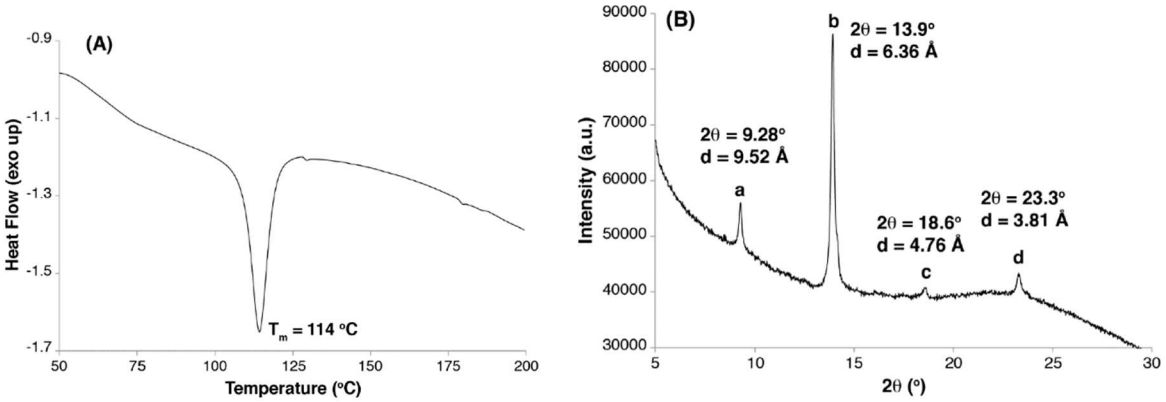

Figure 3.1 (A) Differential scanning calorimetry (DSC) trace (2nd heating, 10°C/min) of Pt-SM. (B) X-ray diffraction (XRD) patterns of Pt-SM films drop-cast onto glass substrates.

For a better comparison, we also studied the physical properties of the structurally similar Si-SM and compound 8 (Scheme 3.2) in detail. Fig. 3.2 shows the DSC traces (2nd heating) of these two compounds. Both Si-SM and 8 possess higher melting points at 243 °C and 204 °C, respectively, than that of Pt-SM. We have also not been able to obtain single crystals of Si-SM and its XRD pattern is shown in Fig. 3.3. Only one scattering signal at 2θ = 4.18°, corresponding to a d-spacing of 2.11 nm, can be observed, which indicates less crystalline order for Si-SM likely caused by the large branched alkyl side-chains. On the other hand, we did obtain single crystals of compound 8 and the crystal structures and molecular packing motifs are displayed in Fig. 3.4. Noticeably, although the

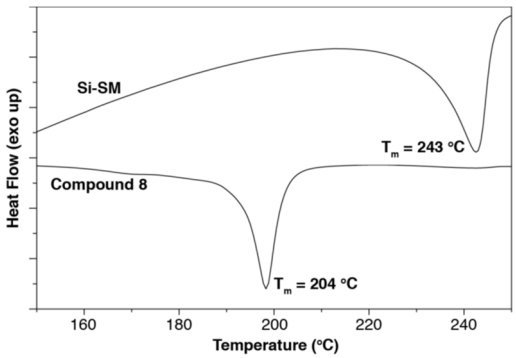

Figure 3.2 Differential scanning calorimetry (DSC) trace (2nd heating 10°C/min) of Si-SM and compound 8

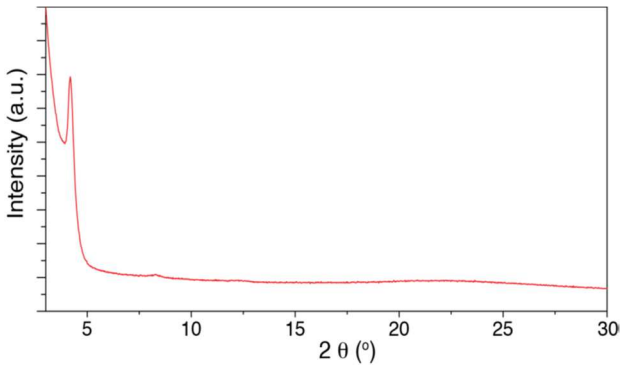

Figure 3.3 X-ray diffraction (XRD) patterns of Si-SM films drop-cast onto glass substrates.

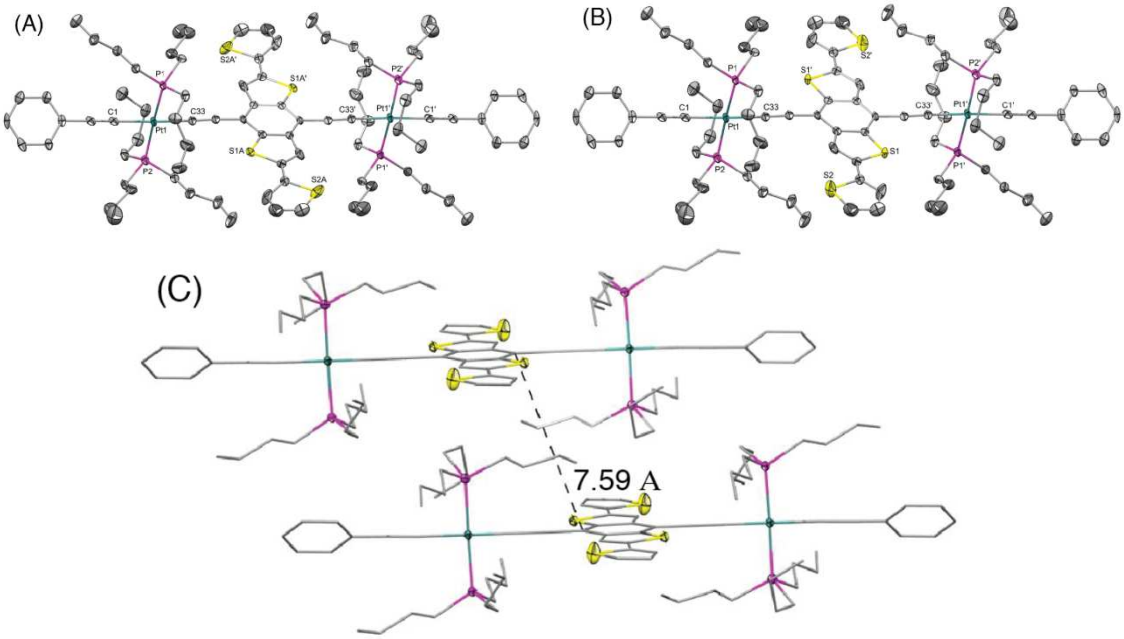

Figure 3.4 Crystal structures of compound 8. Thermal ellipsoids are drawn at 50% probability and hydrogen atoms have been omitted for clarity. (A) Major configuration (ca. 73%). (B) Minor configuration (ca. 27%). (C) Packing diagram of the major configuration with distance between C-C shown.

conjugated chromophores are nearly planar and parallelly aligned, they are slip-stacked from each other along the short axis with tri-n-butylphosphine groups situated in between.

Such packing geometry leads to an inter-chromophore distance of ca. 7.59 °A that is too large for efficient π–π interactions and charge transport (vide infra).

3.2.3 Density Functional Theory (DFT) Calculations of Pt-SM

The electronic properties of Pt-SM were first studied by using density functional theory (DFT) and the results are summarized in Fig. 3.5. All non-essential side chains are replaced with H atoms for computation efficiency and the ground state geometries are optimized using DFT, while the excited states are calculated with linear response time-dependent DFT (TD-DFT)[173,174] at the optimized ground state geometries only. All calculations are performed with the Gaussian 09 package (Rev. B.01) using the hybrid B3LYP functional. The 6-31G* basis set is used for all atoms except for Pt, which has the LANL2DZ basis set for its 5s, 5p, 5d, and 6s valence electrons while the core electrons are replaced by the corresponding pseudopotential.[175] A solvent reaction field simulated by the default polarizable continuum model (PCM) is also employed.[176] We then use the natural transition orbital (NTO) approach[176] to characterize the nature of the lowest singlet and triplet states. We first examined the bright singlet states in Pt-SM that are the S1 and S3 states having transition energies at 1.59 eV and 2.02 eV, respectively. From these NTOs that approximately represent the hole and electron in the transitions, both the S1 and S3 states have clear charge transfer characters mixed with metal-to-ligand-charge transfer (MLCT) transitions, as expected from the electron rich benzenedithiophene (BDT) core and electron poor fluorinated benzothiadiazole (F-BTD) arms, as well as the hole density delocalized throughout the Pt-bisacetylide moieties. We then examine the triplet states in Pt-SM. It should be noted that the NTOs for these triplet states are only the dominant representation

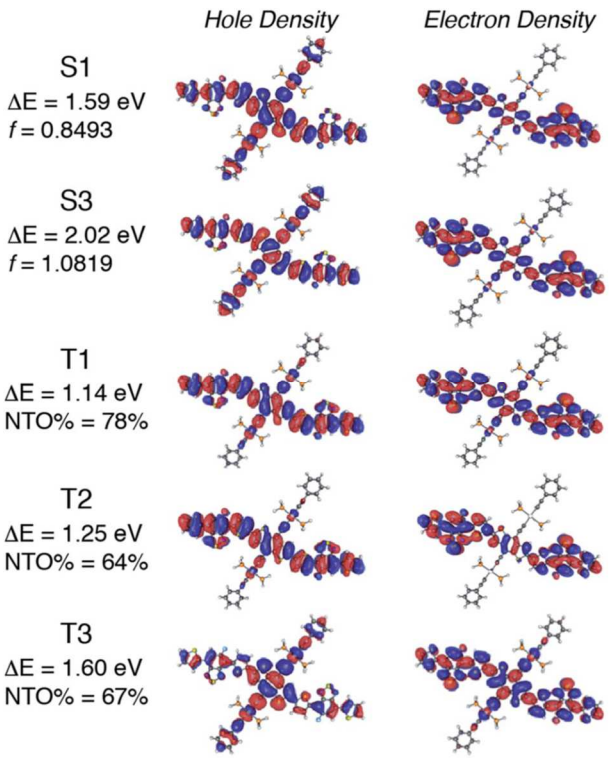

Figure 3.5 Low-lying bright singlet states and triplet states of Pt-SM calculated by density functional theory (DFT). DE: transition energy; f: oscillator strength; NTO: natural transition orbital.

(given in percentages), unlike the singlet transition in Fig. 3.5 where the NTOs represent 100% of the transitions. There are two triplet states having energies lower than S1, which are the T1 (1.14 eV) and T2 (1.25 eV) states. The T1 state is delocalized along the organic chromophore while the T2 state has obvious charge transfer character with spin density more localized on the F-BTD moieties. The third triplet state, T3, lies at 1.60 eV, i.e., less than 10 meV higher than that of S1. It is therefore, plausible that an efficient intersystem crossing occurs at S1 and T3.[177] T3 then fast decays into either T1 or T2, or both states, which then respectively decay to the ground state either single exponentially (from T1 or T2) or biexponentially (from both T1 and T2).

3.2.4 **UV-Vis Absorption and Emission Spectra**

The UV-vis absorption and emission spectra of Pt-SM in both dilute solutions and as thin films are shown in Fig. 3.6 Multiple absorption peaks at ca. 323, 364, 442, 487 and 560 nm are observed in dilute chlorobenzene solutions of Pt-SM. From the absorption onset at ca. 642 nm, the solution bandgap of Pt-SM is estimated to be ca. 1.93 eV. Upon casting

into thin films, the absorption profile of Pt-SM experiences significant red-shifts, leading to an onset of ca. 692 nm and an estimated solid-state bandgap of ca. 1.79 eV. Intriguingly, the films of Pt-SM display panchromatic behavior with strong absorption covering a large spectroscopic range from 300 nm to 700 nm, having multiple peaks at ca. 362, 432, 458, 523, 583 and 642 nm. It is not clear at this stage whether these peaks may be vibronic in nature or if they originate from different electronic transitions as suggested by DFT calculations. This question merits more detailed studies in the future.

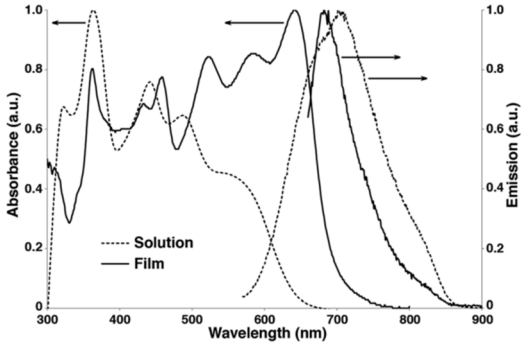

Figure 3.6 UV-Vis absorption and emission spectra of Pt-SM in chlorobenzene solutions (10^{-5} M, dashed lines) and as thin films (solid lines).

In order to qualitatively probe the origins of these electronic transitions, we also performed absorption and emission measurements of Si-SM and compound 8 under identical conditions. As shown in Fig. 3.7, Si-SM displays a dominant structureless peak at 517 nm in solutions, becoming structured and red-shifted to 606 nm in thin films, which is absent for compound 8. This low energy transition has been assigned to intramolecular charge-transfer (ICT) from the electron rich BDT centers to the electron poor F-BTD groups, as shown in recent examples with similar structures.[177–181] We thus assign the low energy absorption peaks observed for Pt-SM to similar ICT transitions, which is consistent with our DFT calculations. Noticeably, these ICT transitions of Pt-SM are at lower energies

respectively than those of Si-SM, suggesting electronic contribution to the ICT transitions from the Pt moieties through MLCT as suggested by the DFT calculations. Furthermore, spectral red-shift from solution to thin film is only observed for Pt-SM and Si-SM, but not for 8, indicating better molecular packing, and thus enhanced inter-molecular electronic interactions, for the first two compounds but otherwise for the latter. This observation is consistent with the XRD and crystal structure studies for Pt-SM and 8, respectively. Compared with 8, Pt-SM has identical bulky Pt-BDT center unit but more extended arms. The absorption profiles are thus consistent with our hypothesis that the "roller-wheel" structures can allow partial overlap and π–π interactions among adjacent molecules if the "roller-wheel" handles are long enough. Pt-SM shows very weak emissions peaked at ca. 700 nm in solutions (excited at 560 nm) and at ca. 680 nm as thin films (excited at 642 nm), respectively. The slight blue shift of the emission in thin films from that of the solutions is presumably due to H-type aggregation of the chromophores,[182,183] which is consistent with our conjecture on the solid-state structure of Pt-SM. The lifetime of these emissions was measured to be ca. 330 ps and did not change with or without the presence of oxygen. Also based on the relatively small Stokes shift, we assign the emissions of Pt-SM to fluorescence. The solution fluorescence quantum yield (QY) of Pt-SM is estimated to be ca. 0.77%, while the solution QY of Si-SM is calculated to be ca. 6.6%. This significant reduction in QY for Pt-SM is possibly caused by the attachment of Pt atoms, leading to increased intersystem crossing (ISC) rates. No phosphorescence could be observed for Pt-SM solutions or thin films even when cooled down to 10 K. Such lack of phosphorescence has been observed in previously reported Pt-containing low bandgap CPs and small molecules,[73,81,82,109,114]which is commonly ascribed to the energy gap law.[136] Noticeably,

compound 8 does display a phosphorescence peak at ca. 705 nm in deaerated solutions that disappears when open to air (Fig. 3.7).

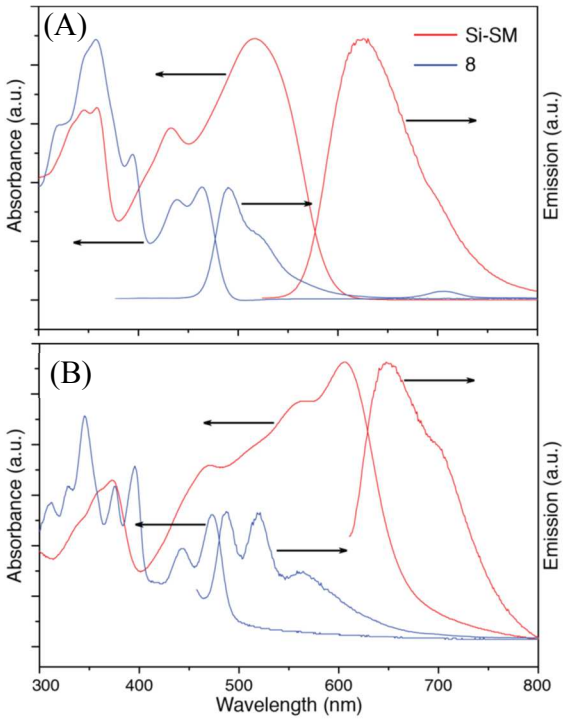

Figure 3.7 UV-vis absorption (left) and emission (right) spectra of compounds Si-SM (red) and Compound 8 (blue): (A) in degassed chlorobenzene solutions (10−5 M) and (B) as thin films spun cast onto glass substrates.

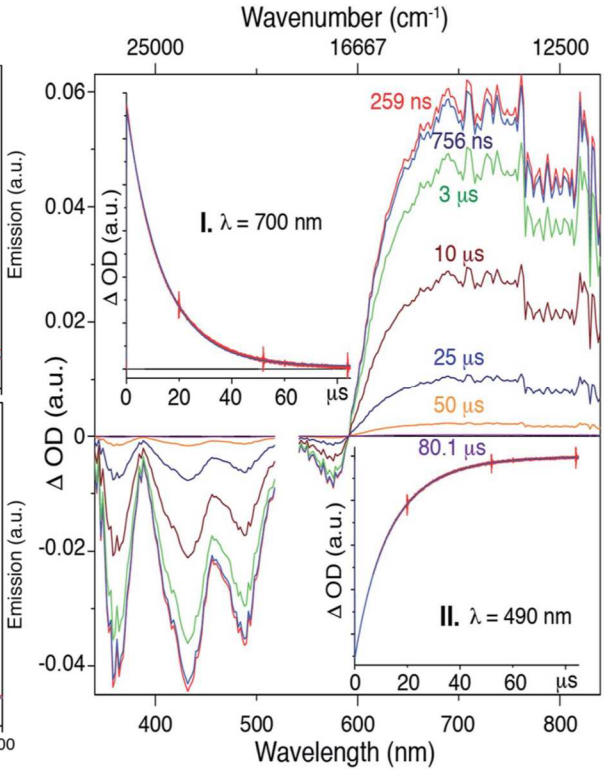

Figure 3.8 Transient absorption spectra of Pt-SM collected in chlorobenzene, excited at 532 nm. Insert: single wavelength kinetic traces (red) and fits (blue) at 700 nm (I) and 490 nm (II).

3.2.5 Time-resolved Transient Absorption Spectroscopy of Pt-SM

Although we are not able to directly observe phosphorescence from Pt-SM, the presence of ISC events and triplet states have been demonstrated by using transient absorption spectroscopy as shown in Fig. 3.8. The 750 ns transient absorption spectrum of Pt-SM features four negative or bleach peaks from 340 nm to 600 nm, and a broad excited state

absorption from 600 nm to 850 nm. The four bleach peaks are ascribed to loss of the ground state, as they are consistent with the absorption spectrum of Pt-SM (Fig. 3.6). We ascribe the excited state absorption feature to two different triplet transitions, as reported in similar systems,[80,106,111,184]and supported by our DFT calculations. Single wavelength kinetics collected at 700 nm and 490 nm, as respectively shown in inserts I and II of Fig. 3.8, retrieved time constants of 7.5 ± 0.4 μs and 16.3 ± 0.4 μs. These are in good agreement with lifetimes of 7.6 ± 0.35 μs and 16.4 ± 0.27 μs, obtained from global fitting analysis. We ascribe the 7.5 μs time constant observed in the transient kinetics to a triplet charge separated state from the BDT core to the F-BTD arms, i.e., the T2 state from DFT calculations. The 16.5 μs transition is thus ascribed to the T1 triplet state that is more delocalized. We make these assignments based upon independent transient absorption spectroscopic measurements of the compound 8 and Si-SM. The lifetime of the 700 nm transient absorption of Si-SM is fit to a single exponential of 1.6 μs and that of 8 (700 nm) is fit to a lifetime of 14.7 μs, respectively. This observation is consistent with DFT calculations, which find two triplet states of different origins in close energy (ca. 0.1 eV) to each other.

3.2.6 Cyclic Voltammetry Measurements

The HOMO and LUMO levels of Pt-SM were estimated using cyclic voltammetry (CV) as shown in Fig. 3.9. One pseudo-reversible reduction and two oxidation peaks are observed, from the onsets of which, the HOMO and LUMO levels are estimated to be ca. -5.0 eV and -3.2 eV, respectively, leading to an electrochemical bandgap of ca. 1.8 eV that agrees well with the optical measurements.

3.2.7 Hole Mobility Measurements of Pt-SM, Si-SM and Compound 8

One key parameter of organic materials for electronic devices is the charge mobility. We have measured hole mobilities of Pt-SM, Si-SM and compound 8 using space charge

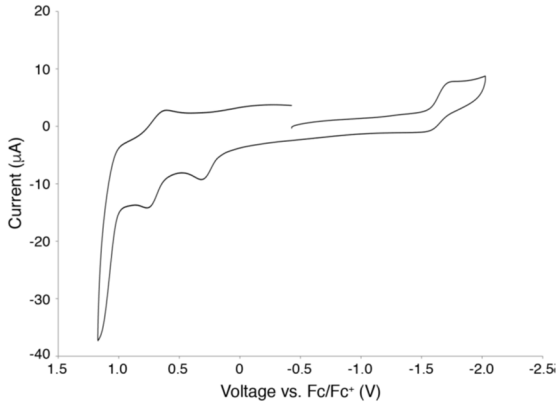

Figure 3.9 Cyclic voltammogram (CV) of Pt-SM in CH_2Cl_2 (1 mM) using Bu_4NPF_6 as supporting electrolyte (0.1 M). The potential is calibrated externally against ferrocene (Fc) redox couple (4.80 V below vacuum).

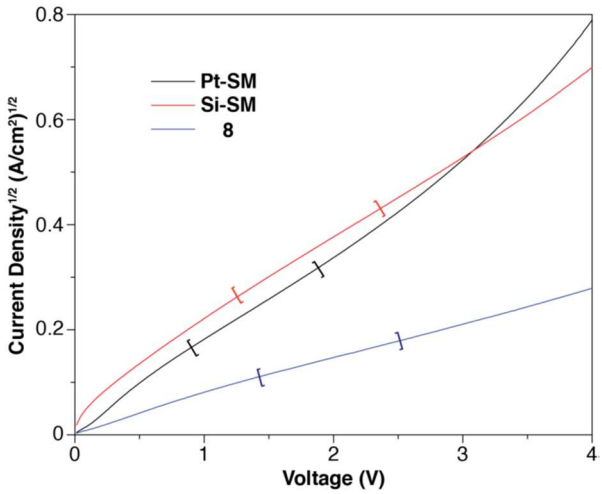

Figure 3.10 Space charge limited current (SCLC) profiles of Pt-SM (black), Si-SM (red) and 8 (blue) obtained from hole selective devices having geometries: ITO/MoO_3/organic/MoO_3/Al. The segments within the square brackets are the linear regions used for respective hole mobility calculations.

limited current (SCLC) method.[185] Hole selective device geometries (ITO/MoO_3/organic/MoO_3/Al) are employed and the current density–voltage (I–V) curves are shown in Fig. 3.10. From the linear region of each I–V curve, the hole mobilities of Pt-SM, Si-SM and 8 are estimated to be 1.5×10^{-5} cm^2 V^{-1} s^{-1}, 1.6×10^{-5} cm^2 V^{-1} s^{-1} and 1.6×10^{-6} cm^2 V^{-1} s^{-1}, respectively. Although single crystalline in the solid state, 8 displays one order of magnitude lower hole mobility. This is expected from the crystal structure in which there is no efficient π–π overlap among adjacent chromophores for charge transport and agrees well with the nearly identical solution and film absorption profiles. On the other hand, Pt-SM and Si-SM show similarly enhanced charge mobilities, indicating better solid state packing structures and more efficient π–π stacking among adjacent conjugated chromophores.

3.3 Solar Cell Performance

OSC devices were fabricated using Pt-SM, Si-SM and compound 8 in device geometries: ITO glass/MoO_3 (10 nm)/organic blend layer/Al (100 nm). The devices were first optimized using blends of phenyl-C_{61}-butyric acid methyl ester ($PC_{61}BM$) by varying the donor/acceptor weight ratios, solvent choices, solution concentrations, spin-coating conditions and thermal/solvent annealing conditions. Table 3.1 summarizes representative device parameters of Pt-SM from various optimization conditions and Table 3.2 gives the optimized device performances of Si-SM and 8. The best devices were found to use a Pt-SM/$PC_{61}BM$ weight ratio of 10/8, the film thickness of ca. 80 nm and solvent annealing in $CHCl_3$ saturated environment for 2 min. We then substituted PC61BM with phenyl-C_{71}-butyric acid methyl ester ($PC_{71}BM$) in the Pt-SM devices by employing the optimized conditions. Table 3.1 summarizes the performance parameters of the devices and Fig.

3.11A displays the representative I–V curves, and absorption and external quantum efficiency (EQE) profiles, as well as the transmission electron microscopy (TEM) image. (Fig. 3.11B)

Table 3.1 Summary of OSC device performances employing Pt-SM with $PC_{61}BM$ or $PC_{71}BM$ under various fabrication conditions. Averages are calculated from at least five devices and the best values are given in parentheses.

rpm[a]	Conc.[b] mg/mL	wt./wt.[c]	Solv.[d]	Anneal.[e]	V_{oc} (V)	J_{sc} (mA/cm^2)	FF (%)	PCE (%)
1000	10	1:1	CF	AC	0.60±0.05 (0.64)	0.84±0.47 (1.55)	44.6±1.39 (46.4)	0.23±0.13 (0.43)
1000	5	1:1	CF	AC	0.84±0.02 (0.85)	3.94±0.45 (4.46)	33.3±1.56 (34.3)	1.10±0.16 (1.30)
1200	5	1:1	CF	AC	0.87±0.004 (0.87)	3.62±0.48 (4.39)	44.7±0.96 (46.2)	1.40±0.17 (1.59)
1600	5	1:1	CF	AC	0.73±0.01 (0.74)	2.68±0.37 (3.00)	53.8±2.25 (56.0)	1.09±0.14 (1.18)
1200	5	1:0.8	CF	AC	0.91±0.005 (0.92)	6.45±0.68 (7.40)	41.4±1.31 (43.2)	2.43±0.30 (2.91)
1200	5	1:0.8	CF	TA1	0.87±0.005 (0.88)	8.33±0.93 (8.90)	48.0±1.11 (49.8)	3.50±0.42 (3.76)
1200	5	1:0.8	CF	TA2	0.87±0.005 (0.88)	8.33±1.50 (9.76)	52.4±4.66 (56.7)	3.80±0.74 (4.61)
1200	5	1:0.8	CF	SA1	0.87±0.005 (0.87)	8.66±1.17 (9.97)	57.8±2.29 (60.4)	4.32±0.41 (4.80)
1200	5	1:0.8	CF	SA2	0.86±0.005 (0.86)	10.66±1.51 (11.81)	56.3±0.64 (56.2)	5.14±0.70 (5.64)
1200	5	1:0.8	CF	ST	0.87±0.005 (0.87)	9.62±1.32 (10.70)	50.2±1.22 (51.8)	4.20±0.48 (4.62)
1200	5	1:0.8[c´]	CF	SA2	0.80±0.03 (0.85)	11.9±1.50 (14.4)	57.0±0.4.5 (63.0)	5.60±0.29 (5.90)

[a] Spin coating speed; all for 30s. [b] Concentration of Pt-SM. [c] Pt-SM/$PC_{61}BM$ weight ratio. [c´] Pt-SM/$PC_{71}BM$ weight ratio. [d] Solvent; CF: chloroform. e Annealing conditions; AC: as cast; TA1: thermal annealing at 100 °C for 10 min after deposition of Al; TA2: thermal annealing at 120 °C for 10 min after deposition of Al; SA1: solvent (CF) annealing for 1 min before deposition of Al; SA2: solvent (CF) annealing for 2 min before deposition of Al; ST: solvent (CF) annealing for 2 min before deposition of Al and thermal annealing at 100 °C for 10 min after deposition of Al.

The optimized devices display an average PCE of ca. 5.6% and a highest value of ca. 5.9%, which are significantly higher than values reported previously for OSCs applying Pt-containing polymers. The J_{SC} values of Pt-SM devices are comparable to those reported Table 3.2 Optimized performance parameters of Si-SM/P_{61}BM and 8/PC_{61}BM devices. Averages are calculated from at least five devices and the best values are given in parentheses. Annealing condition for both is thermal at 150 °C for 10 min after deposition of Al

Table 3.2 Summary of OSC device performances employing Si-SM and Compound 8 with PC_{61}BM under optimized fabrication conditions. Averages are calculated from at least five devices and the best values are given in parentheses.

	rpm[a]	Conc.[b] mg/mL	wt./wt.[c]	Solv.[d]	V_{oc} (V)	J_{sc} (mA/cm2)	FF (%)	PCE (%)
Si-SM	800	5	1:0.8	CF	0.95±0.008 (0.96)	6.37±1.16 (7.35)	52.8±3.44 (56.2)	3.20±0.44 (3.44)
8	800	10	1:1	CF	0.35±0.013 (0.36)	0.059±0.006 (0.058)	49.5±5.03 (55.1)	0.01 (0.01)

[a] Spin coating speed; all for 30s. [b] Concentration of Si-SM or 8. [c] Si-SM or 8/PC_{61}BM weight ratio. [d] Solvent; CF: chloroform.

previously for best-performing Pt-containing polymers. The EQE responses closely match the thin film absorption profiles as shown in Fig. 3.11A (insert), displaying panchromatic responses from 350 nm to 650 nm. A relatively large V_{OC} value of ca. 0.82 V was obtained, indicating small energy loss during the charge separation and collection processes, considering that the energy gap between HOMO of Pt-SM and LUMO of PC_{71}BM is ca. 1 eV.64 These V_{OC} values are also comparable with those from the best performing devices employing Pt-containing polymers. The major improvement comes from the fill factors (FFs). Pt-SM devices constantly display FFs close to 60% while previous polymer

examples rarely gave FFs above 40%. Furthermore, in previous examples, large excesses of fullerenes are required to reach the maximum PCEs due to the amorphous nature of the polymers. In the case of Pt SM, only 44 wt% of fullerenes are sufficient to achieve the optimum performance, likely due to the more crystalline nature of the small molecule leading to better thin film morphologies. Indeed, TEM image of the device active layer (Fig. 3.11B) shows the absence of large aggregates and an interpenetrated network with favorable domain sizes of ca. 5–10 nm.

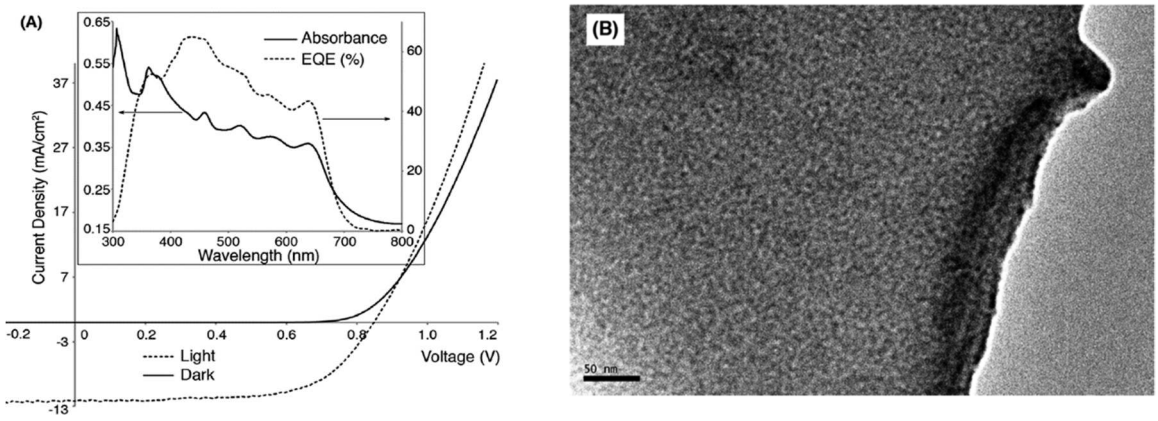

Figure 3.11 (A) Current density–voltage (I–V) curves of a representative OSC device in dark (solid line) and under simulated AM1.5 solar irradiations (dashed line). Insert: absorption (solid line) and external quantum efficiency (EQE, dashed line) profiles of the same device. (B) Transmission electron microscopy (TEM) image of the active layer of the device (scale bar is 50 nm).

3.3.1 Stability of Pt-SM Organic Solar Cells

We then studied stability of the optimized Pt-SM/$PC_{71}BM$ devices through aging tests at room temperature and at 80 °C, and the results are summarized in Fig. 3.12. After two weeks, the devices stored at room temperature show only slight decrease of performance to ca. 85% of the original PCEs; while devices kept at 80 °C display a bigger PCE drop to

ca. 65%. From optical micrographs of these devices shown in Fig. 3.13, both devices as optimized and aged at room temperature show smooth films free of any visible phase segregation and large aggregates. Phase separations on the order of a few mm can be observed in films aged at 80 °C after 14 days, which is still free of any large crystallites. Such coarsening of active layer morphologies likely explains the relatively higher decay rate of device performances.

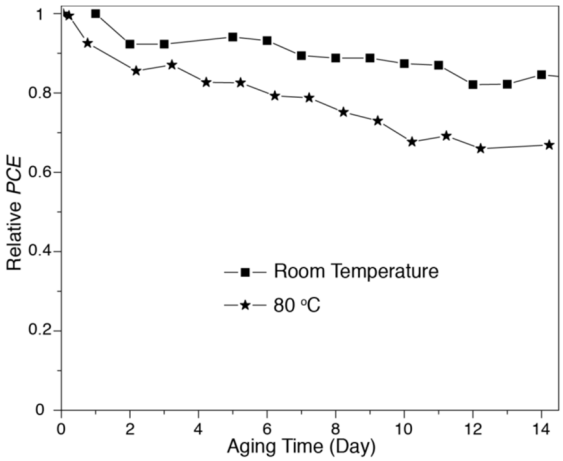

Figure 3.12 Aging tests of optimized Pt-SM/$PC_{71}BM$ devices at room temperature and at 80 °C.

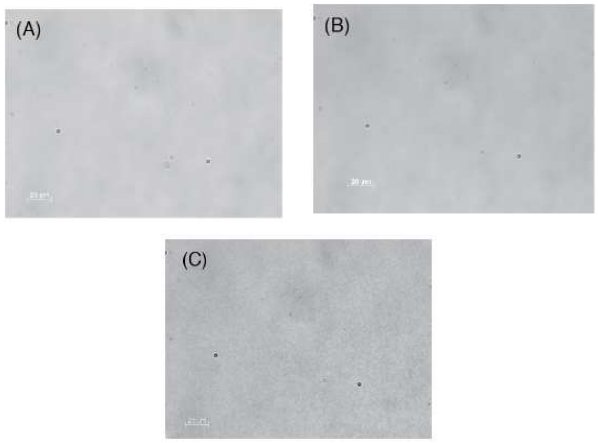

Figure 3.13 Optical micrographs of Pt-SM/$PC_{71}BM$ devices (A) as optimized; (B) aged at room temperature for 14 days; and (C) aged at 80 °C for 14 days.

3.4 Conclusion

In summary, we have designed and synthesized a Pt-bisacetylide containing SM, featuring "roller-wheel" geometry. This new structural design allows partial overlap among the main rigid chromophores, leading to enhanced crystallinity and π–π interactions. OSCs employing Pt-SM displayed higher PCEs, mostly resulted from improved FFs, than those applying Pt-containing polymers reported previously. This molecular design strategy

can be extended to other low bandgap linear organic chromophores as well as conjugated polymers, which will potentially lead to promising materials for OSCs and other organic electronics.

3.5 Experimental

3.5.1 Materials and General Methods

All reagents and solvents were used as received from Sigma-Aldrich or VWR unless otherwise noted. Anhydrous THF was distilled over Na/benzophenone prior to use. Anhydrous chloroform and triethylamine (TEA) were obtained by distillation over CaH_2 and degassed through several freeze-pump-thaw cycles. Phenyl-C_{61}-butyric acid methyl ester ($PC_{61}BM$) and phenyl-C_{71}-butyric acid methyl ester ($PC_{71}BM$) were purchased from American Dye Source. N,N-Diethyl-3-thiophenecarboxamide (1),[186] benzo[1,2-b:4,5-b']dithiophene-4,8-dione (2),[187] benzo[1,2-b:4,5-b']dithiophene-4,8-bis[2-[triisopropylsilyl]ethynyl] (3),[188] 2,6-dibromo-4,8-bis[2- [triisopropylsilyl]ethynyl] (4),[189] benzo[1,2-b:4,5 b']dithiophene-2,6-di-2-thienyl-4,8-bis[2-[triisopropylsilyl]ethynyl] (5),[190] benzo[1,2-b:4,5-b']dithiophene-4,8-diethynyl-2,6-di-2-thienyl (6),[191] Trans-Chloro(phenylethynyl)bis(ributylphosphine)platinum(7),[172] 5-fluoro-2,1,3-benzothiadiazole (10),[192] 4,7-dibromo-5-fluoro-2,1,3 benzothiadiazole (11),[193] were synthesized according to literature procedures. 300.13 MHz ^{1}H, 75.48 MHz ^{13}C, 121.5 MHz ^{31}P and 282.4 MHz ^{19}F NMR spectra were recorded on a Bruker Avance III Solution 300 spectrometer. All solution ^{1}H spectra were referenced internally to tetramethylsilane and ^{13}C spectra were referenced internally to chloroform. ^{31}P and ^{19}F were referenced externally by using standards H_3PO_4 (δ = 0 ppm) and C_6F_6 (δ = -164.9 ppm). Ultraviolet visible (UV-Vis) absorption spectra were recorded on a Shimadzu UV-2401 PC

spectrometer over a wavelength range of 300−900 nm. Fluorescence emission spectra were obtained using a Varian Cary Eclipse Fluorimeter. Fluorescence quantum yield (QY) is estimated using quinine sulfate as a standard (54% in 0.1 M H_2SO_4).[194] Differential scanning calorimetry (DSC) measurements were performed on a Mettler Toledo DSC STARe system with ca. 8 mg sample and at a scan rate of 10 °C/min. The results reported are from the second heating cycle. Cyclic voltammetry (CV) was performed at 25 °C on a CH Instrument CH1604xD electrochemical analyzer using a glassy carbon working electrode, a platinum wire counter electrode and Ag/AgCl reference electrode, calibrated using a ferrocene redox couple (4.8 eV below vacuum). X-ray diffraction (XRD) data was collected using a Rigaku SmartLab diffractometer in Bragg-Brentano mode employing Cu K-α radiation and a D/tex 1-dimensional detector. A nickel filter was used to remove the Cu K-β radiation component. Data was collected over a 2θ range from 5° to 40° using 0.02° step size at a scan rate of 1°/min. Transmission electron microscopy (TEM) images were taken on a JEOL 2010 EX HREM with an Oxford-Link EDS Gatan Digital Micrograph equipped with a slow scan CCD camera. Samples were prepared by soaking solar cell devices employing PEDOT: PSS as anode interfacial layers in water and fishing our floating active layers with carbon coated TEM grids. High resolution mass spectrometry (HRMS) was analyzed by Mass Spectrometry using Electrospray Ionization (ESI) in positive mode on a Waters LCT Premier Time of Flight (TOF) mass spectrometer. Thin film thickness was measured using the KLA-Tencor D-100 Profilometer. Transient absorption lifetimes were collected on an Edinburgh Instruments LP920 Laser Flash Photolysis Spectrometer. The excitation source consists of a Continuum Surelight II Model SLI-10 (Nd:YAG, 10 Hz) with SHG and THG options to generate 532 nm and 355 nm

wavelengths. A Surelight SSP (dichroic to separate the 532 and 355) is positioned in between the laser to select the desired pump wavelength. A 450W ozone free Xenon arc lamp generates a microsecond white light supercontinuum probe beam, which is arranged in a 90° cross-beam geometry excitation beam at the sample. The probe beam passes through a monochromator and is captured by a Hamamatsu R928 PMT. Individual single wavelength kinetics are collected at a 2 nm step size to construct transient absorption spectra at specific times. Transient data are fit by re-convolution in SurfaceXplorer (v. 4) using a second order multiexponential decay with a fixed Instrument Response Function of 40 ns.

3.5.2 Solar Cell Fabrication and Testing

Pt-SM/$PC_{71}BM$ blend solutions were prepared by dissolving Pt-SM and $PC_{71}BM$ at predetermined weight ratios in chloroform at a Pt-SM concentration of 0.5 wt% and stirred at room temperature for 3-4 hours in a nitrogen glovebox (Innovative Technology, model PL-He-2GB, O_2 < 0.5 ppm, H_2O < 0.5 ppm). Solar cell devices were fabricated according to the following procedure: ITO-coated glass substrates (China Shenzhen Southern Glass Display Ltd.; 8 Ω/□) were cleaned by ultrasonication sequentially in detergent water, DI water, acetone and isopropyl alcohol, each for 15 min. These ITO-coated glasses were further treated by UV-ozone (PSD Series, Novascan) for 60 min before being transferred to a nitrogen glovebox (Innovative Technology, model PL-He-2GB, O_2 < 0.1 ppm, H_2O < 0.1 ppm) for MoO_3 deposition. MoO_3 (10 nm) was deposited using an Angstrom Engineering Amod deposition system at a base vacuum level of < 4×10^{-7} Torr. The Pt-SM/fullerene blend solution was first filtered through a 0.45 μm PTFE filter and spin-coated on top of the MoO_3 layer at 1200 rpm for 30 s. Al (100 nm) was thermally

evaporated through patterned shadow masks as anodes, the sizes of which define the active areas of the solar cells to be 7.1 mm^2. Current-voltage (I-V) characteristics were measured using a Keithley 2400 source-measuring unit under simulated AM 1.5G irradiation (100 mW/cm^2) generated by a Xe acr-lamp based Newport 67005 150 W solar simulator equipped with an AM 1.5G filter. The light intensity was calibrated using a Newport thermopile detector (model 818P-010-12) equipped with a Newport 1916-C optical Power Meter. External quantum efficiency (EQE) values were measured by using a commercial solar cell quantum efficiency measurement system (Model QEXL, PV Measurements, Inc., Boulder, CO). The EQE system was calibrated with a Si photodiode certified by the National Renewable Energy Laboratory (NREL).

3.5.3 Experimental Details

Compound 8. Into a 100 mL round bottom flask equipped with a magnetic stir bar, compound 6 (185 mg, 0.46 mmol), compound 7 (812 mg, 1.1 mmol) and CuI (17.5 mg, 0.092 mmol) were dissolved in a mixture of 40 mL anhydrous chloroform and 2 mL triethylamine under argon. The flask was then sealed and the reaction mixture was stirred for 12 h before removal of the solvents under reduced pressure. The product 8 was isolated by flash column chromatography using hexanes/CH_2Cl_2 (8/1) and further purified by recrystallization from $CHCl_3$/CH_3OH mixture as a yellow solid (700 mg, 85% yield). ^{1}H NMR (300.13 MHz, $CDCl_3$): δ (ppm) = 7.66 (s, 2H), 7.32 (m, 6H), 7.21 (m, 6H), 7.12(m, 2H), 7.04 (dd, 2H, ^3JHH = 3.6 Hz), 2.21 (m, 24H), 1.66 (m, 24H), 1.44 (m, 24H), 0.91 (t, 36H, ^3JHH = 7.2 Hz). ^{31}P NMR (121.5 MHz, $CDCl_3$): δ (ppm) = 4.03 ($J_{Pt\text{-}P}$ = 2,350 Hz). ^{13}C NMR (75.48 MHz, $CDCl_3$): δ (ppm) = 138.7, 138.2, 136.0, 130.9, 129.1, 127.8, 127.7, 124.8, 124.1, 120.4, 120.1, 114.2, 109.6, 107.8, 105.3, 26.5, 24.3, 23.9, 13.9. Orange rod

like single crystals of $C_{86}H_{126}P_4Pt_2S_4$, 8, approximate dimensions 0.130 mm x 0.144 mm x 0.192 mm, was coated with Paratone oil and mounted on a MiTeGen MicroLoop that had been previously attached to a metallic pin using epoxy for the X-ray crystallographic analysis. The X-ray intensity data were measured on a Bruker Kappa APEX II CCD system equipped with a graphite monochromator and a Mo Kα fine-focus tube (λ = 0.71073 Å). Crystal data. $C_{86}H_{126}P_4Pt_2S_4$, M = 1802.16, monoclinic, a = 12.7253(4), b = 8.8911(3), c = 37.7183(12) Å, β = 94.230(2)°, U = 4255.9(2) Å^3, T = 99(2) K, space group *P 21/n*, Z = 2, 42733 reflections measured, 10187 unique (*R*int = 0.0871), which were used in all calculations. The final w*R(F2)* was 0.0986 (all data).

Compound 9. Into a solution of compound **8** (480 mg, 0.27 mmol) in dry THF (20 mL) being stirred under nitrogen at −78 °C, was added slowly 0.4 mL lithium diisopropylamide (2.0 M in THF/n-heptane/ethylbenzene, 0.8 mmol). After stirring for 60 min at -78 °C, 186 mg trimethyltin chloride (0.93 mmol) dissolved in 5 mL dry THF was added dropwise and the reaction mixture was slowly warmed up to room temperature and further stirred for 12 h. The reaction was quenched by the addition of water and extracted with chloroform (×3). The organic layer was washed with water, brine and dried over anhydrous Na_2SO_4. After the solvent was removed under vacuum, the crude product was purified by recrystallization ($CHCl_3$/MeOH) as a yellow solid (500 mg, 88% yield). ^{1}H NMR (300.13 MHz, $CDCl_3$): δ (ppm) = 7.66 (s, 2H), 7.32 (m, 6H), 7.21 (m, 4H), 7.11(m, 4H), 2.20 (m, 24H), 1.67 (m, 24H), 1.45 (m, 24H), 0.91 (t, 36H, ^3JHH = 7.2 Hz), 0.39 (s, 18H). ^{31}P NMR (121.5 MHz, $CDCl_3$): δ (ppm) = 4.01 ($J_{Pt\text{-}P}$ = 2,352 Hz) ^{13}C NMR (75.48 MHz, $CDCl_3$): δ (ppm) = 144.3, 138.7, 138.2, 137.9, 135.9, 135.8, 130.8, 129.1, 127.8, 125.3, 124.8, 120.0, 114.0, 109.5, 107.9, 105.3, 26.5, 24.4, 23.9, 13.9, -8.30.

Compound 12. Into a 125 mL pressure vessel, were added compound 11 (1.0 g, 3.2 mmol), tributyl(thiophen-2-yl) stannane (1.2 g, 3.2 mmol), tetrakis(triphenylphospine)palladium (111 mg,0.1 mmol) and 30 mL dry toluene, and the vessel was sealed and stirred at 120 °C for 24 hours. Toluene was then removed under reduced pressure and the residue was dissolved in chloroform. The solution was passed through a short silica gel column and volatile solvents were removed under reduced pressure. The crude product was purified by flash column chromatography using hexanes/CH_2Cl_2 (10/1) and the product 12 was further purified by recrystallization ($CHCl_3$/MeOH) as an orange red solid (706 mg, 70% yield). ^{1}H NMR (300.13 MHz, $CDCl_3$): δ(ppm) = 8.13 (d, 1H, ^3JHH = 3.6 Hz), 7.74 (d, 1H, ^3JHH = 10.2 Hz), 7.54 (d, 1H, ^3JHH = 5.1 Hz), 7.22 (dd, 1H, ^3JHH = 3.9 Hz). ^{19}F NMR (282.4 MHz, $CDCl_3$): δ (ppm) = −101.8. ^{13}C NMR (75.48 MHz, $CDCl_3$): δ (ppm) = 162.2, 158.9, 154.0, 148.8, 137.1, 128.8, 128.3, 127.4, 116.3,96.2.

Pt-SM. Compound 9 (200 mg, 0.094 mmol) and compound 12 (177 mg, 0.564 mmol) were dissolved in 20 mL anhydrous toluene in a 100 mL flask under argon, and $Pd(^tBu_3P)_2$ (9.6 mg,0.019 mmol) was added as a solid. The flask was sealed and the reaction mixture was stirred for six hours at room temperature. Toluene was then removed under reduced pressure and the resulting crude product was purified by column chromatograph using hexanes/CH_2Cl_2 (4/1). Pt-SM was further purified by recrystallization ($CHCl_3$/MeOH) as a dark red solid (35 mg, 16.4% yield). ^{1}H NMR (300.13 MHz, $CDCl_3$): δ (ppm) = 8.31 (d, 2H, ^3JHH = 3.9 Hz), 8.17 (dd, 2H, ^3JHH = 3.6 Hz), 7.83 (s, 2H), 7.80 (d, 2H, ^3JHH = 12.9 Hz), 7.53 (dd, 2H, ^3JHH = 4.8 Hz), 7.36 (m, 6H),7.15 (m, 8H), 2.24 (m, 24H), 1.71 (m, 24H), 1.49 (m, 24H), 0.94 (t, 36H, ^3JHH = 7.2 Hz). ^{31}P NMR (121.5MHz, $CDCl_3$): δ (ppm)

= 4.05 ($J_{Pt\text{-}P}$ = 2,345 Hz). ^{19}F NMR (282.4 MHz, $CDCl_3$): δ(ppm) = -106.2. ^{13}C NMR (75.48 MHz, CDCl3): δ (ppm) = 160.7, 157.3, 153.4, 149.9, 141.1,139.2, 138.5, 138.0, 135.9, 132.1, 131.2, 131.1, 130.9, 128.4, 127.9, 124.8, 124.5, 120.7, 117.4,114.5, 111.2, 109.6, 107.8,105.4, 26.5, 24.4, 24.0, 13.9. HRMS: (ESI): $C_{106}H_{132}F_2N_4P_4Pt_2S_8$, calcd, 2269.6510 for [$M^+$]; found, 2269.6453 for [M^+].

Chapter 4

A "Roller-Wheel" Pt-containing Small Molecule with Proven Slip-Stack Packing and Its Application in Organic Solar Cells

4.1 Introduction

According to the results from chapter 3, the Pt-containing compounds with a roller-wheel structure have been demonstrated to be an original and effective methodology to increase the device performance of organic solar cells.[63] In addition, the novel design has shown the enhanced crystallinity of the Pt-containing conjugated system, leading to an ideal morphology of the active layer, which have been well proved by DSC, XRD and TEM from previous chapter.

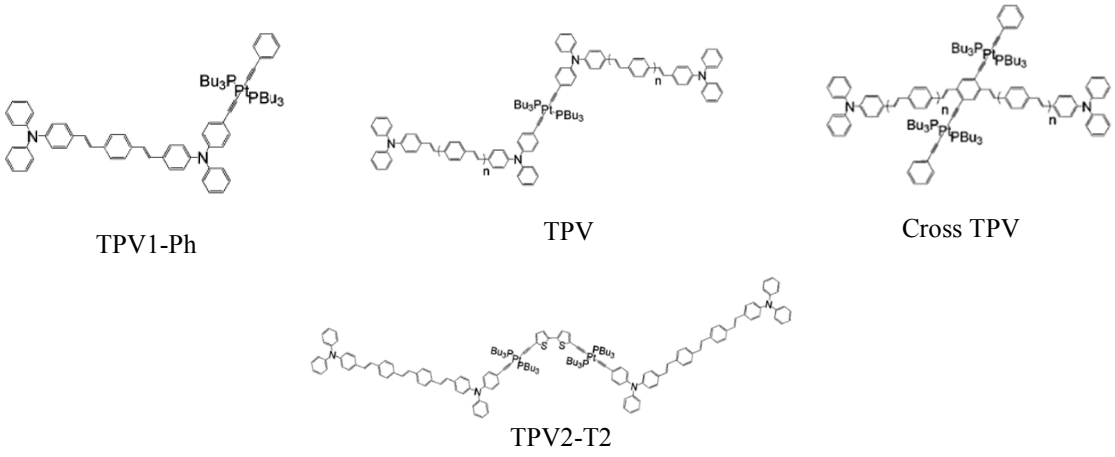

Scheme 4.1 Structures of p-(phenylene vinylene) platinum(II) acetylide chromophores.

However, we don't have direct evidence to support our assumption of slip-stack packing of Pt-SM since the single crystal of Pt-SM was not attained. Actually, there is only one paper reported so far, which provided the single crystal structure of Pt-containing compounds with a long conjugated system.[172] In this work, Dunibina et al. synthesized

various Pt-containing compounds with oligomer PPV as the arms (Scheme 4.1) and the work was mainly focused on the photophysical studies.

Unfortunately, with this all donor design, the bandgap of the final compounds will be relatively high (~2.5 eV) and more importantly, the S1-T1 gap will be fairly large since there is a considerable overlap between the HOMO and LUMO in this type of compounds therefore it is impossible for PCBM to capture the triplet exciton.[195] As a matter of fact, the design in this paper is not suitable for organic solar cells.

In order to solve this problem, we proposed a new synthetic route to synthesize a new donor-acceptor Pt-containing small molecule with longer conjugated arms and higher crystallinity. Above all, with the increased crystallinity, we successfully obtained the single crystal of finally product and demonstrated the existence of slip-stack packing in the system.

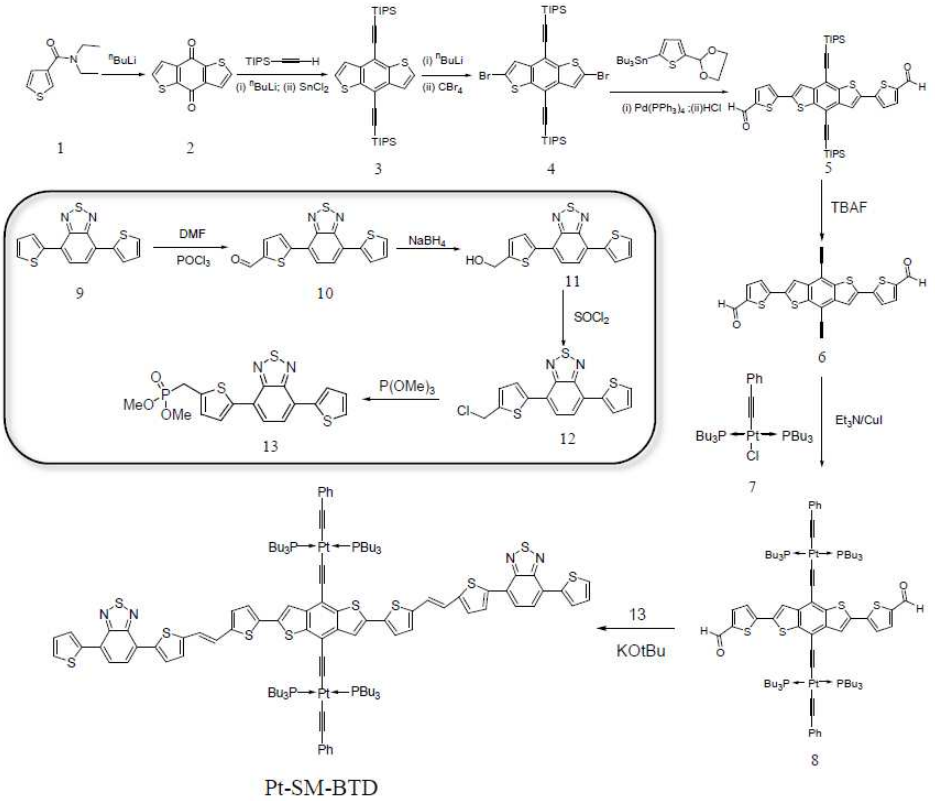

Scheme 4.2 Synthesis of Pt-SM-BTD

4.2 Results and Discussion

4.2.1 Synthesis of Pt-SM-BTD

Synthetic procedures toward the target compound Pt-SM-BTD are outlined in Scheme 4.2 and the synthetic details are included in the Section 4.5.3. The core of Pt-SM-BTD is similar to that of Pt-SM except the aldehyde functional group will be used to form the final product through Wittig-Horner reaction[196] instead of Stille coupling. As a result, the final Pt-SM-BTD will have one more thiophene and double bond on each side of the arm which will further increase the crystallinity and the conjugated length of the final compound. On the other hand, the four bulky tri(n-butyl) phosphine ligands make Pt-SM-BTD readily soluble in common organic solvents such as $CHCl_3$, chlorobenzene, toluene and THF, etc., without the need for additional alkyl side-chains. Pt-SM-BTD is fully characterized by ^{1}H, ^{13}C, ^{19}F and ^{31}P NMR spectroscopy, as well as high resolution mass spectrometry (HR-MS).

4.2.2 UV-Vis Adsorption and Emission Spectra

The UV-Vis absorption and emission spectra of Pt-SM-BTD in both dilute solutions and as thin films are shown in Fig. 4.1. Multiple absorption peaks at 543, 507, 378, and 318 nm are observed in the dilute chlorobenzene solution of Pt-SM-BTD. From the onset of absorption at ca. 635 nm, the solution bandgap of Pt-SM-BTD is calculated to be 1.95 eV. On the other hand, the films of Pt-SM-BTD display panchromatic behavior with strong absorption covering a large spectroscopic range from 300 nm to 700 nm with a significant red-shifts compared to the absorption in the solution, which means the more ordered packing in the solid state. As a result, the film bandgap of Pt-SM-BTD is estimated to be ca. 1.78 eV from the onset of absorption at 695 nm. More interestingly, after thermal or

solvent annealing, we have observed different absorption profiles in the UV-Vis spectrum. Specifically, the thermal annealing experienced more pronounced vibronic structure rather than further red-shifts, while in terms of solvent annealing, we observed another ca. 75 nm shifts resulting in lowest bandgap around 1.61 eV. And the detailed studies regarding this difference are underway right now.

Pt-SM-BTD shows two emissions peaks at ca. 677 nm and 698 nm in solutions (excited at 550 nm) and at ca. 698 nm as thin films (excited at 500 nm), respectively. The emissions did not change with intensity with or without the presence of oxygen. Also based on the relatively small Stokes shift, we assign the emission of Pt-SM-BTD to fluorescence. Unfortunately, we still didn't observe the phosphorescence for either solutions or thin films at room temperature. Such lack of phosphorescence has been observed in previous chapter[63] and other reported Pt-containing low bandgap conjugated polymers and small molecules,[73,81,82,112,114] which is commonly ascribed to the energy gap law.[136]

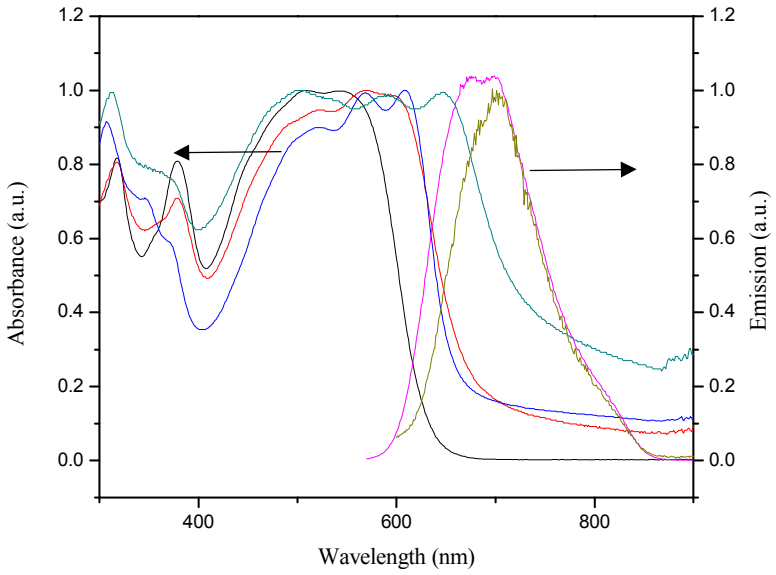

Figure 4.1 UV-Vis absorption and emission spectrum of Pt-SM-BTD in both solution and film. ——Solution (10^{-5} chloroform) UV-Vis; ——Film UV-Vis; —— Film UV-Vis thermal

annealing at 150°C for 10 min; Film UV-Vis solvent (chloroform) annealing for 10 min; Solution (10^{-5} chloroform) emission; Film emission.

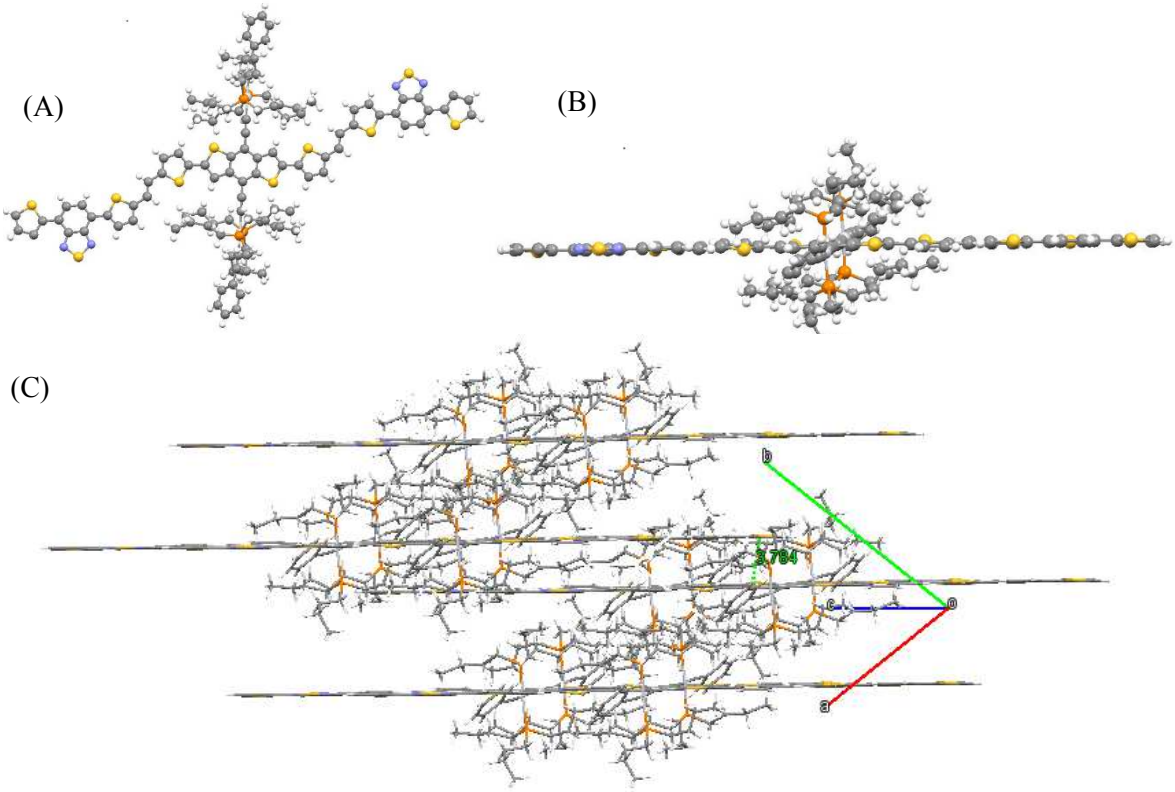

Figure 4.2 Crystal structure of Pt-SM-BTD (A) Crystal structure from front; (B) Crystal structure from side; (C) Packing diagram of Pt-SM-BTD with distance between two layers.

4.2.3 Crystallinity of Pt-SM-BTD

Although we didn't get the single crystal of Pt-SM in chapter 3, fortunately, after the modification of the structure, we successfully obtained the single crystal of Pt-SM-BTD through the two solvents (chlorobenzene and acetonitrile) method. The crystal structure and molecular packing motifs are shown in Fig. 4.2. Noticeably, the conjugated main chain is nearly planar, aligned in parallel, and they are slip-stacked from each other along the arms with tri-n-butylphosphine groups situated in between. Such packing geometry leads

to an inter-chromophore distance of ca. 3.78 Å which is characteristic of typical π-π stacking distances of aromatic molecules. Such π-π stacking motifs are important for electronic coupling among adjacent chromophores and for efficient exciton/charge transport.

The crystallinity of Pt-SM-BTD was further confirmed by differential scanning calorimetry (DSC) and thin film X-ray diffraction (XRD) measurements. As shown in the DSC trace in Fig 4.3, a clear, reproducible melting transition peak at 88°C is seen. Fig 4.4 displays several sharp XRD signals from Pt-SM-BTD films drop-cast onto glass substrates. In addition, the signal at 2θ = 22.3° corresponds to a d-spacing of ca. 3.98 Å, which is closed enough to the results obtained from the structure of the single crystal of Pt-SM-BTD. Both DSC, XRD and single crystal suggest the crystalline nature of Pt-SM-BTD, which has rarely been observed in Pt-bisacetylide containing SMs and polymers.

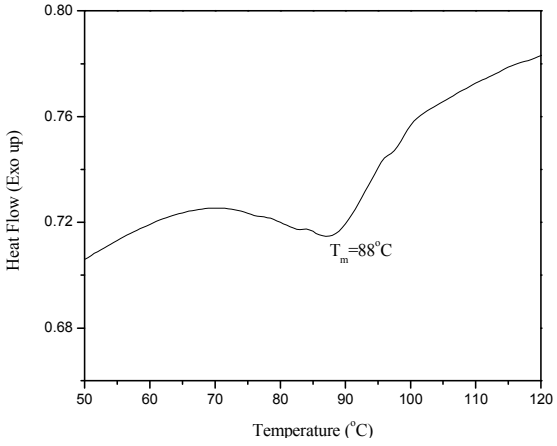

Figure 4.3 Differential scanning calorimetry (DSC) trace (2nd heating, 10 °C/min) of Pt-SM-BTD.

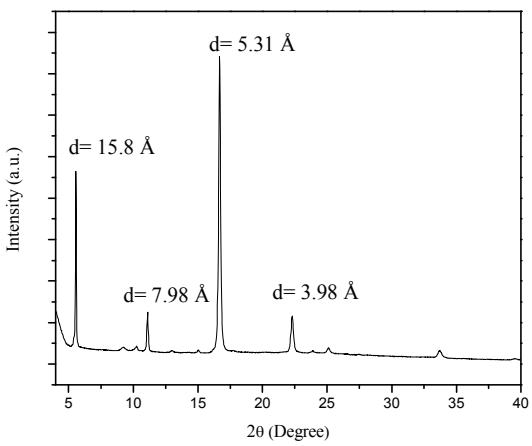

Figure 4.4 X-ray diffraction (XRD) patterns of Pt-SM-BTD after solvent (chloroform) annealing for 10 min

4.2.4 Cyclic Voltammetry Measurements

The HOMO and LUMO levels of Pt-SM-BTD were determined through cyclic voltammetry measurements as shown in Fig. 4.5. One pseudo-reversible reduction and three oxidation peaks are observed, from the onsets of which, the HOMO and LUMO levels are estimated to be ca. -4.91 eV and -3.05 eV, respectively. As a result, the electrochemical bandgap can be calculated around 1.86 eV which is in good agreement with the optical measurements.

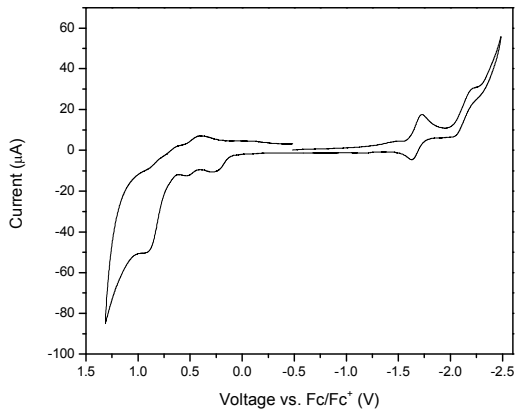

Figure 4.5 Cyclic voltammogram (CV) of Pt-SM-BTD in CH_2Cl_2 (1 mM) using Bu_4NPF_6 as supporting electrolyte (0.1 M). The potential is calibrated externally against ferrocene (Fc) redox couple (4.80 V below vacuum).

4.2.5 Hole Mobility Measurements of Pt-SM-BTD

One key parameter of organic materials for electronic devices is the charge mobility. We have measured hole mobilities of Pt-SM-BTD using space charge limited current (SCLC) method.[185] Hole selective device geometries (ITO/MoO_3/active layer/MoO_3/Al) are employed and the current density-voltage (I-V) curves are shown

in Fig. 4.6. From the linear region of I-V curve, the hole mobility of as-casted film is estimated to be 5.12×10^{-5} $cm^2V^{-1}s^{-1}$ however, the hole mobility greatly increased to 2.02×10^{-4} $cm^2V^{-1}s^{-1}$ after the film was exposed to chloroform vapor for 10 min. indicating a better crystallinity with enhanced charge mobility which is agreed with the results of UV-Vis, and XRD.

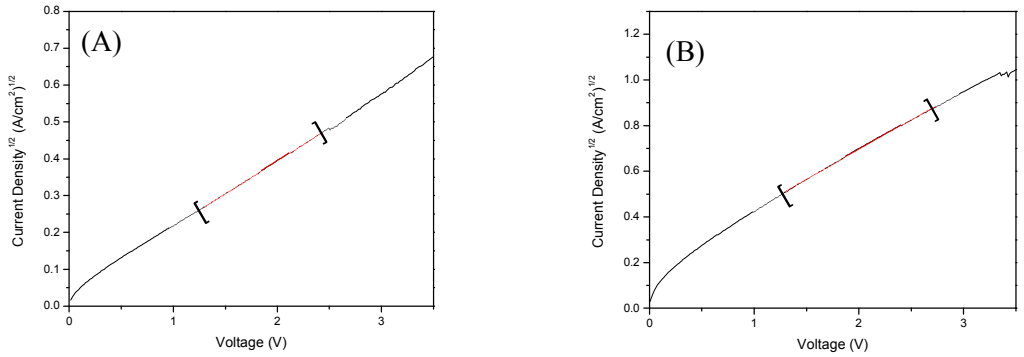

Figure 4.6 Space charge limited current (SCLC) profiles of Pt-SM-BTD (A) as-cast film; (B) solvent (chloroform) annealing for 10 min. The segments within the square brackets are the linear regions used for respective hole mobility calculations.

4.2.6 Time-resolved Transient Absorption Spectroscopy of Pt-SM-BTD

Although we are still unable to directly observe phosphorescence from Pt-SM-BTD, the presence of ISC events and triplet states have been observed by using time-resolved transient absorption spectroscopy as illustrated in Fig. 4.7. The transient absorption spectrum of Pt-SM-BTD features ground state bleach peaks from 350 nm to 600 nm, and a broad excited state absorption from 600 nm to 800 nm. We ascribed the excited state absorption feature to one triplet transition which retrieved time constant of 4.38 μs ± 45 ns. In addition, we temporarily assign the 4.38 μs time

constant observed in the transient kinetics to a triplet charge separated state from the BDT core to the BTD arms, since its time constant is more closed to T2 in the Pt-SM scenario. More detailed studies are being conducted with the help of DFT calculation of Pt-SM-BTD.

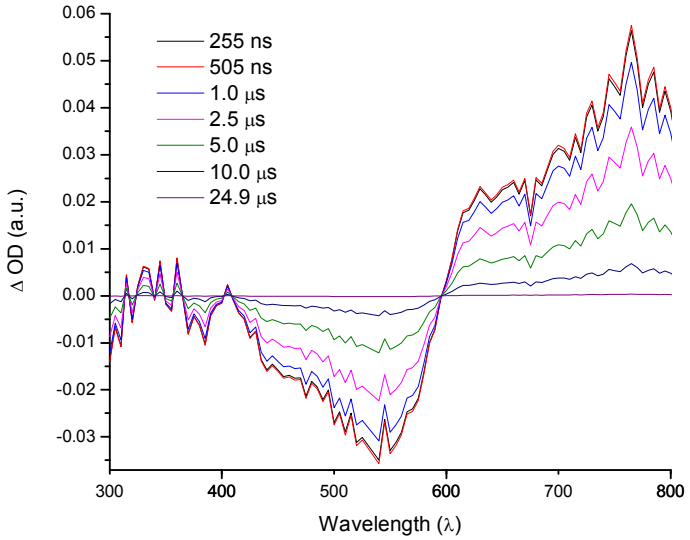

Figure 4.7 Transient absorption spectra of Pt-SM-BTD collected in chlorobenzene, excited at 532 nm with a nanosecond pulse from a SHG Continuum Surelight Nd : YAG at 1 Hz.

4.3 Solar Cell Performance

OSC devices were fabricated using Pt-SM-BTD in device geometries: ITO glass/MoO_3 (10 nm)/organic blend layer/Al (100 nm). The devices were first optimized using blends of phenyl-C_{61}-buyric acid methyl ester ($PC_{61}BM$) by varying the donor/acceptor weight ratios, solvent choices, solution concentrations, spin-coating conditions and thermal/solvent annealing conditions. Table 4.1 summarizes representative device parameters of Pt-SM-BTD from various optimization conditions. The best devices were found to use a Pt-SM-

BTD/$PC_{61}BM$ weight ratio of 1/2 without any post annealing methods. We then substituted $PC_{61}BM$ with phenyl-C_{71}-butyric acid methyl ester ($PC_{71}BM$) in the Pt-SM-BTD by employing the optimized conditions. Fig. 4.8 displays the representative I-V curves (A), and absorption and external quantum efficiency (EQE) profiles (B). The EQE responses closely match the device thin film absorption profiles, displaying panchromatic responses from 350 nm to 700 nm.

Table 4.1 Summary of OSC device performances employing Pt-SM with $PC_{61}BM$ or $PC_{71}BM$ under various fabrication conditions. Averages are calculated from at least five devices and the best values are given in parentheses.

rpm[a]	Conc.[b] mg/mL	wt./wt.[c]	Solv.[d]	Anneal.[e]	V_{oc} (V)	J_{sc} (mA/cm^2)	FF (%)	PCE (%)
1200	10	1:0.8	CF	AC	0.81±0.006 (0.82)	3.46±0.46 (4.17)	31.7±0.50 (32.5)	0.88±0.11 (1.06)
1200	5	1:0.8	CF	AC	0.82±0.007 (0.83)	4.99±0.94 (6.35)	31.8±0.54 (32.8)	1.31±0.26 (1.71)
1200	5	1:2	CF	AC	0.81±0.013 (0.82)	7.75±1.26 (9.92)	39.5±1.22 (42.3)	2.47±0.38 (3.19)
1200	5	1:3	CF	AC	0.77±0.02 (0.79)	6.26±1.07 (8.19)	31.4±1.38 (34.0)	1.51±0.31 (2.07)
800	5	1:2	CF	AC	0.79±0.007 (0.80)	7.25±1.78 (8.71)	32.8±2.28 (35.1)	1.90±0.48 (2.31)
1600	5	1:2	CF	AC	0.81±0.007 (0.82)	8.83±1.52 (10.78)	42.6±1.31 (44.3)	3.06±0.48 (3.65)
2000	5	1:2	CF	AC	0.81±0.006 (0.82)	7.50±1.67 (9.61)	36.8±3.37 (40.2)	2.26±0.60 (2.91)
1200	5	1:2	CB	AC	0.80±0.008 (0.81)	4.05±0.79 (4.86)	41.9±3.97 (44.8)	1.35±0.27 (1.72)
1600	5	1:2	CF	SA1	0.80	7.53±1.46 (8.91)	35.8±0.88 (36.6)	2.16±0.44 (2.61)
1600	5	1:2	CF	SA2	0.79±0.014 (0.81)	7.50±1.24 (9.67)	37.8±3.73 (41.0)	2.27±0.47 (2.92)
1600	5	1:2	CF	SA3	0.79±0.005 (0.80)	5.59±1.25 (6.74)	34.4±4.20 (37.5)	1.52±0.35 (1.92)
1600	5	1:2	CF	TA	0.80±0.006 (0.81)	7.10±1.22 (8.75)	32.0±4.45 (35.2)	1.83±0.47 (2.42)
1600	5	1:2	CF	AC[e]	0.810.014 (0.82)	4.51±0.77 (5.19)	33.2±2.17 (38.8)	1.21±0.18 (1.46)
1600	5	1:2[c´]	CF	AC	0.79±0.003 (0.80)	11.17±0.96 (12.87)	36.0±1.69 (38.5)	3.20±0.33 (3.92)

[a] Spin coating speed; all for 30s. [b] Concentration of Pt-SM-BTD. [c] Pt-SM-BTD/$PC_{61}BM$ weight ratio. [c´] Pt-SM-BTD/$PC_{71}BM$ weight ratio. [d] Solvent; CF: chloroform; CB:

chlorobenzene e Annealing conditions; AC: as cast; TA1: thermal annealing at 100 °C for 5 min after deposition of Al; SA1: solvent (CF) annealing for 30 m sec before deposition of Al; SA2: solvent (CF) annealing for 1 min before deposition of Al; SA3: solvent (CF) annealing for 2 min before deposition of Al. [e] Using LiF as the cathode interfacial layer.

Unlike Pt-SM, the annealing methods provided negative effect on the performances of devices. Although the solvent annealing can provide smaller bandgap and higher hole mobility which are supposed to be beneficial to the PCEs, the increased crystalline nature of Pt-SM-BTD tends to contribute to macrophase separation after the annealing conditions leading to worse morphology with phase sizes around micrometer scale which can be proved by the decreased values of FF, optical microscopy (Fig 4.8 C and D) and TEM images (Fig 4.8 E and F).

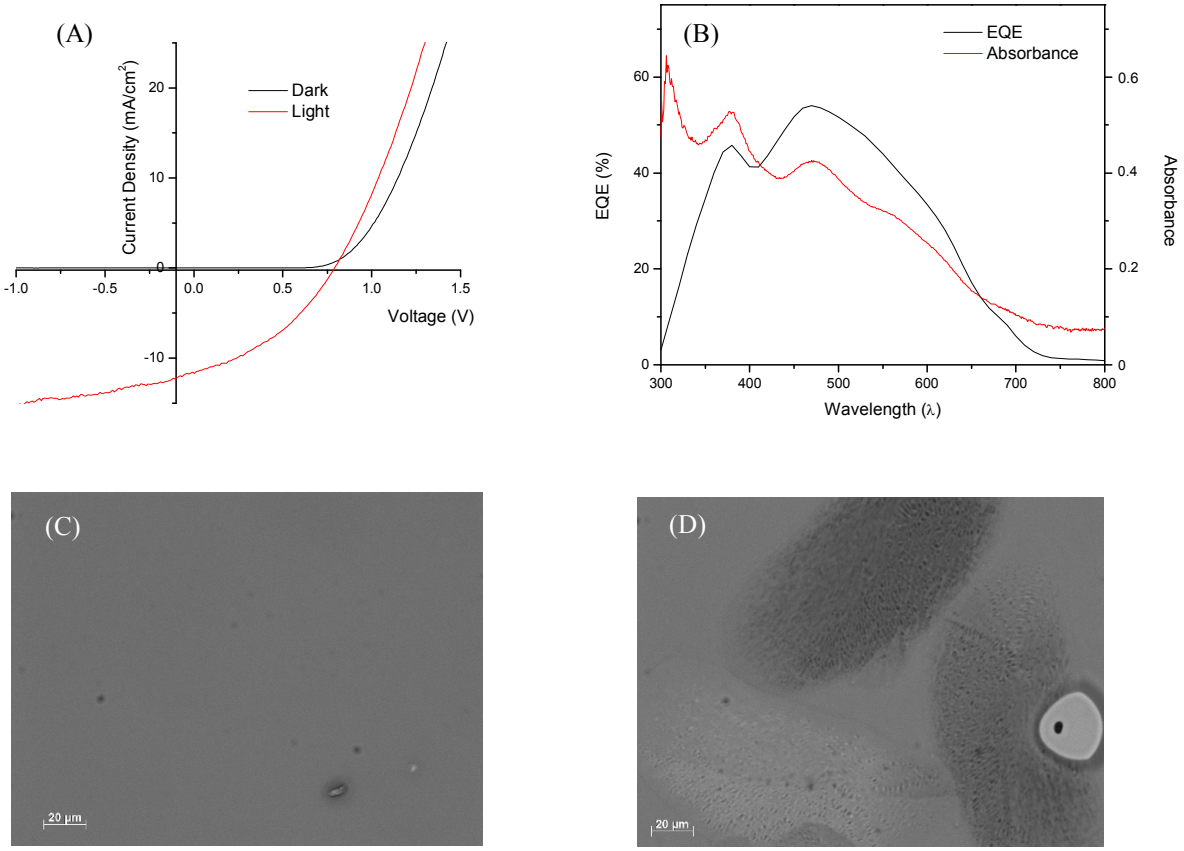

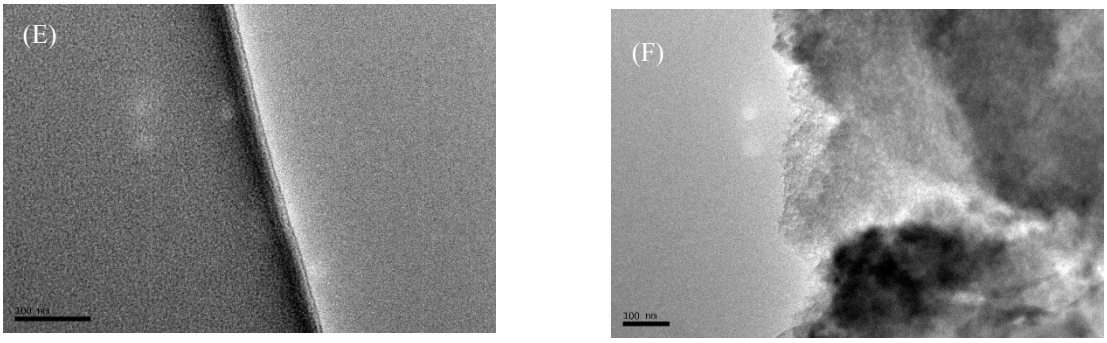

Figure 4.8 (A) Current density-voltage (I-V) curves of a representative OSC device. (B) Absorption and external quantum efficiency (EQE) profiles of the same device. (C) Optical microscopy image of the as-casted active layer of the device (scale bar is 20 nm). (D) Optical microscopy image of the active layer of the device after solvent (chloroform) annealing for 2 min. (E) TEM image of the as-casted active layer of device. (F) TEM image of the active layer of the device after solvent (chloroform) annealing for 2 min.

4.4 Conclusion

In summary, we have designed and synthesized a new derivative of Pt-bisacetylide containing SM, featuring "roller-wheel" geometry which has been well demonstrated by its single crystal structure. This new structural design allows partial overlap among the main rigid chromophores, leading to enhanced crystallinity and π–π interactions. However, OSCs employing Pt-SM-BTD didn't further improve PCEs compared to that of Pt-SM, mostly resulted from higher crystallinity of the compound leading to a bad morphology of the active layer. The drop of PCEs showed us that more balanced conditions including bandgap, crystallinity, hole mobility and morphology should be under consideration in order to achieve the best performance in the organic solar cells.

4.5 Experimental

4.5.1 Materials and General Methods

All reagents and solvents were used as received from Sigma-Aldrich or VWR unless otherwise noted. Anhydrous THF was distilled over Na/benzophenone prior to use. Anhydrous chloroform and triethylamine (TEA) were obtained by distillation over CaH_2 and degassed through several freeze-pump-thaw cycles. Phenyl-C_{61}-butyric acid methyl ester ($PC_{61}BM$) and phenyl-C_{71}-butyric acid methyl ester ($PC_{71}BM$) were purchased from American Dye Source. N,N-Diethyl-3-thiophenecarboxamide (1),[186] benzo[1,2-b:4,5-b']dithiophene-4,8-dione (2),[187] benzo[1,2-b:4,5-b']dithiophene-4,8-bis[2-[triisopropylsilyl]ethynyl] (3),[188] 2,6-dibromo-4,8-bis[2- [triisopropylsilyl]ethynyl] (4),[189] Trans-Chloro(phenylethynyl)bis(bributylphosphine)platinum(7),[172] 4,7-Di-2-thienyl-2,1,3-benzothiadiazole (9),[197] 5-[7-(2-thienyl)-2,1,3-benzothiadiazol-4-yl]-2-thiophenecarboxaldehyde (10),[198] 5-[7-(2-thienyl)-2,1,3-benzothiadiazol-4-yl]-2-thiophenemethanol (11),[199] were synthesized according to literature procedures. 300.13 MHz ^{1}H, 75.48 MHz ^{13}C, 121.5 MHz ^{31}P spectra were recorded on a Bruker Avance III Solution 300 spectrometer. All solution ^{1}H spectra were referenced internally to tetramethylsilane and ^{13}C spectra were referenced internally to chloroform. ^{31}P was referenced externally by using standards H_3PO_4 ($\delta = 0$ ppm). Ultraviolet visible (UV-Vis) absorption spectra were recorded on a Shimadzu UV-2401 PC spectrometer over a wavelength range of 300−900 nm. Fluorescence emission spectra were obtained using a Varian Cary Eclipse Fluorimeter. Differential scanning calorimetry (DSC) measurements were performed on a Mettler Toledo DSC STARe system with ca. 8 mg sample and at a scan rate of 10 °C/min. The results reported are from the second heating cycle. Cyclic voltammetry (CV) was performed at 25 °C on a CH Instrument CH1604xD electrochemical analyzer using a glassy carbon working electrode, a platinum wire counter

electrode and Ag/AgCl reference electrode, calibrated using a ferrocene redox couple (4.8 eV below vacuum). X-ray diffraction (XRD) data was collected using a Rigaku SmartLab diffractometer in Bragg-Brentano mode employing Cu K-α radiation and a D/tex 1-dimensional detector. A nickel filter was used to remove the Cu K-β radiation component. Data was collected over a 2θ range from 5° to 40° using 0.02° step size at a scan rate of 1°/min. Transmission electron microscopy (TEM) images were taken on a JEOL 2010 EX HREM with an Oxford-Link EDS Gatan Digital Micrograph equipped with a slow scan CCD camera. Samples were prepared by soaking solar cell devices employing PEDOT: PSS as anode interfacial layers in water and fishing our floating active layers with carbon coated TEM grids. High resolution mass spectrometry (HRMS) was analyzed by Mass Spectrometry using Electrospray Ionization (ESI) in positive mode on a Waters LCT Premier Time of Flight (TOF) mass spectrometer. Transient absorption lifetimes were collected on an Edinburgh Instruments LP920 Laser Flash Photolysis Spectrometer. The excitation source consists of a Continuum Surelight II Model SLI-10 (Nd:YAG, 10 Hz) with SHG and THG options to generate 532 nm and 355 nm wavelengths. A Surelight SSP (dichroic to separate the 532 and 355) is positioned in between the laser to select the desired pump wavelength. A 450W ozone free Xenon arc lamp generates a microsecond white light supercontinuum probe beam, which is arranged in a 90° cross-beam geometry excitation beam at the sample. The probe beam passes through a monochromator and is captured by a Hamamatsu R928 PMT. Individual single wavelength kinetics are collected at a 2 nm step size to construct transient absorption spectra at specific times. Transient data are fit by re-convolution in SurfaceXplorer (v. 4) using a second order multiexponential decay with a fixed Instrument Response Function of 40 ns.

4.5.2 Solar Cell Fabrication and Testing

Pt-SM-BTD/$PC_{61}BM$ or $PC_{71}BM$ blend solutions were prepared by dissolving Pt-SM-BTD and $PC_{61}BM$ or $PC_{71}BM$ at predetermined weight ratios in chloroform at a Pt-SM concentration of 0.5 wt% and stirred at room temperature for 3-4 hours in a nitrogen glovebox (Innovative Technology, model PL-He-2GB, O_2 < 0.5 ppm, H_2O < 0.5 ppm). Solar cell devices were fabricated according to the following procedure: ITO-coated glass substrates (China Shenzhen Southern Glass Display Ltd.; 8 Ω/□) were cleaned by ultrasonication sequentially in detergent water, DI water, acetone and isopropyl alcohol, each for 15 min. These ITO-coated glasses were further treated by UV-ozone (PSD Series, Novascan) for 60 min before being transferred to a nitrogen glovebox (Innovative Technology, model PL-He-2GB, O_2 < 0.1 ppm, H_2O < 0.1 ppm) for MoO_3 deposition. MoO_3 (10 nm) was deposited using an Angstrom Engineering Amod deposition system at a base vacuum level of < 4×10^{-7} Torr. The Pt-SM-BTD/fullerene blend solution was first filtered through a 0.45 μm PTFE filter and spin-coated on top of the MoO_3 layer at 1200 rpm for 30 s. Al (100 nm) was thermally evaporated through patterned shadow masks as anodes, the sizes of which define the active areas of the solar cells to be 7.1 mm^2. Current-voltage (I-V) characteristics were measured using a Keithley 2400 source-measuring unit under simulated AM 1.5G irradiation (100 mW/cm^2) generated by a Xe acr-lamp based Newport 67005 150 W solar simulator equipped with an AM 1.5G filter. The light intensity was calibrated using a Newport thermopile detector (model 818P-010-12) equipped with a Newport 1916-C optical Power Meter. External quantum efficiency (EQE) values were measured by using a commercial solar cell quantum efficiency measurement system

(Model QEXL, PV Measurements, Inc., Boulder, CO). The EQE system was calibrated with a Si photodiode certified by the National Renewable Energy Laboratory (NREL).

4.5.3 Experimental Details

Compound 5 Weight 1 g (1.42 mmol) compound 4, 1.57 g (3.54 mmol) tributyl[5-(1,3-dioxolan-2-yl)-2-thienyl] stannane and 82 mg (5 mol%) $Pd(PPh_3)_4$ in a pressure-vessel. The solid was dissolved in 20 mL toluene and warm up to the temperature of 120 ℃. The reaction was stopped after 12 hours and solvent was dried in vacuum. The crude product was re-dissolved in THF and 5 mL 1M HCl was added. After 1 hour, the reaction mixture was extracted with chloroform for 3 times and the organic phase was combined and washed with water, brine and finally dried over Na_2SO_4. The crude product was purified by column chromatography on silica gel using hexane/dichloromethane as eluent and the product was further purified by recrystallization (MeOH: $CHCl_3$). (873.9 mg, 80% yield) The product is an orange solid. ^1H NMR (300.13 MHz, $CDCl_3$): δ (ppm) = 9.93 (s, 2H), 7.82 (s, 2H), 7.76 (d, 2H), 7.43 (d, 2H), 1.28 (s, 42H).

Compound 6 5 mL THF and 0.1 mL H_2O was added to compound 5 (64 mg, 0.083 mmol) in a Schleak flask and the resulting solution was bubbled for 15 minutes followed by the addition of TBAF (65 mg, 0.249 mmol) which has been dissolved in 2 mL THF. The reaction ran under the protection of N_2 for 2 hours and the solvent was evaporated under reduced pressure. The crude product was washed by methanol and the product was collected by filtration. The product will go to next step without purification.

Compound 8 To a small vial, compound 6 (32 mg, 0.069 mmol), compound 7 (123mg, 0.167 mmol) and 1 mg CuI were added in the glove box. After 3 mL anhydrous chloroform and 0.25 mL TEA was injected and the mixture was stirred at room temperature. The

reaction was stopped after 12 hours, the solvent was removed under reduced pressure, the crude product was purified by column chromatograph using the mixture of hexane and DCM as an eluent and the product was further purified by recrystallization (chloroform: MeOH). The product is a red solid. (103.7 mg, 80% yield) ^{1}H NMR (300.13 MHz, $CDCl_3$): δ (ppm) = 9.90 (s, 2H), 7.86 (s, 2H), 7.20 (d, 2H), 7.30 (m, 12H), 2.18 (m, 24H), 1.67 (m, 24H), 1.42 (m, 24H), 0.91 (t, 36H). ^{31}P NMR (121.5 MHz, $CDCl_3$): δ (ppm) = 4.04. ^{13}C NMR (75.48 MHz, $CDCl_3$): δ (ppm) = 182.3, 148.0, 142.3, 139.7, 138.5, 137.1, 135.2, 130.8, 128.9, 127.8, 124.9, 124.8, 123.1, 115.1, 109.6, 107.1, 105.0, 26.5, 24.5, 24.4, 24.3, 24.0, 13.9.

Compound 12 Compound 11 (81.2 mg, 0.24 mmol) and pyridine (0.13 mL, 1.40 mmol) were dissolved in toluene 10.0 mL at 0°C. Thionyl chloride (0.15mL, 2.05 mmol) was then added in a dropwise manner at the same temperature. The resulting mixture was stirred at 0°C for 1 hour followed by stirring at room temperature for 12 hours under nitrogen. The excess thionyl chloride and toluene was removed under reduced pressure. The residue was washed with methanol and isolated as an orange-red solid, which was employed to the next step without further purification. (55.7 mg, 65% yield) ^{1}H NMR (300.13 MHz, $CDCl_3$): δ (ppm)= 8.13 (d, 1H), 7.95 (d, 1H), 7.87 (d, 2H), 7.86 (d, 2H), 7.48 (d, 2H), 7.18 (m, 2H) 4.87 (s, 2H). ^{13}C NMR (75.48 MHz, $CDCl_3$): δ (ppm) = 152.4, 152.3, 141.2, 140.6, 139.1, 128.5, 128.0, 127.6, 127.0, 126.9, 126.2, 125.6, 125.5, 125.3, 40.6.

Compound 13 Compound 12 (90 mg, 0.258 mmol) was mixed with $P(OMe_3)$ (3 mL). The resulting mixture was stirred at 135 °C for 12 hours under argon. After cooling to room temperature, the solvent was removed by reduced pressure and the crude product was purified by column (Hexane/Dichloromethane). The product is a dark-red solid. (37 mg,

34% yield) ^{1}H NMR (300.13 MHz, $CDCl_3$): δ (ppm)= 8.00 (d, 1H), 7.86 (d, 1H), 7.65 (d, 1H), 7.63 (d, 1H), 7.40 (d, 1H), 7.13 (dd, 1H), 7.02 (dd, 1H), 3.79 (d, 6H), 3.45 (d, 2H). ^{31}P NMR (121.5 MHz, $CDCl_3$): δ (ppm) = 26.9. ^{13}C NMR (75.48 MHz, $CDCl_3$): δ (ppm) = 152.1, 152.0, 139.0, 138.6, 138.5, 133.5, 133.4, 128.3, 128.2, 127.7, 127.4, 127.3, 127.2, 126.5, 125.4, 125.2, 124.9, 53.0, 52.9, 28.1, 26.2.

Pt-SM-BTD Compound 13 (180 mg, 0.426 mmol.) in THF (15 mL) was added to compound 8 (285 mg, 0.153 mmol) in THF (5 mL). Potassium tert-butoxide (69 mg, 0.613 mmol) dissolved in THF was added in a dropwise manner to the solution at room temperature. The resulting mixture was immediately turned from red-orange to dark-purple with an enhancement in viscosity. The reaction was stopped after 12 hours. The solvent was removed by reduced pressure and the crude product was purified by column (Hexane/Dichloromethane) and the product was further purified by recrystallization (chloroform: MeOH) The product is a dark color solid. (300 mg, 75% yield) ^{1}H NMR (300.13 MHz, $CDCl_3$): δ (ppm) = 8.14 (dd, 2H), 8.07 (d, 2H), 7.90 (dd, 4H), 7.68 (s, 2H), 7.48 (dd, 2H), 7.32 (m, 4H), 7.15 (m, 18H), 2.21 (m, 24H), 1.70 (m, 24H), 1.48 (m, 24H), 0.95 (t, 36H). ^{31}P NMR (121.5 MHz, $CDCl_3$): δ (ppm) = 4.00. ^{13}C NMR (75.48 MHz, $CDCl_3$): δ (ppm) = 152.7, 152.5, 143.7, 141.8, 139.6, 138.8, 138.4, 138.2, 137.8, 135.9, 130.9, 129.0, 128.3, 128.0, 127.8, 127.6, 127.5, 126.9, 125.9, 125.8, 125.6, 125.4, 124.9, 122.0, 121.3, 120.5, 114.2, 109.6, 107.9, 107.7, 107.5, 105.3, 26.5, 24.5, 24.4, 24.3, 24.2, 24.0, 13.9. HRMS: (ESI): $C_{118}H_{142}N_4P_4Pt_2S_{10}$, calcd, 2448.6688 for [$M^+$]; found, 2448.6716 for [M^+].

Chapter 5

A Novel Ionic Fullerene that Act as an Acceptor in the Organic Solar Cells

5.1 Introduction

The state-of-art acceptor in the organic solar cells is well-known PCBM and the combinations of PCBM with various conjugated polymers and small molecules have pushed the efficiencies of OPVs to more than 10%.[27,28] The excellence for PCBM as an acceptor come from: 1) The existence of low-lying excited states in their monoanions, which leads to substantial enhancement in charge separation rates.[200] 2) Nanoscale phase separation and continuous pathway for efficient charge separation and transport.[201] 3) Three-dimensional (3D) spherical structure which enables enhanced entropic effects (ΔS) and enables isotropic charge transport.[202] As a results, the efficiency of the charge transfer from the donor to acceptor is closed to unit.[16] However, since the LUMO level of PCBM is around 3.7eV- 4.2eV which is good enough to capture the singlet exciton, PCBM is not a suitable candidate to consider as a triplet acceptor. Therefore, from previous two chapters, PCBM can capture none of the triplet excitons of the Pt-containing small molecules.

So far, the widely used triplet acceptors are mainly organic small molecules and their applications are focused on the triplet-triplet annihilation (TTA) or light emitting devices.[203–205] Unfortunately, those acceptors are not working well in the OSCs system since it is hard for the acceptors to form continuous pathways for the transport of electron leading to huge recombination.

In order to solve this problem, we can either design new donors with a higher T_1 state and continue to use PCBM as the acceptor, or design new fullerene derivatives with a lower LUMO level. According to papers reported, the best way to increase the T1 state is to apply strong electron-withdrawing group in the compounds or break the planarity of the structure which will cause less or even zero overlapping between HOMO and LUMO resulting a small $\Delta E_{S1\text{-}T1}$.[203–212] Nevertheless, the PCEs of the devices will suffer if we apply these compounds as donors because the excitons formed in the active layer can hardly migrate which will lead to a great amount of recombination. Therefore, we proposed here a novel fullerene derivative named as $C_{60}^{+}SDS^{-}$ (Scheme 5.1) which possesses both the advantages of PCBM and the lower LUMO level because of the ionic nature of the compound. As a result, this new fullerene derivative can potentially become an ideal acceptor for triplet excitons in the organic solar cells.

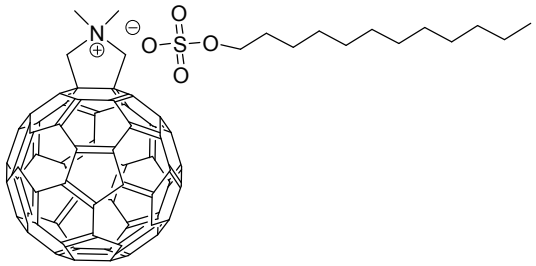

Scheme 5.1 Structure of $C_{60}^{+}SDS^{-}$

5.2 Results and Discussion

5.2.1 Synthesis of $C_{60}^{+}SDS^{-}$

Synthetic procedures toward the target compound $C_{60}^{+}SDS^{-}$ are outlined in Scheme 5.2 and the synthetic details are included in the Section 5.3.2. The functionalization of the fullerene was conducted through classic Prato reaction. The quaternization of pyrrolidinofullerene led to the compound $C60^{+}I^{-}$ which would finally exchange with SDS

to from target compound $C_{60}^{+}SDS^{-}$. The $C_{60}^{+}SDS^{-}$ is highly soluble in polar solvent such as DMSO and slightly soluble in common organic solvents including chlorobenzene and chloroform. The synthesis of $C_{60}^{+}SDS^{-}$ is easy and straightforward with high yield therefore, this methodology can be easily modified to attain various fullerene derivatives with different functional groups.

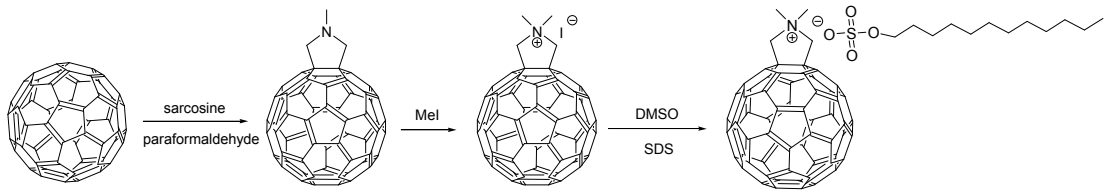

C_{60} pyrrolidinofullerene $C_{60}^{+}I^{-}$ $C_{60}^{+}SDS^{-}$

Scheme 5.2 Synthesis of $C_{60}^{+}SDS^{-}$.

5.2.2 Cyclic Voltammetry Measurements of PCBM, C_{60}, PF, $C_{60}^{+}I^{-}$ and $C_{60}^{+}SDS^{-}$

Electrochemistry is the most crucial property for each of the fullerene derivatives in this project. Therefore, each LUMO level of PCBM, C_{60}, PF, $C_{60}^{+}I^{-}$ and $C_{60}^{+}SDS^{-}$ were determined through cyclic voltammetry measurements as shown in Fig. 5.1 and summarized in Table 5.1. Each compound exhibited 2 or 3 quasi-reversible reduction peaks in the negative potential range from 0 to – 2.2 eV. The first reduction potential shifted positively from PCBM, to C_{60} and finally to ionic fullerene. From the onset of first reduction peak, the LUMO of each compound can be calculated to be -3.77 eV, -3.77 eV, -3.86 eV, -3.93 eV and -3.94 eV for PCBM, PF, C_{60}, $C_{60}^{+}I^{-}$ and $C_{60}^{+}SDS^{-}$ respectively through the equation LUMO = - (E_{red}^{on}+4.8). The LUMO level of ionic fullerene is decreased by 0.17 eV in comparison with that of PCBM which indicates the electron is stabilized by the cation in the fullerene.

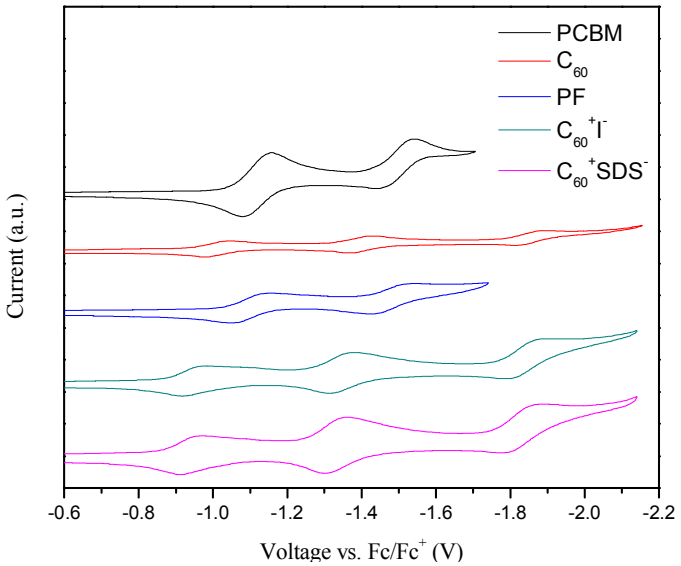

Figure 5.1 Cyclic voltammogram (CV) of PCBM, C_{60}, PF, $C_{60}^{+}I^{-}$ and $C_{60}^{+}SDS^{-}$ in CH_2Cl_2 (1 mM) using Bu_4NPF_6 as supporting electrolyte (0.1 M). The potential is calibrated externally against ferrocene (Fc) redox couple (4.80 V below vacuum).

5.2.3 Time-resolved Transient Absorption Spectroscopy Measurements

From chapter 3, we have successfully proved the existence of triplet excitons of Pt-SM by using time-resolved transient absorption spectroscopy and found out the excited state absorption is from 600 nm to 800 nm. Unfortunately, the PCBM can't quench the triplet excitons since there is almost no change in the life time of triplet excitons. On the other hand, $C_{60}^{+}SDS^{-}$ because of its lower LUMO level can capture the triplet excitons of Pt-SM effectively because the life time of triplet has been greatly suppressed from 16 μs to 10 μs when 5 eq $C_{60}^{+}SDS^{-}$ was added. (Figure 5.2 and Table 5.1) More interestingly, after adding 5 eq C_{60}, one of the triplet exciton life time has dropped, however the amount of decrease is smaller than the amount in terms of $C_{60}^{+}SDS^{-}$ which means the triplet energy level is

really close to the LUMO level of C_{60}. As a result, an ideal acceptor for Pt-SM should hold its LUMO level from -3.86 eV to -3.94 eV.

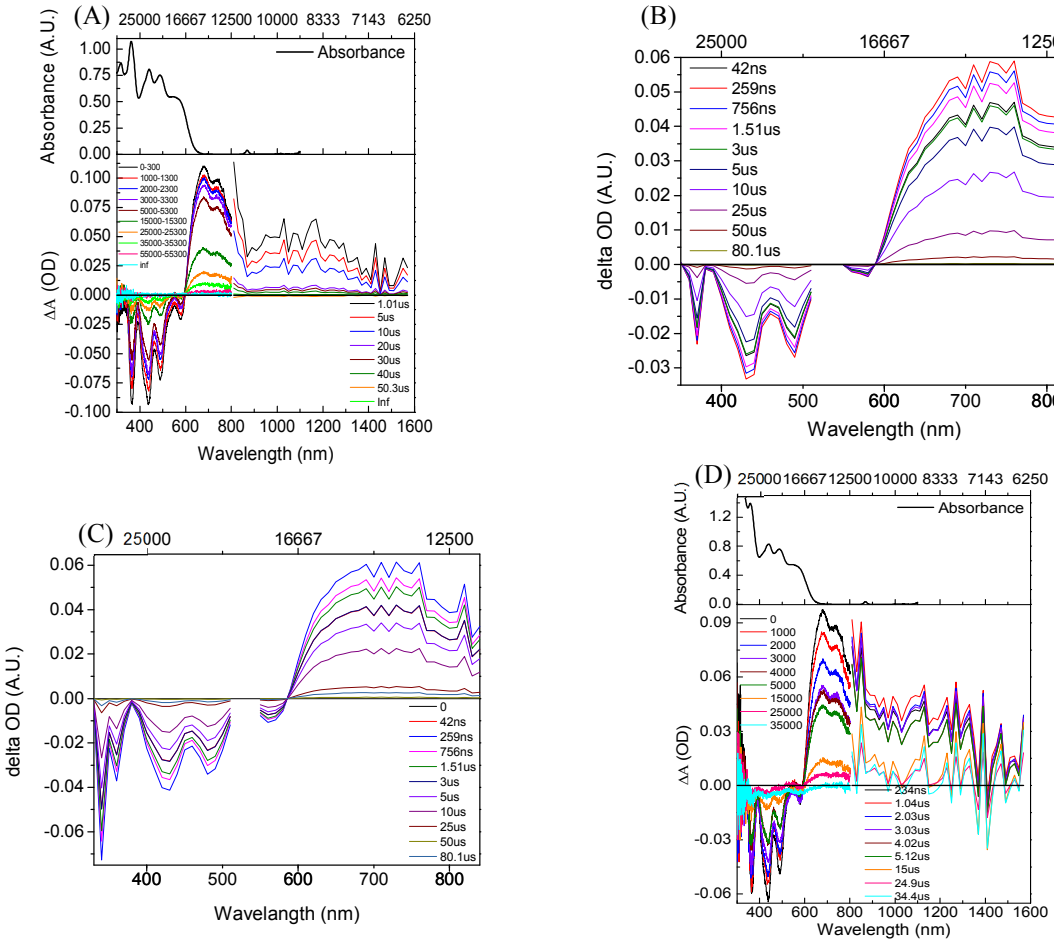

Figure 5.2 Time-resolved transient absorption spectroscopy, (A) Pure Pt-SM; (B) Pt-SM/5eq PCBM; (C) Pt-SM/5eq C_{60}; (D) Pt-SM/5eq $C_{60}^{+}SDS^{-}$

Table 5.1 Summary of lifetimes of Pt-SM with different acceptors

	LUMO of acceptor (eV)	A_1(%)	τ_1(ns)	A_2(%)	τ_2(ns)
Pt-SM	/	42	6000	58	17000
Pt-SM/5eq PCBM	3.77	33	6730	67	16900
Pt-SM/5eq C_{60}	3.86	60	6340	40	13000
Pt-SM/5eq $C_{60}^{+}SDS^{-}$	3.94	22	4800	78	10560

All the data were obtained from wavelength 700 nm

5.2.4 Conclusion

We have successfully designed and synthesized a novel fullerene derivative $C_{60}^{+}SDS^{-}$ with a lower LUMO level. Through the measurement of time-resolved transient absorption spectroscopy, we can find the $C_{60}^{+}SDS^{-}$ can successfully quench the triplet exciton of Pt-SM since the life time was greatly suppressed after 5 eq $C_{60}^{+}SDS^{-}$ was added.

5.2.5 Outlook

Through novel design, the new fullerene derivative $C_{60}^{+}SDS^{-}$ has successfully captured the triplet exciton, however, the lower LUMO of acceptor will inevitably decrease the V_{oc} of the organic solar cell which will finally lead to a bad performance in the OPV devices. As a result, the best scenario is to increase the T1 state of Pt-containing polymers or small molecules through new designs. One possible proposal could be using the same configuration of donor and acceptor in the main chain, then after introducing some steric hindrance group, we can slightly twist the main chain. By doing so we can create a system with less HOMO-LUMO overlap which will increase the T1 state, while still guaranteeing there is enough π-π stacking for mobility of charge carriers.

Although, the long chain from SDS helps to increase the soluble properties of the new fullerene, the absolute solubility for this compound is still limited in common organic solvents. (1mg/mL in chlorobenzene) Therefore, in order to further increase the solubility, a branched chain can be applied instead of linear one.

Finally, using Pt-SM and $C_{60}^{+}SDS^{-}$ to fabricate organic solar cells, for example a bilayer structure can be developed. Therefore, we can first estimate the diffusion length of triplet

exciton and then using time-resolved transient absorption spectroscopy and other characterization techniques to study the photophysics of the system in detail.

5.3 Experimental

5.3.1 Materials and General Methods

All reagents and solvents were used as received from Sigma-Aldrich or VWR unless otherwise noted. Phenyl-C_{61}-butyric acid methyl ester ($PC_{61}BM$) was purchased from American Dye Source. 300.13 MHz ^{1}H, 75.48 MHz ^{13}C, were recorded on a Bruker Avance III Solution 300 spectrometer. All solution ^{1}H spectra were referenced internally to tetramethylsilane and ^{13}C spectra were referenced internally to chloroform. Cyclic voltammetry (CV) was performed at 25 °C on a CH Instrument CH1604xD electrochemical analyzer using a glassy carbon working electrode, a platinum wire counter electrode and Ag/AgCl reference electrode, calibrated using a ferrocene redox couple (4.8 eV below vacuum). High resolution mass spectrometry (HRMS) was analyzed by Mass Spectrometry using Electrospray Ionization (ESI) in positive mode on a Waters LCT Premier Time of Flight (TOF) mass spectrometer. Transient absorption lifetimes were collected on an Edinburgh Instruments LP920 Laser Flash Photolysis Spectrometer. The excitation source consists of a Continuum Surelight II Model SLI-10 (Nd:YAG, 10 Hz) with SHG and THG options to generate 532 nm and 355 nm wavelengths. A Surelight SSP (dichroic to separate the 532 and 355) is positioned in between the laser to select the desired pump wavelength. A 450W ozone free Xenon arc lamp generates a microsecond white light supercontinuum probe beam, which is arranged in a 90° cross-beam geometry excitation beam at the sample. The probe beam passes through a monochromator and is captured by a Hamamatsu R928 PMT. Individual single wavelength kinetics are collected

at a 2 nm step size to construct transient absorption spectra at specific times. Transient data are fit by re-convolution in SurfaceXplorer (v. 4) using a second order multiexponential decay with a fixed Instrument Response Function of 40 ns.

5.3.2 Experimental Details

Pyrrolidinofullerene C_{60} (540 mg, 0.75 mmol) was dissolved in toluene (600 ml) by sonicating for 5 minutes. To this solution were added sarcosine (133.6 mg, 1.50 mmol) and paraformaldehyde (112.5 mg, 3.75 mmol), the reaction mixture was refluxing at 140 ℃for 2 hours. Solvents were removed on a rotavap under vacuum. The product was dissolved in a minimum amount of toluene and loaded onto a silica gel column packed with toluene and eluted with toluene containing 0-5% acetone to collect pure compound. (200 mg, Yield 34.3%) ^{1}HNMR (300.13 MHz, $CDCl_3$), δ(ppm) = 3.01 (s, 3H), 4.41 (s, 4H).

$C_{60}^+I^-$ Methylation of pyrrolidinofullerene (139.9 mg, 0.18 mmol) was carried out by mixing pyrrolidinofullerene with MeI (2.5 g, 18 mmol). The mixture was refluxed at 60 °C for 3 days. After cooling down, 10-20 mL hexane was added, and the product was collected through filtration and washed with more toluene. Pure methylated product $C60^+I^-$ was a dark solid. (150 mg, Yield 88.6%) ^{1}H NMR (300.13 MHz, DMSO-d_6), δ(ppm) = 4.07 (s, 6H), 5.73 (s, 4H).

$C_{60}^+SDS^-$ Dissolve $C60^+I^-$ (50 mg, 0.054 mmol) in 5 mL DMSO and SDS solution (18.3 mg, 0.065 mmol in 5 mL DMSO) was slowly added. The reaction was stopped after 12 hours at room temperature and then 10 mL H_2O was added. After another 12 hours, the product was collected by filtration and washed with more water. The product is a dark brown solid. (51.8 mg, Yield 90.0%) ^{1}HNMR (300.13 MHz, $CDCl_3$), δ(ppm) = 5.73 (s, 4H), 4.07 (s, 6H), 3.65 (t, 2H), 1.45 (t, 2H), 1.23 (m, 16H), 0.82 (t, 2H)

References

(1) Lu, L.; Zheng, T.; Wu, Q.; Schneider, A. M.; Zhao, D.; Yu, L. *Chem. Rev.* **2015**, *115*, 12666–12731.

(2) Sun, K.; Shen, S.; Liang, Y.; Burrows, P. E.; Mao, S. S.; Wang, D. *Chem. Rev.* **2014**, *114*, 8662–8719.

(3) Weinstein, L. A.; Loomis, J.; Bhatia, B.; Bierman, D. M.; Wang, E. N.; Chen, G. *Chem. Rev.* **2015**, *115*, 12797–12838.

(4) U.S. Energy Information Administration. *Off. Integr. Int. Energy Anal.* **2015**, *1*, 1–244.

(5) Tao, M. *Electrochem. Soc. Interface* **2008**, *17*, 30–35.

(6) Cheng, Y.-J.; Yang, S.-H.; Hsu, C.-S. *Chem. Rev.* **2009**, *109*, 5868–5923.

(7) Günes, S.; Neugebauer, H.; Sariciftci, N. S. *Chem. Rev.* **2007**, *107*, 1324–1338.

(8) Zhang, Q.; Kan, B.; Liu, F.; Long, G.; Wan, X.; Chen, X.; Zuo, Y.; Ni, W.; Zhang, H.; Li, M.; Hu, Z.; Huang, F.; Cao, Y.; Liang, Z.; Zhang, M.; Russell, T. P.; Chen, Y. *Nat. Photonics* **2014**, *9*, 35–41.

(9) Huang, Q.; Li, H. *Chinese Sci. Bull.* **2013**, *58*, 2677–2685.

(10) Grätzel, M. *J. Photochem. Photobiol. C Photochem. Rev.* **2003**, *4*, 145–153.

(11) Shalini, S.; Balasundara prabhu, R.; Prasanna, S.; Mallick, T. K.; Senthilarasu, S. *Renew. Sustain. Energy Rev.* **2015**, *51*, 1306–1325.

(12) Song, Z.; Watthage, S. C.; Phillips, A. B.; Heben, M. J. *J. Photonics Energy* **2016**,

6, 22001.

(13) Brenner, T. M.; Egger, D. A.; Kronik, L.; Hodes, G.; Cahen, D. *Nat. Rev. Mater.* **2016**, *1*, 15007.

(14) Thompson, B. C.; Fréchet, J. M. J. *Angew. Chemie Int. Ed.* **2008**, *47*, 58–77.

(15) Tang, C. W. *Appl. Phys. Lett.* **1986**, *48*, 183–185.

(16) Yu, G.; Gao, J.; Hummelen, J. C.; Wudl, F.; Heeger, A. J. *Science (80-.).* **1995**, *270*, 1789–1791.

(17) Hummelen, J. C.; Knight, B. W.; LePeq, F.; Wudl, F.; Yao, J.; Wilkins, C. L. *J. Org. Chem.* **1995**, *60*, 532–538.

(18) Eftaiha, A. F.; Sun, J.-P.; Hill, I. G.; Welch, G. C. *J. Mater. Chem. A* **2014**, *2*, 1201–1213.

(19) Scharber, M. C.; Sariciftci, N. S. *Prog. Polym. Sci.* **2013**, *38*, 1929–1940.

(20) Dang, M. T.; Hirsch, L.; Wantz, G. *Adv. Mater.* **2011**, *23*, 3597–3602.

(21) Kim, J. Y.; Kim, S. H.; Lee, H.-H.; Lee, K.; Ma, W.; Gong, X.; Heeger, A. J. *Adv. Mater.* **2006**, *18*, 572–576.

(22) Reyes-Reyes, M.; Kim, K.; Carroll, D. L. *Appl. Phys. Lett.* **2005**, *87*, 83506.

(23) Garcia-Belmonte, G.; Boix, P. P.; Bisquert, J.; Sessolo, M.; Bolink, H. J. *Sol. Energy Mater. Sol. Cells* **2010**, *94*, 366–375.

(24) Pivrikas, A.; Sariciftci, N. S.; Juška, G.; Österbacka, R. *Prog. Photovoltaics Res. Appl.* **2007**, *15*, 677–696.

(25) Schafferhans, J.; Baumann, A.; Wagenpfahl, A.; Deibel, C.; Dyakonov, V. *Org. Electron.* **2010**, *11*, 1693–1700.

(26) Kularatne, R. S.; Magurudeniya, H. D.; Sista, P.; Biewer, M. C.; Stefan, M. C. *J. Polym. Sci. Part A Polym. Chem.* **2013**, *51*, 743–768.

(27) He, Z.; Zhong, C.; Su, S.; Xu, M.; Wu, H.; Cao, Y. *Nat. Photonics* **2012**, *6*, 593–597.

(28) You, J.; Chen, C.-C.; Hong, Z.; Yoshimura, K.; Ohya, K.; Xu, R.; Ye, S.; Gao, J.; Li, G.; Yang, Y. *Adv. Mater.* **2013**, *25*, 3973–3978.

(29) Dennler, G.; Scharber, M. C.; Ameri, T.; Denk, P.; Forberich, K.; Waldauf, C.; Brabec, C. J. *Adv. Mater.* **2008**, *20*, 579–583.

(30) Kalowekamo, J.; Baker, E. *Sol. Energy* **2009**, *83*, 1224–1231.

(31) Zhan, X.; Zhu, D. *Polym. Chem.* **2010**, *1*, 409.

(32) Potscavage, W. J.; Yoo, S.; Kippelen, B. *Appl. Phys. Lett.* **2008**, *93*, 193308.

(33) Brabec, C. J.; Cravino, A.; Meissner, D.; Sariciftci, N. S.; Fromherz, T.; Rispens, M. T.; Sanchez, L.; Hummelen, J. C. *Adv. Funct. Mater.* **2001**, *11*, 374–380.

(34) Scharber, M. C.; Mühlbacher, D.; Koppe, M.; Denk, P.; Waldauf, C.; Heeger, A. J.; Brabec, C. J. *Adv. Mater.* **2006**, *18*, 789–794.

(35) Topham, P. D.; Parnell, A. J.; Hiorns, R. C. *J. Polym. Sci. Part B Polym. Phys.* **2011**, *49*, 1131–1156.

(36) Yin, Z.; Wei, J.; Zheng, Q. *Adv. Sci.* **2016**, *3*, 1500362.

(37) Yip, H.-L.; Jen, A. K.-Y. *Energy Environ. Sci.* **2012**, *5*, 5994.

(38) Yin, Z.; Zheng, Q.; Chen, S.-C.; Cai, D. *ACS Appl. Mater. Interfaces* **2013**, *5*, 9015–9025.

(39) Tremolet de Villers, B. J.; MacKenzie, R. C. I.; Jasieniak, J. J.; Treat, N. D.; Chabinyc, M. L. *Adv. Energy Mater.* **2014**, *4*, 1301290.

(40) Subbiah, J.; Amb, C. M.; Irfan, I.; Gao, Y.; Reynolds, J. R.; So, F. *ACS Appl. Mater. Interfaces* **2012**, *4*, 866–870.

(41) Lu, K.; Yuan, J.; Peng, J.; Huang, X.; Cui, L.; Jiang, Z.; Wang, H.-Q.; Ma, W. *J. Mater. Chem. A* **2013**, *1*, 14253.

(42) White, M. S.; Olson, D. C.; Shaheen, S. E.; Kopidakis, N.; Ginley, D. S. *Appl. Phys. Lett.* **2006**, *89*, 143517.

(43) Waldauf, C.; Morana, M.; Denk, P.; Schilinsky, P.; Coakley, K.; Choulis, S. A.; Brabec, C. J. *Appl. Phys. Lett.* **2006**, *89*, 233517.

(44) Trost, S.; Zilberberg, K.; Behrendt, A.; Riedl, T. *J. Mater. Chem.* **2012**, *22*, 16224.

(45) Siddiki, M. K.; Venkatesan, S.; Qiao, Q. *Phys. Chem. Chem. Phys.* **2012**, *14*, 4682.

(46) He, Z.; Zhong, C.; Huang, X.; Wong, W.-Y.; Wu, H.; Chen, L.; Su, S.; Cao, Y. *Adv. Mater.* **2011**, *23*, 4636–4643.

(47) Tang, Z.; Tress, W.; Bao, Q.; Jafari, M. J.; Bergqvist, J.; Ederth, T.; Andersson, M. R.; Inganäs, O. *Adv. Energy Mater.* **2014**, *4*, 1400643.

(48) Hu, X.; Yi, C.; Wang, M.; Hsu, C.-H.; Liu, S.; Zhang, K.; Zhong, C.; Huang, F.;

Gong, X.; Cao, Y. *Adv. Energy Mater.* **2014**, *4*, 1400378.

(49) Zhao, D. W.; Liu, P.; Sun, X. W.; Tan, S. T.; Ke, L.; Kyaw, A. K. K. *Appl. Phys. Lett.* **2009**, *95*, 153304.

(50) Jiang, C. Y.; Sun, X. W.; Zhao, D. W.; Kyaw, A. K. K.; Li, Y. N. *Sol. Energy Mater. Sol. Cells* **2010**, *94*, 1618–1621.

(51) Huang, J.; Li, G.; Yang, Y. *Adv. Mater.* **2008**, *20*, 415–419.

(52) Chen, F.; Chen, Q.; Mao, L.; Wang, Y.; Huang, X.; Lu, W.; Wang, B.; Chen, L. *Nanotechnology* **2013**, *24*, 484011.

(53) Jin, S. H.; Jun, G. H.; Hong, S. H.; Jeon, S. *Carbon N. Y.* **2012**, *50*, 4483–4488.

(54) Liu, J.; Durstock, M.; Dai, L. *Energy Environ. Sci.* **2014**, *7*, 1297–1306.

(55) Reese, M. O.; White, M. S.; Rumbles, G.; Ginley, D. S.; Shaheen, S. E. *Appl. Phys. Lett.* **2008**, *92*, 53307.

(56) Kim, D. Y.; Subbiah, J.; Sarasqueta, G.; So, F.; Ding, H.; Irfan; Gao, Y. *Appl. Phys. Lett.* **2009**, *95*, 93304.

(57) van Reenen, S.; Kouijzer, S.; Janssen, R. A. J.; Wienk, M. M.; Kemerink, M. *Adv. Mater. Interfaces* **2014**, *1*, 1400189.

(58) Yuan, Y.; Reece, T. J.; Sharma, P.; Poddar, S.; Ducharme, S.; Gruverman, A.; Yang, Y.; Huang, J. *Nat. Mater.* **2011**, *10*, 296–302.

(59) Bilby, D.; Frieberg, B.; Kramadhati, S.; Green, P.; Kim, J. *ACS Appl. Mater. Interfaces* **2014**, *6*, 14964–14974.

(60) Yip, H.-L.; Jen, A. K.-Y. *Energy Environ. Sci.* **2012**, *5*, 5994–6011.

(61) Jørgensen, M.; Norrman, K.; Gevorgyan, S. A.; Tromholt, T.; Andreasen, B.; Krebs, F. C. *Adv. Mater.* **2012**, *24*, 580–612.

(62) He, W.; Jiang, Y.; Qin, Y. *Polym. Chem.* **2014**, *5*, 1298–1304.

(63) He, W.; Livshits, M. Y.; Dickie, D. A.; Yang, J.; Quinnett, R.; Rack, J. J.; Wu, Q.; Qin, Y. *Chem. Sci.* **2016**, *7*, 5798–5804.

(64) Kim, Y.; Choulis, S. A.; Nelson, J.; Bradley, D. D. C.; Cook, S.; Durrant, J. R. *Appl. Phys. Lett.* **2005**, *86*, 63502.

(65) Ma, W.; Yang, C.; Gong, X.; Lee, K.; Heeger, A. J. *Adv. Funct. Mater.* **2005**, *15*, 1617–1622.

(66) Padinger, F.; Rittberger, R. S.; Sariciftci, N. S. *Adv. Funct. Mater.* **2003**, *13*, 85–88.

(67) Li, G.; Yao, Y.; Yang, H.; Shrotriya, V.; Yang, G.; Yang, Y. *Adv. Funct. Mater.* **2007**, *17*, 1636–1644.

(68) Li, G.; Shrotriya, V.; Huang, J.; Yao, Y.; Moriarty, T.; Emery, K.; Yang, Y. *Nat. Mater.* **2005**, *4*, 864–868.

(69) Mihailetchi, V. D.; Xie, H.; de Boer, B.; Popescu, L. M.; Hummelen, J. C.; Blom, P. W. M.; Koster, L. J. A. *Appl. Phys. Lett.* **2006**, *89*, 12107.

(70) Shrotriya, V.; Yao, Y.; Li, G.; Yang, Y. *Appl. Phys. Lett.* **2006**, *89*, 63505.

(71) Tang, H.; Lu, G.; Li, L.; Li, J.; Wang, Y.; Yang, X. *J. Mater. Chem.* **2010**, *20*,

683–688.

(72) Liao, H.-C.; Ho, C.-C.; Chang, C.-Y.; Jao, M.-H.; Darling, S. B.; Su, W.-F. *Mater. Today* **2013**, *16*, 326–336.

(73) Wong, W.-Y.; Wang, X.-Z.; He, Z.; Djurišić, A. B.; Yip, C.-T.; Cheung, K.-Y.; Wang, H.; Mak, C. S. K.; Chan, W.-K. *Nat. Mater.* **2007**, *6*, 521–527.

(74) Dang, M. T.; Hirsch, L.; Wantz, G.; Wuest, J. D. *Chem. Rev.* **2013**, *113*, 3734–3765.

(75) Liu, F.; Gu, Y.; Jung, J. W.; Jo, W. H.; Russell, T. P. *J. Polym. Sci. Part B Polym. Phys.* **2012**, *50*, 1018–1044.

(76) Rogers, J. T.; Schmidt, K.; Toney, M. F.; Kramer, E. J.; Bazan, G. C. *Adv. Mater.* **2011**, *23*, 2284–2288.

(77) Rogers, J. T.; Schmidt, K.; Toney, M. F.; Bazan, G. C.; Kramer, E. J. *J. Am. Chem. Soc.* **2012**, *134*, 2884–2887.

(78) Mak, C. S. K.; Chan, W. K. In *Macromolecules Containing Metal and Metal-Like Elements*; John Wiley & Sons, Inc.: Hoboken, NJ, USA, 2010; pp 159–189.

(79) Ho, C.-L.; Yu, Z.-Q.; Wong, W.-Y. *Chem. Soc. Rev.* **2016**, *45*, 5264–5295.

(80) Hsu, H.-Y.; Vella, J. H.; Myers, J. D.; Xue, J.; Schanze, K. S. *J. Phys. Chem. C* **2014**, *118*, 24282–24289.

(81) Wong, W.-Y.; Wang, X.-Z.; He, Z.; Chan, K.-K.; Djurišić, A. B.; Cheung, K.-Y.; Yip, C.-T.; Ng, A. M.-C.; Xi, Y. Y.; Mak, C. S. K.; Chan, W.-K. *J. Am. Chem. Soc.* **2007**, *129*, 14372–14380.

(82) Liu, L.; Ho, C.-L.; Wong, W.-Y.; Cheung, K.-Y.; Fung, M.-K.; Lam, W.-T.; Djurišić, A. B.; Chan, W.-K. *Adv. Funct. Mater.* **2008**, *18*, 2824–2833.

(83) Wong, W.-Y.; Chow, W.-C.; Cheung, K.-Y.; Fung, M.-K.; Djurišić, A. B.; Chan, W.-K. *J. Organomet. Chem.* **2009**, *694*, 2717–2726.

(84) Wang, X.-Z.; Wang, Q.; Yan, L.; Wong, W.-Y.; Cheung, K.-Y.; Ng, A.; Djurišić, A. B.; Chan, W.-K. *Macromol. Rapid Commun.* **2010**, *31*, 861–867.

(85) Khan, M. S.; Al-Mandhary, M. R. A.; Al-Suti, M. K.; Al-Battashi, F. R.; Al-Saadi, S.; Ahrens, B.; Bjernemose, J. K.; Mahon, M. F.; Raithby, P. R.; Younus, M.; Chawdhury, N.; Köhler, A.; Marseglia, E. A.; Tedesco, E.; Feeder, N.; Teat, S. J. *Dalt. Trans.* **2004**, 2377–2385.

(86) Boudreault, P.-L. T.; Najari, A.; Leclerc, M. *Chem. Mater.* **2011**, *23*, 456–469.

(87) Bian, L.; Zhu, E.; Tang, J.; Tang, W.; Zhang, F. *Prog. Polym. Sci.* **2012**, *37*, 1292–1331.

(88) Beaujuge, P. M.; Fréchet, J. M. J. *J. Am. Chem. Soc.* **2011**, *133*, 20009–20029.

(89) Zhou, H.; Yang, L.; You, W. *Macromolecules* **2012**, *45*, 607–632.

(90) Hirao, T. *Coord. Chem. Rev.* **2002**, *226*, 81–91.

(91) Liu, Y.; Li, Y.; Schanze, K. S. *J. Photochem. Photobiol. C Photochem. Rev.* **2002**, *3*, 1–23.

(92) Moorlag, C.; Sih, B. C.; Stott, T. L.; Wolf, M. O. *J. Mater. Chem.* **2005**, *15*, 2433.

(93) Wolf, M. O. *J. Inorg. Organomet. Polym. Mater.* **2006**, *16*, 189–199.

(94) Ho, C.-L.; Wong, W.-Y. *Coord. Chem. Rev.* **2013**, *257*, 1614–1649.

(95) Wong, W.-Y. *J. Inorg. Organomet. Polym. Mater.* **2005**, *15*, 197–219.

(96) Wong, W.-Y. *Dalt. Trans.* **2007**, 4495.

(97) Ng, A.; Ho, C.-L.; Fung, M. K.; Sun, Y. C.; Shao, S.-Y.; Fu, Y.-Y.; Ng, A. M. C.; Li, C. H.; Cheung, W. K.; Leung, Y. H.; Djurišić, A. B.; Wang, Q.; He, Z.; Wang, X.; Chan, W.-K.; Xie, Z.-Y.; Zapien, J. A.; To, C. H.; Wong, W.-Y. *Macromol. Chem. Phys.* **2012**, *213*, 1300–1310.

(98) Yan, L.; Zhao, Y.; Wang, X.; Wang, X.-Z.; Wong, W.-Y.; Liu, Y.; Wu, W.; Xiao, Q.; Wang, G.; Zhou, X.; Zeng, W.; Li, C.; Wang, X.; Wu, H. *Macromol. Rapid Commun.* **2012**, *33*, 603–609.

(99) Köhler, A.; Wittmann, H. F.; Friend, R. H.; Khan, M. S.; Lewis, J. *Synth. Met.* **1996**, *77*, 147–150.

(100) Beljonne, D.; Wittmann, H. F.; Köhler, A.; Graham, S.; Younus, M.; Lewis, J.; Raithby, P. R.; Khan, M. S.; Friend, R. H.; Brédas, J. L. *J. Chem. Phys.* **1996**, *105*, 3868–3877.

(101) Chawdhury, N.; Köhler, A.; Friend, R. H.; Wong, W.-Y.; Lewis, J.; Younus, M.; Raithby, P. R.; Corcoran, T. C.; Al-Mandhary, M. R. A.; Khan, M. S. *J. Chem. Phys.* **1999**, *110*, 4963–4970.

(102) Wilson, J. S.; Köhler, A.; Friend, R. H.; Al-Suti, M. K.; Al-Mandhary, M. R. A.; Khan, M. S.; Raithby, P. R. *J. Chem. Phys.* **2000**, *113*, 7627–7634.

(103) Liu, Y.; Jiang, S.; Glusac, K.; Powell, D. H.; Anderson, D. F.; Schanze, K. S. *J.*

Am. Chem. Soc. **2002**, *124*, 12412–12413.

(104) Ramakrishna, G.; Goodson, T.; Rogers-Haley, J. E.; Cooper, T. M.; McLean, D. G.; Urbas, A. *J. Phys. Chem. C* **2009**, *113*, 1060–1066.

(105) Wong, W.-Y. *Macromol. Chem. Phys.* **2008**, *209*, 14–24.

(106) Wong, W.-Y.; Ho, C.-L. *Acc. Chem. Res.* **2010**, *43*, 1246–1256.

(107) Wong, W.-Y.; Harvey, P. D. *Macromol. Rapid Commun.* **2010**, *31*, 671–713.

(108) Wong, W.-Y.; Chan, S.-M.; Choi, K.-H.; Cheah, K.-W.; Chan, W.-K. *Macromol. Rapid Commun.* **2000**, *21*, 453–457.

(109) Guo, F.; Kim, Y.-G.; Reynolds, J. R.; Schanze, K. S. *Chem. Commun.* **2006**, *17*, 1887–1889.

(110) Wong, W.-Y.; Wang, X.; Zhang, H.-L.; Cheung, K.-Y.; Fung, M.-K.; Djurišić, A. B.; Chan, W.-K. *J. Organomet. Chem.* **2008**, *693*, 3603–3612.

(111) Mei, J.; Ogawa, K.; Kim, Y.-G.; Heston, N. C.; Arenas, D. J.; Nasrollahi, Z.; McCarley, T. D.; Tanner, D. B.; Reynolds, J. R.; Schanze, K. S. *ACS Appl. Mater. Interfaces* **2009**, *1*, 150–161.

(112) Wu, P.-T.; Bull, T.; Kim, F. S.; Luscombe, C. K.; Jenekhe, S. A. *Macromolecules* **2009**, *42*, 671–681.

(113) Zhan, H.; Lamare, S.; Ng, A.; Kenny, T.; Guernon, H.; Chan, W.-K.; Djurišić, A. B.; Harvey, P. D.; Wong, W.-Y. *Macromolecules* **2011**, *44*, 5155–5167.

(114) Baek, N. S.; Hau, S. K.; Yip, H.-L.; Acton, O.; Chen, K.-S.; Jen, A. K.-Y. *Chem.*

Mater. **2008**, *20*, 5734–5736.

(115) Wang, X.-Z.; Wong, W.-Y.; Cheung, K.-Y.; Fung, M.-K.; Djurišić, A. B.; Chan, W.-K. *Dalt. Trans.* **2008**, 5484.

(116) Wang, Q.; Wong, W.-Y. *Polym. Chem.* **2011**, *2*, 432–440.

(117) Qin, C.; Fu, Y.; Chui, C.-H.; Kan, C.-W.; Xie, Z.; Wang, L.; Wong, W.-Y. *Macromol. Rapid Commun.* **2011**, *32*, 1472–1477.

(118) Dasarathy, A.; Isaacson, J. P.; Jones-Smith, K.; Tabachnik, J.; Mathur, H. *Phys. Rev. A* **2013**, *87*, 62111.

(119) Ziessel, R.; Ulrich, G.; Harriman, A. *New J. Chem.* **2007**, *31*, 496.

(120) Loudet, A.; Burgess, K. *Chem. Rev.* **2007**, *107*, 4891–4932.

(121) Ulrich, G.; Ziessel, R.; Harriman, A. *Angew. Chemie Int. Ed.* **2008**, *47*, 1184–1201.

(122) Boens, N.; Leen, V.; Dehaen, W. *Chem. Soc. Rev.* **2012**, *41*, 1130–1172.

(123) Bessette, A.; Hanan, G. S. *Chem. Soc. Rev.* **2014**, *43*, 3342.

(124) Yuan, L.; Lin, W.; Zheng, K.; He, L.; Huang, W. *Chem. Soc. Rev.* **2013**, *42*, 622–661.

(125) Rousseau, T.; Cravino, A.; Ripaud, E.; Leriche, P.; Rihn, S.; De Nicola, A.; Ziessel, R.; Roncali, J. *Chem. Commun.* **2010**, *46*, 5082.

(126) Kubo, Y.; Watanabe, K.; Nishiyabu, R.; Hata, R.; Murakami, A.; Shoda, T.; Ota, H. *Org. Lett.* **2011**, *13*, 4574–4577.

(127) Bura, T.; Leclerc, N.; Fall, S.; Lévêque, P.; Heiser, T.; Ziessel, R. *Org. Lett.* **2011**, *13*, 6030–6033.

(128) Bura, T.; Leclerc, N.; Fall, S.; Lévêque, P.; Heiser, T.; Retailleau, P.; Rihn, S.; Mirloup, A.; Ziessel, R. *J. Am. Chem. Soc.* **2012**, *134*, 17404–17407.

(129) Chen, J. J.; Conron, S. M.; Erwin, P.; Dimitriou, M.; McAlahney, K.; Thompson, M. E. *ACS Appl. Mater. Interfaces* **2015**, *7*, 662–669.

(130) Kauffman, G. B.; Teter, L. A.; Huheey, J. E. In *Inorgnic Syntheses*; 1963; pp 245–249.

(131) Glimsdal, E.; Carlsson, M.; Kindahl, T.; Lindgren, M.; Lopes, C.; Eliasson, B. *J. Phys. Chem. A* **2010**, *114*, 3431–3442.

(132) Davis, M. C.; Baldwin, L. C.; Groshens, T. J. *Tetrahedron Lett.* **2012**, *53*, 1564–1566.

(133) Noth, H.; Wrackmeyer, B. *Nuclear Magnetic Resonance Spectroscopy of Boron Compounds*; 1978.

(134) Younus, M.; Köhler, A.; Cron, S.; Chawdhury, N.; Al-Mandhary, M. R. A.; Khan, M. S.; Lewis, J.; Long, N. J.; Friend, R. H.; Raithby, P. R. *Angew. Chemie Int. Ed.* **1998**, *37*, 3036–3039.

(135) Wu, W.; Zhao, J.; Sun, J.; Huang, L.; Yi, X. *J. Mater. Chem. C* **2013**, *1*, 705–716.

(136) Caspar, J. V.; Sullivan, B. P.; Kober, E. M.; Meyer, T. J. *Chem. Phys. Lett.* **1982**, *91*, 91–95.

(137) Xu, Z.; Chen, L.-M.; Chen, M.-H.; Li, G.; Yang, Y. *Appl. Phys. Lett.* **2009**, *95*,

13301.

(138) Chu, C.-W.; Li, S.-H.; Chen, C.-W.; Shrotriya, V.; Yang, Y. *Appl. Phys. Lett.* **2005**, *87*, 193508.

(139) Shrotriya, V.; Li, G.; Yao, Y.; Chu, C.-W.; Yang, Y. *Appl. Phys. Lett.* **2006**, *88*, 73508.

(140) Steinmann, V.; Kronenberg, N. M.; Lenze, M. R.; Graf, S. M.; Hertel, D.; Meerholz, K.; Bürckstümmer, H.; Tulyakova, E. V.; Würthner, F. *Adv. Energy Mater.* **2011**, *1*, 888–893.

(141) Sun, Y.; Seo, J. H.; Takacs, C. J.; Seifter, J.; Heeger, A. J. *Adv. Mater.* **2011**, *23*, 1679–1683.

(142) Krebs, F. C.; Espinosa, N.; Hösel, M.; Søndergaard, R. R.; Jørgensen, M. *Adv. Mater.* **2014**, *26*, 29–39.

(143) You, J.; Dou, L.; Yoshimura, K.; Kato, T.; Ohya, K.; Moriarty, T.; Emery, K.; Chen, C.-C.; Gao, J.; Li, G.; Yang, Y. *Nat. Commun.* **2013**, *4*, 1446.

(144) Kan, B.; Li, M.; Zhang, Q.; Liu, F.; Wan, X.; Wang, Y.; Ni, W.; Long, G.; Yang, X.; Feng, H.; Zuo, Y.; Zhang, M.; Huang, F.; Cao, Y.; Russell, T. P.; Chen, Y. *J. Am. Chem. Soc.* **2015**, *137*, 3886–3893.

(145) Zhang, J.; Zhang, Y.; Fang, J.; Lu, K.; Wang, Z.; Ma, W.; Wei, Z. *J. Am. Chem. Soc.* **2015**, *137*, 8176–8183.

(146) Ouyang, X.; Peng, R.; Ai, L.; Zhang, X.; Ge, Z. *Nat. Photonics* **2015**, *9*, 520–524.

(147) Subbiah, J.; Purushothaman, B.; Chen, M.; Qin, T.; Gao, M.; Vak, D.; Scholes, F.

H.; Chen, X.; Watkins, S. E.; Wilson, G. J.; Holmes, A. B.; Wong, W. W. H.; Jones, D. J. *Adv. Mater.* **2015**, *27*, 702–705.

(148) Liu, Y.; Page, Z. A.; Russell, T. P.; Emrick, T. *Angew. Chemie Int. Ed.* **2015**, *54*, 11485–11489.

(149) Huang, Y.; Kramer, E. J.; Heeger, A. J.; Bazan, G. C. *Chem. Rev.* **2014**, *114*, 7006–7043.

(150) Chen, L.-M.; Xu, Z.; Hong, Z.; Yang, Y. *J. Mater. Chem.* **2010**, *20*, 2575.

(151) Page, Z. A.; Liu, Y.; Duzhko, V. V.; Russell, T. P.; Emrick, T. *Science (80-.).* **2014**, *346*, 441–444.

(152) Ameri, T.; Dennler, G.; Lungenschmied, C.; Brabec, C. J. *Energy Environ. Sci.* **2009**, *2*, 347.

(153) Zhou, H.; Zhang, Y.; Mai, C.-K.; Collins, S. D.; Bazan, G. C.; Nguyen, T.-Q.; Heeger, A. J. *Adv. Mater.* **2015**, *27*, 1767–1773.

(154) Brabec, C. J.; Heeney, M.; McCulloch, I.; Nelson, J. *Chem. Soc. Rev.* **2011**, *40*, 1185–1199.

(155) Heeger, A. J. *Adv. Mater.* **2014**, *26*, 10–28.

(156) Köhler, A.; Bässler, H. *J. Mater. Chem.* **2011**, *21*, 4003–4011.

(157) Fishchuk, I. I.; Kadashchuk, A.; Sudha Devi, L.; Heremans, P.; Bässler, H.; Köhler, A. *Phys. Rev. B* **2008**, *78*, 45211.

(158) Sudha Devi, L.; Al-Suti, M. K.; Dosche, C.; Khan, M. S.; Friend, R. H.; Köhler, A.

Phys. Rev. B **2008**, *78*, 45210.

(159) Hoffmann, S. T.; Scheler, E.; Koenen, J.-M.; Forster, M.; Scherf, U.; Strohriegl, P.; Bässler, H.; Köhler, A. *Phys. Rev. B* **2010**, *81*, 165208.

(160) Shao, Y.; Yang, Y. *Adv. Mater.* **2005**, *17*, 2841–2844.

(161) Schanze, K. S.; Silverman, E. E.; Zhao, X. *J. Phys. Chem. B* **2005**, *109*, 18451–18459.

(162) Schulz, G. L.; Holdcroft, S. *Chem. Mater.* **2008**, *20*, 5351–5355.

(163) Qian, M.; Zhang, R.; Hao, J.; Zhang, W.; Zhang, Q.; Wang, J.; Tao, Y.; Chen, S.; Fang, J.; Huang, W. *Adv. Mater.* **2015**, *27*, 3546–3552.

(164) Glusac, K.; Köse, M. E.; Jiang, H.; Schanze, K. S. *J. Phys. Chem. B* **2007**, *111*, 929–940.

(165) Walker, B.; Kim, C.; Nguyen, T.-Q. *Chem. Mater.* **2011**, *23*, 470–482.

(166) Coughlin, J. E.; Henson, Z. B.; Welch, G. C.; Bazan, G. C. *Acc. Chem. Res.* **2014**, *47*, 257–270.

(167) Kan, B.; Zhang, Q.; Li, M.; Wan, X.; Ni, W.; Long, G.; Wang, Y.; Yang, X.; Feng, H.; Chen, Y. *J. Am. Chem. Soc.* **2014**, *136*, 15529–15532.

(168) Guo, F.; Ogawa, K.; Kim, Y.-G.; Danilov, E. O.; Castellano, F. N.; Reynolds, J. R.; Schanze, K. S. *Phys. Chem. Chem. Phys.* **2007**, *9*, 2724.

(169) Anthony, J. E.; Brooks, J. S.; Eaton, D. L.; Parkin, S. R. *J. Am. Chem. Soc.* **2001**, *123*, 9482–9483.

(170) Anthony, J. E. *Chem. Rev.* **2006**, *106*, 5028–5048.

(171) Pope, M.; Swenberg, C. E. In *Electronic Processes in Organic Crystals and Polymers*; 1999.

(172) Dubinina, G. G.; Price, R. S.; Abboud, K. A.; Wnuk, P.; Stepanenko, Y.; Drobizhev, M.; Rebane, A.; Schanze, K. S. *J. Am. Chem. Soc.* **2012**, *134*, 1–4.

(173) Casida, M. E. In *in Recenet Advances in Densit Functional Methods*; Chong, D. P., Ed.; World Scientific Publishing Co. Ltd.: Singapore, 1995; p 155.

(174) Bauernschmitt, R.; Ahlrichs, R. *Chem. Phys. Lett.* **1996**, *256*, 454–464.

(175) Hay, P. J.; Wadt, W. R. *J. Chem. Phys.* **1985**, *82*, 299–310.

(176) Tomasi, J.; Mennucci, B.; Cammi, R. *Chem. Rev.* **2005**, *105*, 2999–3094.

(177) Dreuw, A.; Head-Gordon, M. *J. Am. Chem. Soc.* **2004**, *126*, 4007–4016.

(178) Price, S. C.; Stuart, A. C.; Yang, L.; Zhou, H.; You, W. *J. Am. Chem. Soc.* **2011**, *133*, 4625–4631.

(179) Huo, L.; Zhang, S.; Guo, X.; Xu, F.; Li, Y.; Hou, J. *Angew. Chemie Int. Ed.* **2011**, *50*, 9697–9702.

(180) Son, H. J.; Lu, L.; Chen, W.; Xu, T.; Zheng, T.; Carsten, B.; Strzalka, J.; Darling, S. B.; Chen, L. X.; Yu, L. *Adv. Mater.* **2013**, *25*, 838–843.

(181) Dou, L.; Chang, W.-H.; Gao, J.; Chen, C.-C.; You, J.; Yang, Y. *Adv. Mater.* **2013**, *25*, 825–831.

(182) Spano, F. C. *Acc. Chem. Res.* **2010**, *43*, 429–439.

(183) Spano, F. C.; Silva, C. *Annu. Rev. Phys. Chem.* **2014**, *65*, 477–500.

(184) Chen, Z.; Hsu, H.-Y.; Arca, M.; Schanze, K. S. *J. Phys. Chem. B* **2015**, *119*, 7198–7209.

(185) Murgatroyd, P. N. *J. Phys. D. Appl. Phys.* **1970**, *3*, 308.

(186) Schröder, N.; Lied, F.; Glorius, F. *J. Am. Chem. Soc.* **2015**, *137*, 1448–1451.

(187) Pawle, R. H.; Agarwal, A.; Malveira, S.; Smith, Z. C.; Thomas, S. W. *Macromolecules* **2014**, *47*, 2250–2256.

(188) Kim, H. G.; Jo, S. B.; Shim, C.; Lee, J.; Shin, J.; Cho, E. C.; Ihn, S.-G.; Choi, Y. S.; Kim, Y.; Cho, K. *J. Mater. Chem.* **2012**, *22*, 17709.

(189) Lin, Y.-Z.; Yeh, C.-W.; Chou, P.-T.; Watanabe, M.; Chang, Y.-H.; Chang, Y. J.; Chow, T. J. *Dye. Pigment.* **2014**, *109*, 81–89.

(190) Bilkay, T.; Schulze, K.; Egorov-Brening, T.; Fink, K.; Janietz, S. *Org. Electron.* **2013**, *14*, 344–353.

(191) Yiliang, W.; Ping, L.; James, W. A.; Nan-Xing, H. Semiconducting composition from spiro compounds. US 20110260114 A1 20111027, 2011.

(192) Stuart, A. C.; Tumbleston, J. R.; Zhou, H.; Li, W.; Liu, S.; Ade, H.; You, W. *J. Am. Chem. Soc.* **2013**, *135*, 1806–1815.

(193) Kim, J.; Yun, M. H.; Kim, G.-H.; Lee, J.; Lee, S. M.; Ko, S.-J.; Kim, Y.; Dutta, G. K.; Moon, M.; Park, S. Y.; Kim, D. S.; Kim, J. Y.; Yang, C. *ACS Appl. Mater. Interfaces* **2014**, *6*, 7523–7534.

(194) Melhuish, W. H. *J. Phys. Chem.* **1961**, *65*, 229–235.

(195) Cook, S.; Furube, A.; Katoh, R. *Energy Environ. Sci.* **2008**, *1*, 294.

(196) Fu, B.; Baltazar, J.; Hu, Z.; Chien, A.-T.; Kumar, S.; Henderson, C. L.; Collard, D. M.; Reichmanis, E. *Chem. Mater.* **2012**, *24*, 4123–4133.

(197) Wang, L.; Huang, W.; Li, R.; Gehrig, D.; Blom, P. W. M.; Landfester, K.; Zhang, K. A. I. *Angew. Chemie Int. Ed.* **2016**, *55*, 9783–9787.

(198) Bhanvadia, V. J.; Patel, H. A.; Sharma, N. N.; Patel, A. L. *Synth. Commun.* **2016**, *46*, 1052–1061.

(199) Chen, M.; Moad, G.; Rizzardo, E.; Evans, R. A.; Haeussler, M. Conducting and semiconducting organic materials. WO2009155657 A1, 2009.

(200) Liu, T.; Troisi, A. *Adv. Mater.* **2013**, *25*, 1038–1041.

(201) Clarke, T. M.; Durrant, J. R. *Chem. Rev.* **2010**, *110*, 6736–6767.

(202) Gregg, B. A. *J. Phys. Chem. Lett.* **2011**, *2*, 3013–3015.

(203) Zhang, C.; Zhao, J.; Cui, X.; Wu, X. *J. Org. Chem.* **2015**, *80*, 5674–5686.

(204) Mahmood, Z.; Zhao, J. *J. Org. Chem.* **2016**, *81*, 587–594.

(205) Zhou, Q.; Zhou, M.; Wei, Y.; Zhou, X.; Liu, S.; Zhang, S.; Zhang, B. *Phys. Chem. Chem. Phys.* **2017**, *19*, 1516–1525.

(206) Xu, S.; Liu, T.; Mu, Y.; Wang, Y.-F.; Chi, Z.; Lo, C.-C.; Liu, S.; Zhang, Y.; Lien, A.; Xu, J. *Angew. Chemie Int. Ed.* **2015**, *54*, 874–878.

(207) Tanaka, H.; Shizu, K.; Miyazaki, H.; Adachi, C. *Chem. Commun.* **2012**, *48*, 11392.

(208) Nakagawa, T.; Ku, S.-Y.; Wong, K.-T.; Adachi, C. *Chem. Commun.* **2012**, *48*, 9580.

(209) Méhes, G.; Nomura, H.; Zhang, Q.; Nakagawa, T.; Adachi, C. *Angew. Chemie Int. Ed.* **2012**, *51*, 11311–11315.

(210) Uoyama, H.; Goushi, K.; Shizu, K.; Nomura, H.; Adachi, C. *Nature* **2012**, *492*, 234–238.

(211) Wang, H.; Xie, L.; Peng, Q.; Meng, L.; Wang, Y.; Yi, Y.; Wang, P. *Adv. Mater.* **2014**, *26*, 5198–5204.

(212) Lee, J.; Shizu, K.; Tanaka, H.; Nomura, H.; Yasuda, T.; Adachi, C. *J. Mater. Chem. C* **2013**, *1*, 4599.